

**Building a 300 mK-17 T-UHV-  
scanning tunnelling microscopy system**

**and**

**spin-resolved investigation of individual  
bis(phthalocyaninato)terbium single-molecule magnets**

Dissertation  
zur Erlangung des Doktorgrades  
des Fachbereichs Physik  
der Universität Hamburg

vorgelegt von  
**Jörg Schwöbel**  
aus Wuppertal

Hamburg  
2018

Gutachter der Dissertation: Prof. Dr. Roland Wiesendanger  
Prof. Dr. Nils Huse  
Gutachter der Disputation: Prof. Dr. Roland Wiesendanger  
Prof. Dr. Peter Burger  
Datum der Disputation: 12. Februar 2018  
Vorsitzender des Prüfungsausschusses: Prof. Dr. Michael A. Rübhausen  
Vorsitzender des Promotionsausschusses: Prof. Dr. Wolfgang Hansen  
Leiter des Departments Physik: Prof. Dr. Michael Potthoff  
Dekan der MIN-Fakultät: Prof. Dr. Heinrich Graener

# Kurzfassung

Diese Arbeit präsentiert eine Untersuchung des Einzelmolekülmagneten Bis(phthalocyaninato)terbium mit spinaufgelöster Rastertunnelmikroskopie und -spektroskopie, eine Untersuchung des Schaltens von chiralen zu achiralen Konformationen ebendieses Moleküls, sowie den Aufbau einer Rastertunnelmikroskopanlage für die Untersuchung von Molekülen bei tiefen Temperaturen und in hohen Magnetfeldern.

Einzelmolekülmagnete sind einzelne Moleküle, die eine (wenn auch kurzzeitig und bei tiefen Temperaturen) stabile Magnetisierung aufweisen. Ein vielversprechender Vertreter ist Bis(phthalocyaninato)terbium ( $\text{TbPc}_2$ ), ein Doppeldeckermolekül, in dem zwei parallele Phthalocyaninliganden ein zentrales Terbiumion umschließen. Neben dem zentralen Terbiumion ( $J = 6$ ) stellt der Spin eines über beide Liganden delokalisierten ungepaarten Elektrons ein zweites Spinsystem dar. Beide, ihre Wechselwirkung, der Zugriff auf diese Systeme und ihre Interaktion mit der Umgebung sind Gegenstand intensiver Forschung.  $\text{TbPc}_2$  kann einerseits als kleiner und stabiler Vertreter der Klasse von Einzelmolekülmagneten gesehen werden, andererseits als ein Modellsystem für paramagnetische Einzelatome, die mithilfe eines molekularen Ligandenfelds zu Superparamagneten werden.

In der vorliegenden Arbeit wurden einzelne  $\text{TbPc}_2$ -Moleküle auf einem unmagnetischen und, zur magnetischen Kopplung, einem ferromagnetischen Substrat präpariert. Adsorption, Konformation und elektronische Struktur wurden mittels konventioneller spinmittelnder Rastertunnelmikroskopie und -spektroskopie mit intramolekularer Ortsauflösung untersucht. Die spinaufgelöste elektronische Struktur wurde mittels spinpolarisierter Rastertunnelmikroskopie und -spektroskopie untersucht.

Die adsorbierten Moleküle wurden als intakte  $\text{TbPc}_2$  Doppeldecker identifiziert, und ihr Adsorptionsplatz bestimmt. Eine Spinaufspaltung des niedrigsten unbesetzten Orbitals wurde beobachtet und quantifiziert, dabei beide Spinkanäle energetisch und örtlich aufgelöst, und die räumliche Verteilung des spinaufgespaltenen Orbitals dargestellt. Aus dieser Beobachtung kann auf den Ladungszustand des Moleküls geschlossen werden: Es ist negativ gela-

den durch einen Ladungstransfer vom Substrat. Dies bedeutet insbesondere, dass der Ligandenspin, eines der Spinsysteme des Moleküls, verschwindet. Die Spinaufspaltung des Orbitals zeigt, dass dennoch eine magnetische Kopplung der Liganden des Moleküls zum ferromagnetischen Substrat besteht. Diese lässt sich auf eine direkte Kopplung der Phthalocyaninliganden zum Substrat zurückführen; eine Beteiligung des Terbiumzentrums des Moleküls ist hierzu nicht notwendig. Eine Spinpolarisation, die eindeutig dem Terbiumzentrum zuzuordnen wäre, wurde nicht beobachtet.

Die Konformationen des auf dem unmagnetischen Substrat adsorbierten  $\text{TbPc}_2$  konnten mit der Spitze des Rastertunnelmikroskops geschaltet werden. Damit konnte insbesondere ihre Chiralität an- und ausgeschaltet und die Händigkeit der Chiralität geändert werden.

Für weitere Fortschritte in der Erforschung des molekularen Magnetismus wurde eine neue Rastertunnelmikroskopanlage für die Untersuchung von Molekülen bei tieferen Temperaturen ( $T = 380 \text{ mK}$ ) und in höheren Magnetfeldern ( $B = 17 \text{ T}$ ) aufgebaut.

# Abstract

This work presents an investigation of bis(phthalocyaninato)terbium single-molecule magnets by spin-polarised scanning tunnelling microscopy and spectroscopy, as well as the construction of a scanning tunnelling microscopy system for the investigation of molecules at low temperature and in high magnetic field.

Single-molecule magnets are single molecules exhibiting a stable magnetisation, albeit short-lived and only at low temperature. A promising one is bis(phthalocyaninato)terbium ( $\text{TbPc}_2$ ), a double-decker molecule consisting of two parallel phthalocyanine ligands sandwiching a central terbium ion. Additional to the magnetic moment of the central terbium ion ( $J = 6$ ), an electron ( $S = 1/2$ ) delocalised over both ligands forms a second spin system. Both magnetic moments, their interaction, the access to these magnetic systems, and their interaction with the environment are subject of intense research.  $\text{TbPc}_2$  can be perceived as a comparably small and stable single-molecule magnet, or as a model system for paramagnetic single ions which become superparamagnetic in a molecular ligand field.

In the present work, individual  $\text{TbPc}_2$  molecules were deposited on a non-magnetic support, and a ferromagnetic support for magnetic coupling. Adsorption, conformation and electronic structure have been investigated by conventional spin-averaging scanning tunnelling microscopy and spectroscopy with sub-molecular spatial resolution. The spin-resolved electronic structure has been investigated by spin-polarised scanning tunnelling microscopy and spectroscopy.

The adsorbed molecules have been identified to be intact  $\text{TbPc}_2$  double-deckers. Their adsorption site has been determined. A spin splitting of the lowest unoccupied molecular orbital has been observed and quantified, resolving both spin channels with energy resolution and spatial resolution, and imaging the spatial distribution of the spin-split orbital. The observation of a spin splitting on this orbital reveals the charge state of the molecule. It is negatively charged due to charge transfer from the substrate. Notably, this implies that the ligand spin, one of the spin systems of this molecule,

is quenched. Still, the observation of a spin splitting of the orbital indicates that there is a magnetic coupling of the molecular ligands to the ferromagnetic support. This is caused by direct coupling of the substrate and the phthalocyanine ligands; an influence of the central terbium ion is not necessary to explain the observation. A spin polarisation stemming uniquely from the terbium centre has not been observed.

TbPc<sub>2</sub> adsorbed on the non-magnetic substrate has been found to exhibit a chiral and an achiral conformation. These conformations have been switched into each other by manipulation with the scanning tunnelling microscope tip. By switching, their chirality is turned on and off; the handedness can be changed by repeated switching.

For further progress in the investigation of molecular magnetism, a new scanning tunnelling microscopy system for the investigation of individual molecules at lower temperature ( $T = 380$  mK) and higher magnetic field ( $B = 17$  T), was constructed.

# Contents

<b>Introduction</b>	<b>1</b>
<b>I Introduction and theory</b>	<b>5</b>
<b>1 Scanning tunnelling microscopy</b>	<b>7</b>
1.1 The tunnel effect . . . . .	7
1.2 Experimental realisation . . . . .	9
1.3 Theoretical treatment of topography mode . . . . .	10
1.4 Spectroscopy mode . . . . .	11
1.4.1 Normalisation . . . . .	12
1.4.2 Tip density of states . . . . .	12
1.4.3 Tip wave function . . . . .	12
1.5 STM operation modes . . . . .	13
1.6 Spin-polarised STM . . . . .	14
1.6.1 Tip stabilisation height influence . . . . .	17
1.6.2 Evaluation of spin polarisation . . . . .	19
1.7 Imaging molecules by STM . . . . .	21
<b>2 Magnetism</b>	<b>23</b>
2.1 Superparamagnetism . . . . .	24
2.2 Magnetic molecules . . . . .	25
2.2.1 Single-molecule magnets . . . . .	25
2.2.2 Lanthanide-based SMMs . . . . .	27
2.2.3 TbPc <sub>2</sub> . . . . .	28
<b>II Instrumentation</b>	<b>31</b>
<b>3 Building a 300mK-17T-STM system</b>	<b>33</b>
3.1 Motivation . . . . .	33

3.2	Working principle and design concept . . . . .	35
3.3	Vacuum chambers overview . . . . .	43
3.3.1	Vacuum . . . . .	43
3.3.2	Materials . . . . .	44
3.3.3	Pump monitoring and valve control . . . . .	45
3.4	Preparation chamber . . . . .	46
3.4.1	Transfer stage . . . . .	46
3.4.2	Microbalance . . . . .	49
3.4.3	Stage for mobile evaporators . . . . .	49
3.4.4	Molecule deposition techniques . . . . .	50
3.4.5	Gas inlet stage . . . . .	52
3.5	LEED/Auger system . . . . .	53
3.5.1	Test measurements . . . . .	53
3.6	Satellite preparation chamber . . . . .	53
3.6.1	Electron beam heating stage . . . . .	54
3.6.2	Cooling stage . . . . .	56
3.7	STM chamber . . . . .	57
3.7.1	Molecule evaporator stage . . . . .	57
3.7.2	Storage cupboard . . . . .	59
3.8	Microscope . . . . .	59
3.8.1	Wiring . . . . .	61
3.8.2	Tip exchange . . . . .	63
3.9	Labview control . . . . .	63
3.9.1	Microbalance . . . . .	64
3.9.2	Automated sample cleaning . . . . .	64
3.9.3	Temperature control . . . . .	64
3.9.4	Quick heating of molecule evaporators . . . . .	64
3.10	Sample transfer . . . . .	65
<b>III Experimental results and discussion</b>		<b>67</b>
<b>4</b>	<b>SP-STM investigation of TbPc<sub>2</sub></b>	<b>71</b>
4.1	Magnetic substrate system . . . . .	72
4.2	Experimental setup . . . . .	74
4.2.1	Sample preparation . . . . .	75
4.2.2	Tip preparation . . . . .	75
4.3	Spin-averaged investigation of TbPc <sub>2</sub> on Co/Ir(111) . . . . .	76
4.3.1	Decomplexation . . . . .	79
4.3.2	Analysis of molecular adsorption . . . . .	82
4.3.3	Conformations . . . . .	85

4.4	Spin-resolved investigation . . . . .	86
4.4.1	Constant-current mode measurements . . . . .	86
4.4.2	Constant-height mode measurements . . . . .	96
4.4.3	Occupied states . . . . .	98
4.4.4	Spin-resolved point spectroscopy . . . . .	99
4.5	Discussion and Outlook . . . . .	102
<b>5</b>	<b>TbPc<sub>2</sub> on Ir(111)</b>	<b>111</b>
5.1	Chiral conformation . . . . .	112
5.1.1	Orientation . . . . .	115
5.2	Achiral conformation . . . . .	115
5.3	Switching . . . . .	118
5.3.1	Switching the chiral conformation into the achiral conformation . . . . .	118
5.3.2	Switching the achiral conformation into the chiral conformation . . . . .	123
5.3.3	Chirality change . . . . .	124
5.3.4	Geometrical structure of the conformations . . . . .	125
5.4	Summary . . . . .	126
	<b>Summary</b>	<b>129</b>
	<b>Bibliography</b>	<b>138</b>
	<b>Publications</b>	<b>139</b>
	<b>Talks and poster presentations</b>	<b>141</b>
	<b>Acknowledgement</b>	<b>143</b>



# Introduction

For many decades, progress in information technology has been driven by ever progressing miniaturisation of functional structures in microchips, leading to exponential increase of both processing speed and data storage density and capacity. Now, miniaturisation of manufacturing processes and structure size approaches fundamental limits, such as the wavelength of ultra-violet light employed in photolithography and lack of control to position atoms at will in top-down manufacturing processes. Molecules as building blocks of nanoscale electronics promise to solve these problems. Single magnetic molecules can store information, the direction of their magnetic moment (up and down) defines a bit. In contrast to top-down techniques employed in silicon electronics, synthesis of molecules yields monodisperse objects, i.e. the molecules are identical. Molecular self-assembly provides a bottom-up fabrication technique for precise manufacturing on the nanoscale. The key here is to transfer the problem of assembling devices to a well-established technique: chemistry. Self-assembly requires control over appropriate functional units on the molecule, which can be added by synthesis. Access to the large existing toolbox of chemistry offers a high degree of control, comes at comparably low cost, and also enables further functionalisation, for example sensitivity to light or other external stimuli to control different states of the molecule. Molecules promise to be employed as building blocks of molecular spintronics, where the electron's spin degree of freedom is exploited [1]. Spin valves [2] and multiple-field-effect nanotransistors [3] have been demonstrated. In the future, molecules could also be exploited in quantum computing [4, 5], which promises significant progress for computation.

Magnetism has been found for several classes of molecules. Arrays of magnetic molecules couple ferromagnetically, organic radicals show magnetism of purely organic origin, and metalorganic molecules can show magnetic behaviour stemming from their metal centres. However, nearly all magnetic single molecules are paramagnetic only, and their magnetic moment does not retain its direction after removal of an external magnetic field. One solution is the addition of a ferromagnetic support to obtain metal-molecule hybrids,

another has been found only recently: single-molecule magnets (SMM) are superparamagnetic molecules, i.e. below a certain blocking temperature, they show slow relaxation of magnetisation after removal of an external magnetic field. In 1993, Sessoli *et al.* found the molecular cluster  $\text{Mn}_{12}$  to exhibit hysteresis [6]. Unfortunately, this and similar single-molecule magnets coupling several transition metals to form one giant spin require temperatures well below 10 Kelvin to show magnetic blocking. In 2003, Ishikawa *et al.* found a molecule containing a single lanthanide atom,  $\text{TbPc}_2$ , to show phase lag in ac magnetisation measurements at up to 40 K [7]. Since then, more single-molecule magnets containing only one lanthanide atom, therefore sometimes coined SIMM, single-ion molecular magnets, have been found. Their high magnetic anisotropy stems from the 4f electrons of a lanthanide ion, whose easy-axis magnetisation direction is stabilised by the ligand field provided by its environment, in this case the molecular ligands [8]. Similarly, single-ion magnets are stabilised by the atomic environment of a carefully chosen surface system [9, 10]. Therefore, understanding and control of the environment is crucial for the properties of SMMs. The central terbium ion in  $\text{TbPc}_2$  is sandwiched by two phthalocyanine ligands. Phthalocyanines provide a comparably stable environment, are robust, well-known in science and in application, for example as dyes. Individual  $\text{TbPc}_2$  molecules can be adsorbed intact on metal surfaces, preserving their SMM properties [11, 12]. Vitali *et al.* found fingerprints of 4f states by spin-averaging STM [11].

Spin-polarised scanning tunnelling microscopy (SP-STM) and spectroscopy (SP-STs) is an experimental technique which employs tips with a spin-polarised density of states to resolve spin contrast on the surface with near-atomic spatial resolution. The technique has been successfully used to discern spin contrast on interesting magnetic surface systems [13] and, more recently, on molecules as well. A ferromagnetic coupling of a molecular metal centre to a ferromagnetic support was shown [14], as well as newly arising spin-polarised molecule–substrate hybrid states [15, 16]. To this point, SP-STM has not presented spin-polarised pristine molecular orbitals.

In the present work, Terbium- $\text{Pc}_2$  single-molecule magnets are investigated by SP-STM. The adsorption on a ferromagnetic and a non-magnetic substrate is studied, and the spin structure investigated by SP-STM. For future experiments, a new STM setup operating with higher magnetic field and at lower temperature has been built. Its design dedicated for the preparation of molecular systems, and the yet lower temperature meet the requirements of studies of single-molecule magnets.

This thesis is composed of three major parts, an introduction, a description of the newly built experimental setup, and an experimental part presenting two different experiments.

The first part provides an introduction into the experimental technique and its theoretical background as well as the magnetic molecule investigated in the third part.

The second part describes the newly designed STM setup built in this PhD work, with a focus on new developments introduced into the machine.

The third, experimental part is divided into two chapters, tackling the same molecule but investigating different effects. In the first chapter, spin-polarised tunnelling microscopy and -spectroscopy is employed to investigate the spin-resolved density of states of an individual TbPc<sub>2</sub> molecule adsorbed on a ferromagnetic substrate. The chapter first discusses basic work such as sample preparation, discussion of adsorption onto the substrate and spin-averaged characterisation of the electronic structure, before studying and discussing the spin-resolved electronic structure and the new findings. The second chapter presents the unrelated effect of switching conformations found on the same molecule adsorbed on a different, non-magnetic substrate. It first discusses the chiral, then the achiral conformation, and finally the switching between these conformations. Finally, the results of the experimental part are summarised.



# Part I

## Introduction and theory



# Chapter 1

## Scanning tunnelling microscopy

This chapter gives a short introduction into scanning tunnelling microscopy (STM), its working principles, and its implementation into an experimental setup. Spin-polarised scanning tunnelling microscopy (SP-STM) is described in more detail.

Scanning tunnelling microscopy is a tool to image surfaces and nanoscale objects with sub-nanometre spatial resolution. An atomically sharp tip is scanned line by line in a distance of a few ångström over the surface. Due to the quantum mechanical tunnelling effect, a small tunnelling current flows when a bias voltage is applied between tip and sample. Due to an exponential dependence of this current on the tip-sample distance, the recorded current is very sensitive to surface corrugation, and even atomic resolution can be achieved. Scanning tunnelling microscopy was first demonstrated by Binnig, Rohrer, and Gerber in 1982 [17]. In 1986, Binnig and Rohrer were awarded the Nobel prize for their achievements.

### 1.1 The tunnel effect

The quantum mechanical tunnel effect explains how electrons pass through an energy barrier higher than their kinetic energy, thus impenetrable for classical particles. The transmission probability of the electrons is found to depend exponentially on the barrier height and width. This effect is exploited in STM, where the energy barrier is given by the vacuum between tip and sample. The exponential dependence of the tunnelling current on the tip-sample distance gives rise to the high spatial resolution of STM. This section presents a sketch of the derivation of the exponential dependence for the one-dimensional tunnel effect.

Figure 1.1 shows a potential barrier with height  $V_0$  and width  $d$ . An

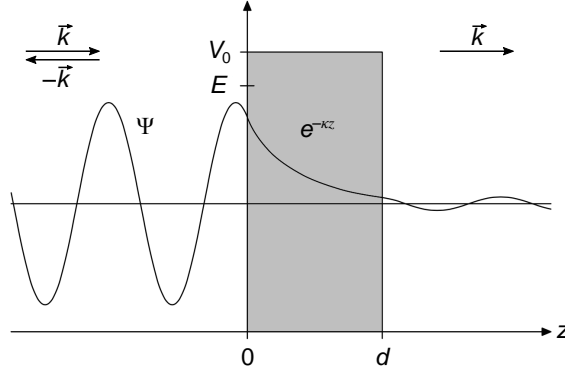


Figure 1.1: **One dimensional tunnelling through an energy barrier.** Before and behind an energy barrier of height  $V_0$  and width  $d$ , a free electron is described by a plane wave. Within the barrier, the probability density decreases exponentially towards the end of the barrier.

electron with mass  $m_e$  has a kinetic energy  $E < V_0$ . In classical mechanics, the electron could therefore not overcome the barrier. In quantum mechanics, the electron is described by a wave function  $\Psi$ , fulfilling the time-independent Schrödinger equation in one dimension,

$$E\Psi(z) = -\frac{\hbar^2}{2m_e} \frac{d^2}{dz^2} \Psi(z) + V(z)\Psi(z) \quad (1.1)$$

The solution for  $\Psi(z)$  is

$$\Psi(z) = \begin{cases} Ae^{ikz} + Be^{-ikz} & \text{for } z < 0 \text{ (before the barrier)} \\ Ce^{\kappa z} + De^{-\kappa z} & \text{for } 0 < z < d \text{ (in the barrier)} \\ Ee^{ikz} & \text{for } z > d \text{ (behind the barrier)} \end{cases} \quad (1.2)$$

with  $k = \frac{1}{\hbar} \sqrt{2m_e E}$  and  $\kappa = \frac{1}{\hbar} \sqrt{2m_e (V_0 - E)}$ . Outside the barrier,  $\Psi$  describes a particle with wave vector  $k$  moving in  $z$  direction. In the barrier, i.e. the classically forbidden region,  $\Psi$  decays exponentially with decay constant  $\kappa$ . This means there is a finite probability to find the electron in the classically forbidden region. For STM, the experimentally relevant quantity is the transmission coefficient, i.e. the ratio between transmitted and incident current. It is determined from the solution of 1.2, with the coefficients determined by fulfilling matching conditions at the boundaries, and assuming a barrier much higher than the electron energy.

$$T = \frac{I_{\text{trans}}}{I_{\text{in}}} \approx e^{-2\kappa d} \quad (1.3)$$

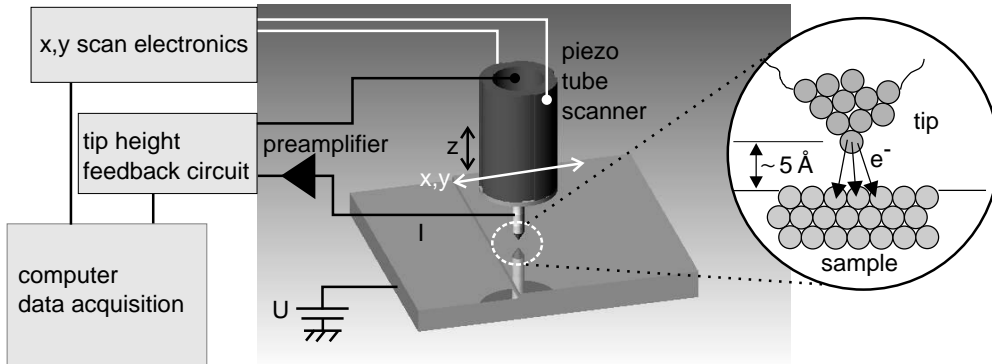


Figure 1.2: **Schematic of STM.** A bias voltage is applied between tip and sample. The low tunnelling current is amplified and recorded. The tip is held in a piezo tube allowing for motion in all 3D directions by applying high voltages. A topograph is recorded by scanning the tip line by line over the sample. Source: [18]

In STM experiments,  $d$  corresponds to the width of the vacuum barrier, i.e. the tip–sample distance.  $V_0$  corresponds to the work function of the electrodes (typically 4...5 eV). From this, the decay constant  $\kappa$  can be estimated, and the current is found to drop by about one order of magnitude when the tip is retracted by one ångström.

## 1.2 Experimental realisation

The quantum mechanical tunnelling effect described in the last section is employed in scanning tunnelling microscopes. In these systems, an atomically sharp metal tip is brought into close contact (a few ångströms) to an almost planar, electrically conducting surface. A bias voltage ( $\sim 1$  V) applied between tip and sample results in a small tunnelling current ( $\sim 1$  pA... 1 nA). The tip is scanned line by line over the surface, and its height is modified by a feedback loop to keep the tunnelling current constant. The recorded vertical tip displacement as a function of spatial coordinates  $(x,y)$  gives the STM topograph. The ultimate lateral resolution (down to atomic resolution) of STM is due to the exponential dependence of the current on the tip–sample distance. The subatomic displacement of the tip is achieved by a piezo-electric scanner tube (of macroscopic,  $\sim 3$  cm, size) controlling both lateral and vertical motion of the tip with picometre precision. High voltages of  $\lesssim 300$  V are applied to move the piezo scanner. Atomically sharp tips are obtained quite easily, for example by etching processes. Careful design is

necessary to block external vibrational noise from the tip–sample junction.

### 1.3 Theoretical treatment of topography mode

A more detailed approach of the tunnelling process was developed by Bardeen [19], who investigated planar electrodes. Assuming a simplified STM junction geometry, Tersoff and Hamann [20, 21] found that STM topography maps represent contours of equal local density of states (LDOS).

Time-dependent perturbation theory describes a system with two separate subsystems for the electronic states of two electrodes (in this case tip and sample) in weak tunnelling contact. The stationary Schrödinger equation can then be solved; the matrix element  $M_{\mu\nu}$  describes the transmission rate of the tunnelling between tip states  $\psi_\mu$  and sample states  $\psi_\nu$ .

$$M_{\mu\nu} = -\frac{\hbar^2}{2m_e} \int d\vec{S} (\psi_\mu^* \vec{\nabla} \psi_\nu - \psi_\nu \vec{\nabla} \psi_\mu^*) \quad (1.4)$$

where the integral is taken over a surface between the two electrodes. The tunnelling current is determined by summing over all tip and sample states which contribute to an elastic, i.e. energy-conserving, tunnelling process:

$$I = \frac{2\pi e}{\hbar} \sum_{\mu,\nu} \{f(E_\mu)[1-f(E_\nu+eU)] - f(E_\nu+eU)[1-f(E_\mu)]\} |M_{\mu\nu}|^2 \delta(E_\mu - (E_\nu + eU)) \quad (1.5)$$

where  $f(E)$  is the Fermi function, and tunnelling in both directions is included. The tunnelling current thus depends on the overlap of tip and sample wave functions, as described by  $M_{\mu\nu}$ . For low temperatures, the Fermi function approaches a step function. For low bias voltage (compared to the work function of  $\sim 5$  (e)V) and a simplified geometry (Figure 1.3) assuming a spherical tip apex (and thus spherical, i.e. s-wave, tip wave functions), Tersoff and Hamann [20, 21] derived a simpler expression:

$$I \propto \sum_{\nu} |\psi_\nu(\vec{r}_0)|^2 \delta(E_\nu - E_F) \quad (1.6)$$

where the right-hand side of the equation equals the definition of the sample local density of states (LDOS) at the position  $\vec{r}_0$  of the tip apex and at energy  $E_\nu - E_F$ . When operating in constant-current (“topography”) mode, the STM tip thus follows a surface of constant LDOS of the sample.

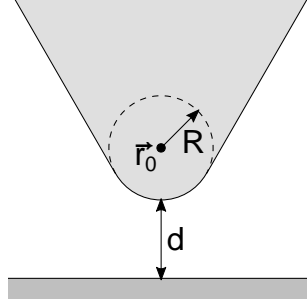


Figure 1.3: **Simplified geometry of the tunnelling junction**, with tip apex radius  $R$  at position  $\vec{r}_0$ , and tip-sample distance  $d$  forming the vacuum barrier. Image adopted from [21]

## 1.4 Spectroscopy mode

Apart from imaging, STM can also be employed to investigate the electronic structure of a sample. In scanning tunnelling spectroscopy (STS), the STM tip is kept in a fixed position, a voltage ramp is driven and the resulting tunnelling current recorded. To increase signal-to-noise ratio, the derivative  $dI/dU$  is determined by adding a quickly (kHz) alternating low voltage onto the bias voltage; the response of the tunnelling current is recorded via lock-in technique. Plotting  $dI/dU$  against  $U_{\text{bias}}$  gives a  $dI/dU$  spectrum, which is strongly related to a spectrum of the local density of states (LDOS) of the sample. This is briefly explained in this section.

The sum in equation 1.5 can be replaced by an integral, integrating over the density of states instead of summing over separate wave functions. Replacing the Fermi function by a step function gives

$$I = \frac{2\pi e}{\hbar} \int_{E_F}^{E_F+eU} \rho_s(E) \rho_t(E - eU) |M|^2 dE \quad (1.7)$$

with  $\rho_{s/t}$  the density of states of sample and tip, and the tunnelling matrix element  $M$  generalised from  $M_{\mu\nu}$ . This expression is symmetric with respect to tip and sample density of states, which therefore contribute equally to the tunnelling current. Assuming that the tunnelling matrix element  $M$  and the tip LDOS do not change appreciably over the investigated energy interval, the derivative  $dI/dU$  is simply:

$$\frac{dI(U)}{dU} \propto \rho_s(E_F + eU) \quad (1.8)$$

The derivative of the tunnelling current is, in first approximation, proportional to the LDOS of the sample at the position of the tip; the STS  $dI/dU$

point spectrum therefore approximately represents the energy-dependent LDOS of the sample.

### 1.4.1 Normalisation

The assumption of a constant, or slowly changing density of states for the tip is appropriate for clean and blunt metal tips, but adsorption of molecules or molecular parts on the tip apex often give pronounced features on the tip LDOS. To experimentally isolate a feature of the tip LDOS from STS spectra, reference spectra over clean metal surface spots are taken. To directly compare different spectra taken in the course of an experiment, the tip shall not change.

To compensate for an energy dependence of the tunnelling matrix element  $M$  as well as for a slowly changing tip LDOS  $\rho_t$ , a number of corrections for  $dI/dU$  spectra have been suggested [22, 23]. A very simple normalisation is the division of  $dI/dU$  by  $(I/U)$ , where  $I$  is simply the tunnelling current recorded alongside with the  $dI/dU$  signal. Feenstra *et al.* [23] argue that the energy dependence of the tunnelling barrier influences  $dI/dU$  and  $(I/U)$  similarly, and therefore cancels out in the quotient.

### 1.4.2 Tip density of states

Above, the energy dependence of the tip density of states was assumed to be low, and the  $dI/dU$  spectrum could then be identified with the LDOS of the sample. For a significantly energy-dependent tip LDOS, this is not the case. Equation 1.7 is symmetric with respect to tip and sample LDOS, so both contribute to the  $dI/dU$  spectrum. Ukraintsev [22] shows that the negative bias voltage (applied to the sample) side of the spectrum rather reflects the tip density of states whereas the positive bias side is dominated by the sample LDOS. Tunnelling from occupied states close to the Fermi level into unoccupied states thus dominates over tunnelling from high-energy occupied states to unoccupied states close to the Fermi level. This can be understood when looking at the tunnelling barrier. In the former case, the tunnelling electrons have higher energy and therefore give a higher contribution to the tunnelling current.

### 1.4.3 Tip wave function

Tersoff and Hamann described the tip apex by an s-like wave function. However, typical (SP-)STM tip apex materials are tungsten, iron or chromium, i.e. d metals. Chen [24] found that the matrix element  $M$  is proportional to

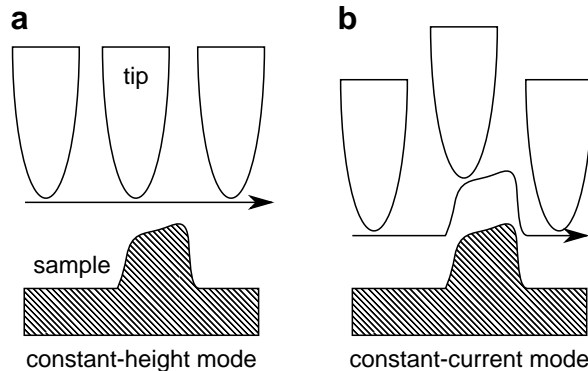


Figure 1.4: **Topography operation modes of STM.** (a) Constant-height mode. The tip scans over the surface at a constant height. The topograph is given by the variation of the tunnelling current. (b) Constant-current mode. A feedback loop is used to keep the tunnelling current constant by adjusting the tip height. The topograph is given by the tip height.

spatial derivatives of the sample wave function for tip orbitals with quantum number  $l > 0$ . Thus, imaging depends on the orbital type of the tip wave function. Gross *et al.* [25] used tips functionalised by picking up CO molecules to image the electronic structure of pentacene molecules. The CO tip apex has a strong contribution of p orbitals and is more sensitive to molecular sample wave functions changing phase, as the tip wave function does. A similar effect can often be seen in STM on molecules. After accidentally adsorbing a molecule or molecular parts on the tip apex, surface molecules often appear different compared to imaging with clean metal tips. They show higher-frequency corrugation, possibly reflecting a similar sensitivity. In view of imaging 4f orbitals, these results are interesting as choosing an appropriately functionalised tip apex might enhance its sensitivity to these orbitals.

## 1.5 STM operation modes

STM topography imaging can be performed in two different modes. In “constant-height mode” the tip height is fixed<sup>1</sup> while scanning (Figure 1.4a), and the image is given by the spatial variation of the tunnelling current, which depends on the tip–sample distance and thereby on the surface corrugation. In “constant-current mode” (Figure 1.4b), the tunnelling current

<sup>1</sup>Experimentally, the Z piezo voltage is kept constant with a linear addition to compensate for an inclination of the sample plane.

is kept constant by a feedback loop adjusting the tip height accordingly, and the image is given by the tip height profile. Both modes have advantages and disadvantages and are therefore chosen depending on the purpose. Most importantly, the constant-current mode optimises the signal-to-noise ratio, whereas constant-height mode data are easier to analyse and to compare with each other and to theory, as the tip height does not depend on the electronic structure of sample and tip.

### Maps of differential conductance

Maps of differential conductance (“ $dI/dU$  map”) combine spatial resolution and energy sensitivity of STM. They are recorded simultaneously with topographs in either constant-current or constant-height mode. A small, quickly alternating (kHz) voltage is added onto the bias voltage, the response of the tunnelling current recorded, and the derivative  $dI/dU$  determined by lock-in technique. The map gives the LDOS at the bias voltage, taken in the plane described by the scanning tip. The topograph can be recorded in either constant-current or constant-height mode. The constant-current mode ensures a high current and thereby  $dI/dU$  signal, but the tip plane is determined by the total density of states from the Fermi level to the bias voltage; constant-current mode  $dI/dU$  maps therefore not only monitor the LDOS at the bias voltage, but are influenced by the LDOS at lower bias voltage.

### Point spectroscopy mode

STS spectra are taken in so-called point spectroscopy mode. The tip is stabilised above the point of interest with the stabilisation height defined by the bias voltage and the tunnelling current. Then, a voltage ramp is driven and the tunnelling current recorded. To increase the signal-to-noise ratio, again a lock-in technique is used to determine the derivative  $dI/dU$ .

## 1.6 Spin-polarised STM

In the preceding discussion, the tunnelling electrons were treated as simple charged particles, while their spin degree of freedom was not discussed. Spin sensitivity is achieved by spin-polarised scanning tunnelling microscopy, abbreviated SP-STM or SPSTM. To obtain spin sensitivity, tips coated with magnetic material are used. The magnetic tip acts as a spin filter, and the tunnelling current depends on the relative orientation of tip and sample magnetisation. The key advantage of this technique is the combination of

spin sensitivity with the energy sensitivity and the high spatial resolution of STM [13].

Figure 1.5 shows a schematic of SP-STM, simplified to one dimension. Tip and sample magnetisation are aligned parallel (Fig. 1.5a) or antiparallel (Fig. 1.5b). Both tip and sample have a spin-dependent local density of states. Neglecting spin-flip and other inelastic processes, spin and energy of the tunnelling electrons are conserved. The spin asymmetry leads to a larger total current (the sum of spin up and spin down currents) for the parallel than for the antiparallel case. These total currents are recorded by conventional spin-averaging current amplifiers for both alignments. An effective spin polarisation is derived from the difference of these currents. Whereas Figure 1.5 depicts sample areas with opposite magnetisation, parallel and antiparallel alignment can also be achieved by rotating the tip's magnetisation and measuring the same surface area.

(Spin) polarisation is defined as the difference of density of states of opposite spin channels, normalised by their sum:

$$P = \frac{\rho_{\uparrow\uparrow} - \rho_{\uparrow\downarrow}}{\rho_{\uparrow\uparrow} + \rho_{\uparrow\downarrow}} \quad (1.9)$$

The magnetisation direction of the tip acts as quantisation axis of the spin of the tunnelling electrons. Slonczewski [26] found for the tunnelling conductance at low (bias) voltages:

$$\sigma = \sigma_0[1 + P_T P_S \cos\theta] \quad (1.10)$$

with  $\sigma_0$  the spin-averaged tunnelling conductance,  $P_T$  and  $P_S$  effective (tunnelling barrier dependent) spin polarisations of tip and sample, and  $\theta$  the angle between tip and sample magnetisation directions.

Spin-polarised scanning tunnelling spectroscopy (SP-STs) was theoretically investigated by Heinze [27], who found a very similar result:

$$\frac{dI}{dU}(\vec{r}, eU, \theta) \propto \rho_T \cdot \rho_S(\vec{r}, E_F + eU) \cdot [1 + P_T \cdot P_S(\vec{r}, E_F + eU) \cdot \cos\theta] \quad (1.11)$$

with  $\rho_T$  and  $P_T$  the LDOS and spin polarisation of the tip, and  $\rho_S(\vec{r}, E_F + eU)$  and  $P_S(\vec{r}, E_F + eU)$  the LDOS and spin polarisation of the sample at the position of the tip and at an energy shifted by the bias voltage  $U$ . The  $dI/dU$  signal thus depends on the relative orientation of tip and sample magnetisation directions as in equation 1.10, and depends on both tip and sample density of states.

Experimentally, the differential conductance of the spin channels is used to calculate an asymmetry [28], also called spin asymmetry [29] or magnetic

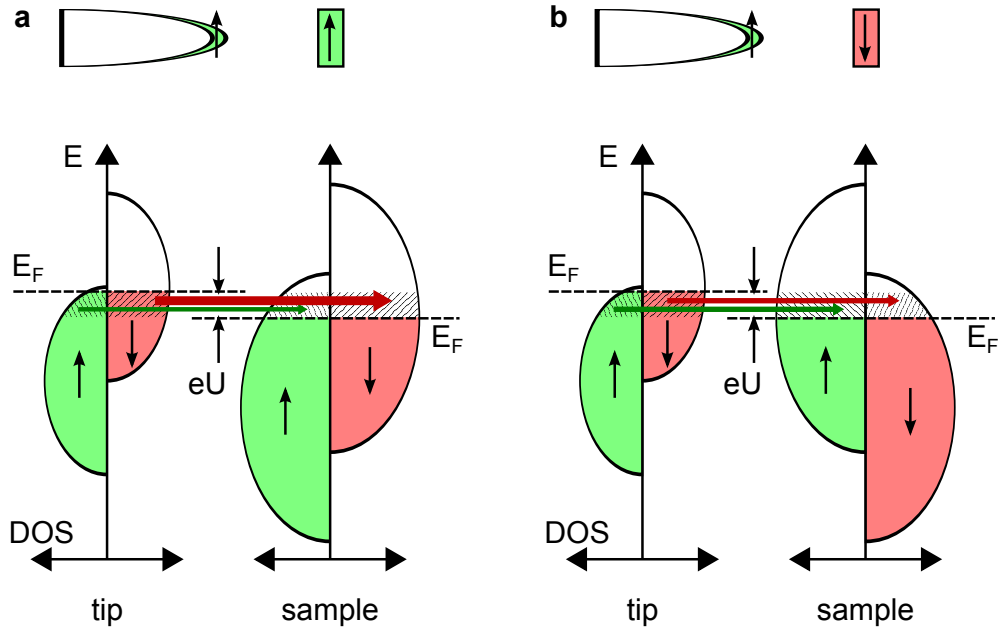


Figure 1.5: **Schematic of spin-polarised tunnelling.** The spin-polarised local density of states of tip and sample is sketched for parallel (a) and antiparallel (b) alignment of tip and sample magnetisation. A bias voltage is applied, and spin-up and down electrons tunnel elastically from occupied tip states into unoccupied sample states. Here, the tip LDOS contributing to the tunnelling process is higher for spin down; in (a), the same holds for the sample. Therefore, there is a high current of spin-down electrons and a low current for spin-up. Likewise, investigating a surface region with reversed magnetisation (b) yields small currents for both spin channels and thus a smaller total current than for the parallel case. This difference in total current is detected by spin-averaging amplifiers and provides information about the spin polarisation.

asymmetry [30]:

$$A = \frac{(dI/dU)_{\uparrow\uparrow} - (dI/dU)_{\uparrow\downarrow}}{(dI/dU)_{\uparrow\uparrow} + (dI/dU)_{\uparrow\downarrow}} \quad (1.12)$$

The  $dI/dU$  signal slightly depends on the tip height, which is not necessarily identical for both spin channels, as explained in more detail in the following section. A correction for this small effect is possible, and a spin asymmetry calculated from these corrected quantities  $dI/dU_{\uparrow\uparrow, \text{corr}}$ , or from  $dI/dU$  signals taken with equal tip height, is called the effective spin polarisation.

$$SP_{\text{eff}} = \frac{(dI/dU)_{\uparrow\uparrow, \text{corr}} - (dI/dU)_{\uparrow\downarrow, \text{corr}}}{(dI/dU)_{\uparrow\uparrow, \text{corr}} + (dI/dU)_{\uparrow\downarrow, \text{corr}}} \quad (1.13)$$

Magnetic tips are obtained by coating conventional tungsten tips with magnetic material, e.g., iron or chromium. Iron coated tips are ferromagnetic; the iron film acts as soft magnet, its magnetisation direction is rotated by an external magnetic field. Chromium coated tips are antiferromagnetic and maintain the spin direction of the front tip atom in external magnetic fields. Iron coated tips are used to change the spin sensitivity of the tip to access both spin channels of a sample hardly affected by the external field [13], whereas chromium coated tips are for example suitable for spin-resolved investigation of field dependent effects [31, 13]. Recently, bulk chromium tips have been employed successfully [32, 33]. This is relevant for STM setups with high magnetic fields as the one built in this work ( $B = 17 \text{ T}$ ), as antiferromagnetic bulk chromium tips are stable in high external magnetic fields. A combination of magnetic and functionalised tips (as described in section 1.4.3) to resolve spin and orbital character of the sample wave function has not been reported yet. SP-STM with conventional coated tips requires the possibility of in-situ tip exchange and facilities for in-situ tip preparation to renew the tip coating material when it is lost due to inevitable tip manipulations.

### 1.6.1 Tip stabilisation height influence

The evaluation of SP-STM data relies on the comparison of two spin channels obtained in two separate measurements. For a direct comparison of both  $dI/dU$  maps and point spectroscopy data, the tip height needs to be equal for both spin channels to ensure equal overlap of tip and sample wave functions. The tip height can however differ, as it is defined by the spin-dependent LDOS of the respective spin channel both in point spectroscopy and topography mode.

In point spectroscopy mode, the tip stabilisation height for given stabilisation parameters  $U_{\text{stab}}$  and  $I_{\text{stab}}$  is defined by the integral over the LDOS

of the respective spin channel. A higher SP-LDOS in one spin channel gives higher tunnelling current at a given tip height; the tip therefore stabilises farther away from the substrate for this spin channel in order to lower the tunnelling current and reach the same stabilisation current  $I_{\text{stab}}$ . The tip being farther away from the substrate is less sensitive to the sample LDOS at all energies. A non-spin-polarised feature at a certain energy is therefore perceived to be weaker in this spin channel compared to the other; the spin asymmetry calculated from these measurements then gives an artefact non-zero value for a non-spin-polarised feature.

Similarly, taking a spin-resolved constant-current topograph at a bias voltage above a spin-polarised feature makes the tip follow a trajectory with higher tip-sample distance for the spin channel with higher SP-LDOS between the Fermi level ( $E_F$ ) and the bias voltage. While comparison of the topographs reveals the integrated spin asymmetry [34],  $dI/dU$  maps taken at these differently high planes again suffer from different tip sensitivity.

To avoid these caveats from different tip stabilisation height, several approaches are possible:

- The tip is stabilised at a bias voltage where the stabilisation height for both spin channel equals, either because the spin polarisation from  $E_F$  to this bias voltage is zero, or because their integrated spin polarisation vanishes.

A bias voltage with vanishing spin polarisation until  $E_F$  does not always exist, as some systems exhibit SP (directly) around  $E_F$ . The latter option is not perfectly precise as the integrated polarisation can differ for different tips, because the integrated spin polarisation also depends on the spin polarisation of the tip LDOS. In addition, this method is applicable only to measuring modes relying on a single initial height, such as point spectroscopy and constant-height maps. For the starting height of a constant-height map, the data acquisition system needs to provide an option for defining individual start and recording voltages. The version of the data acquisition software used in this work did not provide this option.

- The tip is stabilised above a non-magnetic area on the surface, then moved towards the area of interest with predefined height changes only. This is feasible for a constant-height image which starts above a non-magnetic area and includes the spin-polarised area. For point spectroscopy the acquisition system needs to provide an option for separate stabilisation and measuring positions. However, not all substrate systems provide non-magnetic regions.

- If the data set includes non-spin-polarised reference data, a correction of spin-resolved data is feasible. From the information about the tip height over a non-magnetic reference (e.g., a constant-current image recorded above both non-magnetic as well as spin-polarised areas), the relative tip displacement (comparing the height  $z$  for the two channels) can be obtained. The measured data set can then be corrected by multiplication with a factor  $e^{\kappa z}$  to compensate for the different tip heights.

This correction can also be applied to recover constant-height  $dI/dU$  maps from constant-current  $dI/dU$  maps. Again, the tip height  $z$  from the constant-current topograph is used to correct the constant-current  $dI/dU$  signal by a factor  $e^{\kappa z}$ . For comparison of spin channels with tip height differences of only about  $\Delta z \lesssim 10$  pm, a typical  $\kappa = 2 \text{ \AA}^{-1}$  is sufficient. For a full recovery of constant-height maps from constant-current data, the height variation is given by the larger corrugation of the surface ( $\Delta z \sim 200$  pm), and the tunnelling barrier dependent  $\kappa$  needs to be determined individually by  $I(z)$  spectra.

In summary, to reliably obtain spin difference and effective spin polarisation, either an appropriate scheme or correction of raw spin-resolved  $dI/dU$  data is necessary.

### 1.6.2 Evaluation of spin polarisation

Spin polarisation denotes the degree of asymmetry of spin-dependent density of states. While the experimentally determined effective spin polarisation provides a quantity to determine the magnitude of this effect, I argue here that the simple difference of the spin channels without normalisation by the sum provides more accurate information about the density of states of the spin-polarised molecular orbitals. Calculating the difference of the spin channels makes non-spin-polarised contributions vanish, therefore it only contains information of spin-polarised states. Division by the sum of the two spin channels provides a normalisation and gives the effective spin polarisation, but also reintroduces non-SP contributions. This shall be discussed in this subsection.

To understand the quantities spin difference and spin asymmetry, let's start with equation 1.11, set  $\theta = 0^\circ$  ( $180^\circ$ ) for the up (down) channel, and abbreviate  $\rho_S := \rho_S(\vec{r}, E_F + eU)$ . Spin difference and spin asymmetry (based on corrected  $dI/dU$  signals to equal the effective spin polarisation for this

discussion) then give

$$(dI/dU)_{\text{up/down}} \propto \rho_T \rho_S \cdot [1 \pm P_T P_S] \quad (1.14)$$

$$\begin{aligned} \text{diff}(dI/dU) &:= (dI/dU)_{\text{up}} - (dI/dU)_{\text{down}} \\ &\propto \rho_T \rho_S \cdot [1 + P_T P_S] - \rho_T \rho_S \cdot [1 - P_T P_S] = 2\rho_T \rho_S P_T P_S \end{aligned} \quad (1.15)$$

$$A(dI/dU) := \frac{(dI/dU)_{\text{up}} - (dI/dU)_{\text{down}}}{(dI/dU)_{\text{up}} + (dI/dU)_{\text{down}}} = \frac{2\rho_T \rho_S P_T P_S}{2\rho_T \rho_S} = P_T P_S \quad (1.16)$$

The spin difference is proportional to a product of spin and sample density of states and spin polarisations, and the spin asymmetry is found to equal the product of tip and sample polarisation, as defined above. For simplicity, let's assume density of states  $\rho_T$  and polarisation  $P_T$  of the tip to be constant. The spin asymmetry then is simply proportional to the sample polarisation  $P_S$ .

In a very simplified picture, only one spin-polarised molecular orbital, assumed to only weakly interact with the substrate, contributes to the tunnelling current. In this simplified picture, the spin polarisation of the molecular orbital is defined by the number of its spin-up and spin-down electrons, which does not depend on the spatial position in the orbital ( $P_S(\vec{r}) = \text{const}$ ). As the spin asymmetry is proportional to this sample spin polarisation (equation 1.16), the spin asymmetry does not exhibit any spatial dependence either; a map of spin asymmetry shows no spatial resolution in this approximation. In contrast, the spin difference also depends on the sample density of states (equation 1.15); a spin-difference map therefore represents a map of the spatial distribution of the molecular orbital's density of states.

In the spin asymmetry, non-spin-polarised contributions to the tunnelling current are reintroduced by the sum in the denominator; this reduces the spin asymmetry where the molecular orbital exhibits a lower LDOS and other conduction channels contribute a higher fraction.

Conclusions for spin-sensitive point spectra are similar to the discussion for maps. Spin-difference maps display the spatial distribution of the LDOS of the spin-polarised orbital, and spin-difference point spectra its energy dependence. The spin asymmetry provides a measure for the spin polarisation of the spin-polarised orbital probed at the respective energy.

A map of spin asymmetry therefore shows where a spin-polarised orbital contributes to the tunnelling current, and provides a contrastable measure of the strength of the effect. A map of the difference of the spin channels on the other hand maps the (LDOS of the) spin-polarised molecular orbital.

Similarly, spin-asymmetry point spectra provide a measure for the spin polarisation as a function of energy, but spin-difference point spectra represent the LDOS( $E$ ) of the spin-polarised orbital; this quantity must be used to determine peak positions and widths.

To summarise this section, spin-resolved constant-current-mode  $dI/dU$  maps require normalisation by the simultaneously recorded topography signal in order to produce correct spin-difference or spin-asymmetry  $dI/dU$  maps. Spin-resolved constant-height mode  $dI/dU$  maps require a well-defined tip stabilisation, i.e. independent of the spin channel, or need to be corrected accordingly. Strategically, experimentally less demanding uncorrected spin-resolved constant-current maps can still be appropriate to give a first overview of spin-polarised effects. Spin-resolved  $dI/dU$  point spectra similarly need a well defined tip stabilisation height, or correction. (Constant-height mode) spin-difference  $dI/dU$  maps image spin-polarised orbitals, whereas spin-asymmetry maps reveal the magnitude of the spin polarisation. Similarly, for (normalised)  $dI/dU$  point spectra, the spin difference provides the LDOS of the spin-polarised orbitals, whereas the energy-dependent spin asymmetry again shows the magnitude of the spin polarisation.

## 1.7 Imaging molecules by STM

STM can be applied to investigate molecular systems on surfaces. Directly adsorbed on magnetic metallic substrates, molecules often chemisorb, i.e. they form bonds to the surface. This influences the molecule, its geometry, electronic structure, charge state, and magnetic properties. An appropriate substrate therefore needs to be chosen with care.

As the magnitude of the tunnelling current depends on the overlap of tip and sample wave functions, molecular orbitals decaying far into the vacuum contribute more strongly to the signal. This is the case for example for molecular  $\pi_z$  or atomic  $d_{z^2}$  orbitals, whereas  $\sigma$  orbitals are localised closer to nuclei. This effect is important for a direct observation of 4f electrons, which are localised around their nucleus and shielded by 5p electrons.



# Chapter 2

## Magnetism

In history, applications of magnetism have brought significant progress. Thousands of years ago, magnetic compasses were used for navigation. Electrification, part of the industrial revolution, relied on generators employing magnets; electrical motors, microphones, loudspeakers were introduced, based on electromagnetism. Information technology still relies on magnetic data storage devices, such as hard drives and magnetic tapes. In the latter ones, the bistable magnetisation direction of magnetic domains defines 0 and 1 of a data bit, the smallest unit of information. Continuous reduction of size has increased storage density and writing speed dramatically.

Spins rather than charge states could be employed as bits (or qubits in quantum computers) to process information in future chips. The energy-consuming motion of charge carriers is replaced by flipping spins, with their direction providing 0 and 1 of the bit.

Ferromagnetism, paramagnetism, diamagnetism and antiferromagnetism are the most commonly known manifestations of magnetism. Paramagnetic materials become magnetised in magnetic fields, but do not retain this magnetisation once the field is switched off. Diamagnetism is a comparably weak effect and results in a repulsion of diamagnetic materials in magnetic fields due to induction of magnetic moments. Ferromagnetism is based on collective interactions (and thus long-range order) of magnetic moments of atoms, whose orbitals overlap and couple magnetic moments by exchange interaction. The atomic magnetic moments align parallel, and thereby a spontaneous magnetisation appears in zero magnetic field. Atoms favouring antiparallel alignment of their magnetic moments give antiferromagnets with long-range order, but zero net magnetisation. Antiferromagnets therefore do not align with magnetic fields.

For many applications, the stability of the magnetisation and its direction is mandatory. This can be ensured by magnetic anisotropy and magnetic

remanence, the magnetisation after removal of an external magnetic field.

## 2.1 Superparamagnetism

A less known phenomenon is superparamagnetism. At high temperatures, magnetic moments of superparamagnets align with external magnetic fields as paramagnets do. Below a certain “blocking temperature”  $T_B$  they retain non-zero magnetisation after removal of an external field, thus show magnetic remanence and hysteresis as ferromagnets do. The hysteretic behaviour stems from magnetic anisotropy, manifested in an energy barrier separating states of opposite magnetisation (cf. Figure 2.1). This energy barrier can be overcome by thermal excitation, resulting in a finite blocking temperature. The timescale of spontaneous magnetisation reversal, the Néel relaxation time, follows an Arrhenius-like law:  $\tau = \tau_0 \exp(\frac{U}{k_B T})$ , with  $\tau_0$  being the attempt frequency, and  $U$  the height of the energy barrier.

The behaviour of a superparamagnet is hysteretic, or blocked, below  $T_B$ , and paramagnet-like above  $T_B$ . Still, usage of the term “superparamagnetic” varies; it might be applied to the magnetic behaviour below  $T_B$ , above  $T_B$ , or both. Researchers focusing on miniaturisation of data storage devices call the behaviour of their small ferromagnetic single-domain particles below  $T_B$  “ferromagnetic”, and “superparamagnetic” only above  $T_B$ ; they perceive superparamagnetism as absence of the desired property, ferromagnetism. In stark contrast, several publications state that “SMMs [...] show superparamagnetic behavior below a certain blocking temperature” [35, 36].

The blocking temperature  $T_B$  is the temperature below which a superparamagnet exhibits slow reversal of magnetisation. A high energy barrier slows down the relaxation of magnetisation; still the relaxation remains a statistical process, and a blocking temperature can only be given together with specifying a timescale. When for example defined as the highest temperature for which a hysteresis loop opens, the blocking temperature depends on the sweep rate of the magnetic field [37]. Another definition relies on the phase lag in ac magnetic field measurements [7], which are frequency- and thus again time-dependent.

Experimental timescales span several orders of magnitude, making  $T_B$  differ by tens of Kelvins. Another quantity to characterise the stability of an SMM is the anisotropy barrier height  $U$  calculated from theoretical models or an effective  $U_{\text{eff}}$  derived experimentally using the Arrhenius-like  $\tau \sim \exp(\frac{U}{k_B T})$  dependence. The latter as well as definitions of  $T_B$  are not well defined because, depending on the temperature range, different relaxation mechanisms dominate.

The blocking temperature of  $\text{TbPc}_2$  is reported to be around 10 K [7, 38, 39]. Unfortunately, the variety of experimental techniques and definitions employed makes it difficult to compare blocking temperature variations caused by changing chemical and geometrical environment such as ligands, staggering angle, geometrical deformation, or charge state of molecules among different publications. Still it is safe to assume that a  $\text{TbPc}_2$  molecule does not retain its magnetisation direction for more than a few seconds at 6 Kelvin, the operation temperature of our STM. This is below the typical timescale of STM imaging. With lower temperatures or different experimental schemes, such as IETS for spin excitation spectroscopy or pump-probe schemes, the superparamagnetism of  $\text{TbPc}_2$  might be accessible.

Practical applications include heat-assisted magnetic recording, where a superparamagnetic nanoparticle of a hard drive platter is heated above its blocking temperature to facilitate setting its magnetisation direction, and magnetic resonance imaging, where small metal oxide particles are employed as contrast agents. For data storage, the magnetic information needs to be preserved, a superparamagnet thus shall be employed below its blocking temperature. This temperature decreases (due to miniaturisation) below room temperature for magnetic hard drives in the near future, and is still well below liquid nitrogen temperature for superparamagnetic molecules.

## 2.2 Magnetic molecules

The first magnetic molecules were synthesised by Wickmann *et al.* in 1967 [40, 41]. These molecules are paramagnetic due to their unpaired spins. Common classes of magnetic molecules include organometallic molecules whose magnetism arises from the incorporated metal atom(s), and open-shell molecules (radicals), which are magnetic due to their unpaired electron spin and can be purely organic. These conventional magnetic molecules are paramagnetic but can interact with each other to couple ferromagnetically to larger magnets showing magnetic hysteresis. In contrast, single-molecule magnets, as described in the following section, show hysteresis on a single-molecule level.

### 2.2.1 Single-molecule magnets

Single-molecule magnets (SMM) are superparamagnetic molecules that show slow relaxation of magnetisation on a single molecule level. SMMs exhibit a bistable high-spin ground state, with two high- $|S_z|$  substates of opposite magnetisation separated by a large energy barrier (cf. Figure 2.1). This zero-field splitting yields large uniaxial anisotropy and bistable magnetisa-

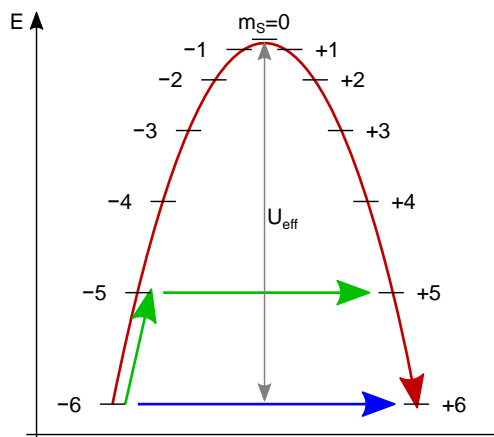


Figure 2.1: **Schematic zero field splitting and relaxation mechanisms of  $S_z$  substates of an SMM. Red arrow: thermal relaxation, blue arrow: quantum tunnelling of magnetisation, green arrows: thermally assisted quantum tunnelling.**

tion. The high-spin ground state is provided by several (usually first row transition) metal ions coupled via superexchange interaction, or by a single (mostly rare-earth) metal ion in a ligand field of molecular complex ligands. The blocking temperatures of SMMs range from a few up to about 14 Kelvin [39, 37]. Timescales of relaxation at low temperature are below a second in many experiments. The magnetisation relaxes by thermal excitations (cf. Figure 2.1), and by tunnelling into opposite  $S_z$  substates. The latter process is called quantum tunnelling of magnetisation (QTM), dominates at very low temperature where thermal excitations have little energy, and is used as a fingerprint in the investigation of SMMs: In 1996 regular steps were observed [42, 43] in the hysteresis curve of  $\text{Mn}_{12}$ -acetate [6, 44], invoked by tunnelling between sublevels which are energetically aligned by Zeeman splitting.

The geometry of an SMM is a result of careful design to establish its magnetic properties, and to suppress quantum tunnelling of magnetisation as far as possible. The molecular ligand periphery mediates access to the magnetic core of the SMM, protects it from its environment (exchange coupling, decoherence), or provide control of the magnetic properties (e.g., read-out [45], write, switch on and off [1]). Modification of the charge state [1] or geometry [46, 47] alter the magnetic properties. The ligands also add functionality, allow for self-assembly of molecules, binding to surfaces, aligning the molecule and thereby the magnetic easy axis.

To increase barrier height and thus achieve longer lifetimes, a large num-

ber of derivatives of  $M_{12}$  and other exchange-coupled clusters has been synthesised and investigated. The quest first concentrated on clusters with larger number of coupled magnetic atoms in order to increase the spin  $S$ , according to the barrier height  $U = -DS^2$ , where  $D$  is the zero-field splitting parameter. However, blocking temperatures did not rise significantly. Later, Neese *et al.* [48] showed theoretically that the prefactor  $D$  scales with  $\sim \frac{1}{S^2}$ , foiling the efforts. A more recent class of SMMs relies on single lanthanide atoms, exhibits larger barrier heights, and is presented in the following section.

### 2.2.2 Lanthanide-based SMMs

The molecule investigated in this thesis is an SMM with a single metal centre (therefore sometimes referred to as “SIMM”, single-ion molecule magnet), a lanthanide ion. Lanthanide atoms have partially filled 4f orbitals, lying close to the nucleus. These orbitals do not form bonds, still they are influenced by ligand fields.

The magnetic moment of a lanthanide-based single-ion single-molecule magnet stems from the 4f orbitals of the lanthanide ion, and its magnetic anisotropy from careful design of its surrounding ligand field. The ligand field is provided by the molecular environment of the lanthanide ion.

The spin-orbit coupling of 4f electrons is large, larger than the crystal field splitting. Spin and orbital angular momenta couple to a total momentum  $J$ . The partially filled f orbitals give a high total momentum  $J$  as derived by Hund’s rules. An appropriate ligand field lifts the degeneracy of the  $J_z$  substates and creates a doubly degenerate high  $\pm m_J$  ground state. This can be understood in a simplified picture: The negative charges of a purely axial ligand field have more overlap with  $J_z$  orbitals of prolate shape than with those of oblate shape. This lifts the energetic degeneracy of  $J_z$  states, and oblate orbitals are lower in energy.<sup>1</sup>

The lanthanide ions hardly interact via exchange coupling as the 4f orbitals are strongly localised around the nucleus (cf. Figure 2.2) and therefore barely overlap with orbitals of neighbouring atoms. This makes their magnetisation both stable against external influence as well as hard to access directly.

The origin of magnetic properties of these lanthanide-based SMMs is closely related to single-ion magnets (e.g., Ho on Pt(111) [9]). Their magnetic

---

<sup>1</sup>Lanthanide-based SMMs investigated so far mostly rely on axial ligand fields. For this simple geometry, Dy and Tb are most suited and therefore most prevalent in research. Equatorial ligand fields favour prolate orbitals and give high  $\pm m_J$  ground states for Er or Yb [8].

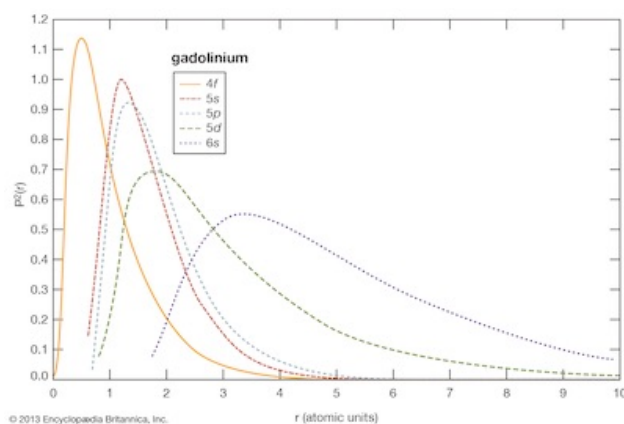


Figure 2.2: **Probability density of 4f electrons**, as a function of the atomic radius. The 4f electrons (yellow curve) are localised close to the nucleus and are therefore shielded by 5s (red) and 5p (blue) electrons, while 5d and 6s orbitals are empty in ionic  $\text{Tb}^{+\text{III}}$ . The graph refers to gadolinium with atomic number  $Z = 64$ , similar to 65 for terbium. Image from britannica.com, <https://www.britannica.com/media/full/491579/187149>.

anisotropy relies on ligand fields as well, provided by neighbouring surface atoms. The magnetism of SMMs consisting of several transition-metal atoms, as discovered [6, 44] long before the first lanthanide-based SMM, arises from a different origin: several transition metal atoms (often Mn [6, 44], Fe [49, 50], Co, or mixtures thereof) are coupled by superexchange mediated by bridging non-magnetic atoms to create a collective high-spin ground state and high anisotropy.

### 2.2.3 $\text{TbPc}_2$

Bis(phthalocyaninato)terbium, abbreviated  $\text{TbPc}_2$ , is the first lanthanide-based single-molecule magnet [7, 51]. Two phthalocyanine (Pc) planes sandwich a terbium ion (see Figure 2.3). The Pc rings are staggered by  $45^\circ$  due to mutual steric repulsion of the isoindole groups. The inner nitrogen atoms are arranged in a square antiprismatic coordination and provide a nearly axial ligand field. The strong spin-orbit coupling of Tb couples the orbital  $L = 3$  moment and the  $S = 3$  spin of the eight 4f electrons to a  $J = 6$  ground state. The axial ligand field favours the oblate  $J_z = \pm 6$  orbitals and induces a high zero field splitting of  $U_{\text{eff}} = 410 \text{ cm}^{-1} = 50 \text{ meV}$  [52], rendering  $\text{TbPc}_2$  an SMM with one of the highest blocking temperatures observed so far [39]. Terbium exhibits an oxidation state of +III, whereas single-decker phthalocyanines in metal-Pcs have oxidation number -II. In

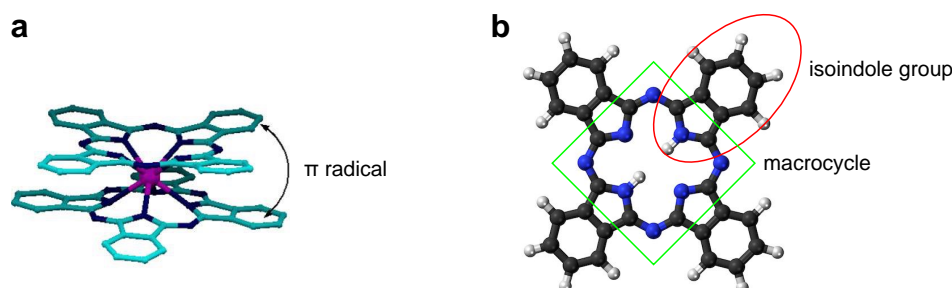


Figure 2.3: **Structure models of double-decker  $\text{TbPc}_2$  and single-decker  $\text{H}_2\text{Pc}$ .** (a) Structure model of  $\text{TbPc}_2$ . Two phthalocyanine rings, staggered by  $45^\circ$ , sandwich a terbium ion (purple). Hydrogen atoms are not drawn for clarity. The unpaired  $\pi$ -radical electron is delocalised over both Pc planes. The two times four inner isindole nitrogen atoms form an antiprism geometry and provide a nearly axial ligand field for the central Tb ion. (b) Structure model of one Pc ring. This drawing shows  $\text{H}_2\text{Pc}$  with two hydrogen atoms instead of a metal ion in the inner cavity. Carbon atoms drawn in black, hydrogen white, nitrogen blue.

neutral  $[\text{TbPc}_2]^0$ , there is thus a hole on the Pc ligands. Ishikawa *et al.* found that this unpaired electron is delocalised over the  $\pi$  systems of both Pc rings, forming a  $\pi$  radical [53, 52]. The unpaired spin forms a second spin system in  $[\text{TbPc}_2]^0$ . Charging  $\text{TbPc}_2$  by an additional electron forms negatively charged  $[\text{TbPc}_2]^-$ ; as the Tb +III oxidation state is very stable, the additional electron fills the singly occupied molecular orbital (SOMO) and forms a filled HOMO.  $[\text{TbPc}_2]^-$  thus does not contain a spin system on the ligands. Ishikawa *et al.* [52] showed that slow relaxation of magnetisation occurs for both neutral  $[\text{TbPc}_2]^0$  and charged  $[\text{TbPc}_2]^-$ , substantiating that  $\text{TbPc}_2$  acts as an SMM both in presence and in absence of the ligand spin. The presence of a ligand spin was found to slow down the magnetisation relaxation [52]. Komeda *et al.* [47] modified the staggering angle of the two Pc planes, resulting in a charge transfer from the surface and quenching of the ligand spin. Stepanow *et al.* [12] found by XMCD that the magnetic properties of individual  $\text{TbPc}_2$  molecules are preserved upon adsorption on a Cu(100) metal substrate. This is an important finding as adsorption on surfaces is known to alter properties of molecules, their geometry, electronic structure, and charge state. Vitali *et al.* [11] claim that the 4f orbitals are accessible to STM, visible in a cross-shape structure on the Pc ligand.

The intramolecular staggering angle of  $45^\circ$  minimises the steric repulsion of the Pc ligands. The angle can still be altered for example by embedding  $\text{TbPc}_2$  into a crystal matrix. Komeda *et al.* [47] showed that a modification

of the staggering angle shifts the frontier orbitals (i.e. HOMO and LUMO), alters the charge state and thus switches the ligand spin on and off. As the magnetic properties of lanthanide-based SMMs rely on the ligand field of the molecular ligands, a distortion of a Pc, or a different arrangement of the two Pc rings with respect to each other, influences its magnetic behaviour. Surface adsorption changes both electronic and geometrical structure, thereby affects the SMM properties, but also provides access to them.

TbPc<sub>2</sub> contains two phthalocyanine ligands, which are prevalent in research and application. For application, their optical properties are widely employed. Apart from simple dyes, phthalocyanines are used in CD-R storage media and even for phototherapy in medicine. Closely related molecules, porphyrins, are central building blocks in haemoglobin in blood, and in chlorophyll in plants. Many elements can be placed into the central cavity, modifying electronic structure, colour, and magnetism of the molecule. Similarly, terbium in TbPc<sub>2</sub> can be replaced by many other metal centres, including most lanthanides and Yttrium, which does not contain 4f electrons. The ligands can be modified as well, e.g., attaching functional groups to the Pc rings can be used to modify coupling to the substrate, or control self-assembly on surfaces to construct larger systems. Being known for a long time, chemistry provides a large toolbox for modification of these molecules with industry-scale synthesis. Phthalocyanines are heterocyclic macrocycle organic compounds with a conjugated  $\pi$  system. Metallated phthalocyanines are highly symmetric with a 4-fold D<sub>4h</sub> symmetry. HOMO and LUMO (highest occupied and lowest unoccupied molecular orbitals) also exhibit this high symmetry; they are well accessible to STM, as their  $\pi$ -type orbitals decay far into the vacuum. Phthalocyanines are also excellent candidates for STM studies because they are flat, stable, and can be sublimed without decomposition. In view of these findings, TbPc<sub>2</sub> is a very promising candidate to study SMM properties by SP-STM.

**Part II**  
**Instrumentation**



# Chapter 3

## Building a 300mK-17T-STM system

### 3.1 Motivation

SP-STM experiments on magnetic molecules profit from advances of the experimental setup. The first concern is the temperature of the STM. Many single-molecule magnets show blocking temperatures of only a few Kelvin. To study single-molecule magnetisation, similar to (SP-)STM magnetometry investigations of single atoms [9, 10] and nanoparticles [54, 55], low temperatures are needed to lower the thermal energy of the system and slow down spontaneous reversal of magnetisation. Lower temperatures also increase the energy resolution of the STM. The energy resolution scales linearly with temperature ( $\Delta E = 5.4k_{\text{B}}T$  [56, 57]), as long as mechanical and electronic noise is sufficiently low. Many STMs are cooled by liquid helium and reach  $T \sim 4$  K and  $\Delta E \sim 2$  mV, which is sufficient for investigation of the local density of states (LDOS) of a system, or, e.g., Kondo effect and vibrational [57] and vibronic excitations. Yet higher energy resolution and thus lower temperatures open perspectives of investigating spin-flip excitations by inelastic electron tunnelling spectroscopy (IETS). At  $T = 300$  mK the energy resolution is  $\sim 0.15$  meV. Such a low temperature cannot be reached with simple baths of cryoliquids, but requires a more complex design; therefore, the number of STM systems operating at 300 mK is still limited. For SP-STM, a magnetic field is very helpful to unambiguously prove that an effect observed is in fact due to magnetism, and mandatory for magnetometry measurements or investigations of coercivity. To investigate a Zeeman splitting of states due to an external magnetic field, both a high energy resolution and a high magnetic field are required.

The system presented here reaches  $T = 380$  mK and  $B = 17$  T. This combination of both low temperature and very high magnetic field is extremely rare with so far only one system [58] in the world offering a comparable field (15 T) at yet lower temperature (10 to 15 mK). The system was designed with a focus on the preparation and investigation of molecular systems. To achieve the high energy resolution as expected by low temperature operation, mechanical and electronic noise need to be minimised. The system offers the possibility of *in situ* tip exchange and preparation, a prerequisite for SP-STM. It offers several facilities to clean crystal surfaces with different techniques and prepare ultra-thin films, especially magnetic films for SP-STM, on an atomically clean level in a UHV environment. The system provides automated sample cleaning in order to save time. A special focus lies on the preparation of molecules, offering low-temperature deposition to allow for investigations of single molecules, and preparation of molecules from the gas phase or liquids.

This chapter describes the 300mK-17T-STM system assembled in this work. The first section 3.2 introduces the working principle of the cryostat, its implementation, and discusses problems of this implementation. The concept of the entire system is given in section 3.3. Section 3.4 describes the preparation chamber, focussing on elements for preparation of molecular systems and presenting improvements compared to the design of a previous molecule-adapted VT-STM of the group. The last sections (3.7 and 3.8) describe the STM chamber and the microscope.

### Comparison to other sub-Kelvin STM systems

Even with 300mK-type cryostats available for several years, the combination of 300mK temperature, STM (or other scanning probe techniques), and high magnetic field is still rare, as STM poses special requirements for the cryostat design concerning vibrational noise and UHV compatibility. The implementation of a high magnetic field further reduces the choice of materials (compare section 3.3.2). Apart from the “single-shot” design used here, other techniques to reach sub-Kelvin temperatures include Joule-Thomson systems and  $^3\text{He}/^4\text{He}$  dilution refrigerators. Both techniques introduce vibrational noise to the STM, stemming from gas flow through expansion tubes and continuous pumping of a 1 Kelvin  $^4\text{He}$  bath, respectively. Despite this intrinsic disadvantage, both techniques are successfully employed for STM [59, 58]. A  $^3\text{He}/^4\text{He}$  dilution refrigerator at NIST operates at 10 to 15 mK and 15 T [58].

A few single-shot 300mK system reach both comparable temperature and magnetic fields as the one described here. A system designed by Oxford Instruments [60] operates at 315 mK and 14 T, and Unisoko sells STMs specified

with 400 mK and 10 T. A drawback of the single-shot mode is the need to re-liquefy  $^3\text{He}$ , which means interruption of measurements, and a temporary increase of temperature.

Low temperatures and high magnetic fields are not the only paths to bring STM and SP-STM forward: some systems include magnetic fields pointing in arbitrary 3D directions [61] for the investigation of complex magnetic states, others are designed to operate with extremely low currents, allowing for investigations of very weakly bound and therefore mobile molecular systems, and yet others improve on high-frequency signalling to explore time regimes inaccessible so far [62]. Additionally, not only the abilities of the STM, but also the appropriate preparation of samples is important. A number of highly interesting molecules have been deposited intact and clean onto surfaces. Soft landing techniques and electrospray deposition techniques led to advances here.

## 3.2 Working principle and design concept

This section first explains the working principle of single-shot 300mK cryostats and then describes the implementation in the system assembled here.

Cryogenic temperatures can be achieved by bringing the system into or in close contact to a cryoliquid, e.g., liquid nitrogen ( $T = 77\text{ K}$ ) or liquid helium ( $^4\text{He}$ ,  $T = 4.2\text{ K}$ ). Temperatures of about 1 K can be achieved by pumping the gas over the liquid helium bath, exploiting the effect of evaporative cooling. To reach millikelvin temperatures,  $^4\text{He}$  is replaced by its isotope,  $^3\text{He}$ . The cooling method applied here relies on evaporative cooling of  $^3\text{He}$  and allows for temperatures of about 300 mK. As  $^3\text{He}$  is considerably more expensive than  $^4\text{He}$ ,  $^3\text{He}$  is not liquefied in an external lossy process, but kept and liquefied within the cryostat system. With the boiling point of  $^3\text{He}$  being 3.2 K, cooled  $^4\text{He}$  can be employed to liquefy  $^3\text{He}$ . While bath cryostat systems run continuously, with only little disturbance during the refill of the cryoliquid, these 300mK systems need to run in cycles (“single-shot” mode) of operation at 300 mK with liquid  $^3\text{He}$  evaporating until it has run out and subsequent re-liquefaction. The period of the cycle depends on the amount of  $^3\text{He}$  and on the design of the cryostat. The holding time is typically chosen to be one or a few days in order to perform experiments without the need to warm up to liquefaction temperature during experiments.<sup>1</sup>The system presented here

---

<sup>1</sup>If the prepared sample is not destroyed by the increased mobility of the adsorbates at elevated temperature or by contamination from background gas desorbed by motion or temperature changes of components, the investigation can still last several cycles without fresh preparation of the sample.

is designed for a holding time of 100 hours and has proven to operate for 160 hours.

The single-shot mode cycle of operation and liquefaction works as follows: During operation at  $\sim 300$  mK,  $^3\text{He}$  is liquid and is contained in a reservoir. For evaporative cooling, its gas phase is pumped. This can be done by a sorption pump adsorbing  $^3\text{He}$  when cooled by contact to a liquid  $^4\text{He}$  tank. When the liquid  $^3\text{He}$  is used up, it needs to be re-condensed. For this, the  $^3\text{He}$  reservoir is brought into contact with a  $^4\text{He}$  “1K system” ( $T \sim 1$  K) cooled below the boiling point of  $^3\text{He}$  by pumping the  $^4\text{He}$  contained. To release  $^3\text{He}$  from the sorption pump, the pump is warmed up to about 40 K. When all  $^3\text{He}$  has condensed, the connection of the  $^3\text{He}$  reservoir to the 1K system is removed and the sorption cooled down again to cool the  $^3\text{He}$  by pumping.

This principle is implemented into the system described here, with emphasis on vibrational decoupling to reduce noise in the STM, which is directly attached to the  $^3\text{He}$  tank (“pot”). The sorption pump works without mobile parts and is therefore silent. The 1K system ( $T \sim 1.5$  K) is connected to an external pump, which can introduce vibrations. Therefore, not only the thermal but also the mechanical contact to the 1K tank is opened for operation. STM,  $^3\text{He}$  pot, and sorption pump are mounted on an insert (Figure 3.1), which can be moved vertically (Figure 3.2) to establish the contacts to the  $^4\text{He}$  bath and the 1K system needed for operation and liquefaction, respectively. All  $^3\text{He}$  is always contained in the insert. The insert rests on damping legs for vibrational decoupling from the boiling cryoliquids, the rest of the setup, and external pumps. Contacts to the 1K system and the  $^4\text{He}$  bath are established by cones on both insert and tanks, which are pressed into each other by vertical motion of the insert. Sorption pump and  $^4\text{He}$  bath need to be thermally connected during operation (to cool the sorption pump below  $\sim 20$  K to adsorb  $^3\text{He}$ ), so the  $^4\text{He}$  outer cone needs to be vibrationally decoupled from the  $^4\text{He}$  bath itself. It is therefore mounted on the damping of the insert, and copper braids provide thermal connection to the  $^4\text{He}$  bath. In condensing position (Figure 3.2b) the sorption pump is free, so it is not cooled. To accelerate desorption of  $^3\text{He}$ , resistive heaters heat the pump.

To change between these positions, the inner cone of the  $^3\text{He}$  pot has to pass the outer cones. For this purpose, this inner cone and both outer cones are not arranged as full cones, but have clearances giving a propeller shape (Figure 3.2d). A  $60^\circ$  turn of the insert lets the cones pass.

Apart from these two positions used for measurement operation and condensation, there is a third position to grant access to the microscope. In this higher “transfer position” (Figure 3.2c) the microscope is located just above the magnet, so it is free to access by a wobble stick, and samples can be inserted. In this position, atoms or molecules can be deposited onto the

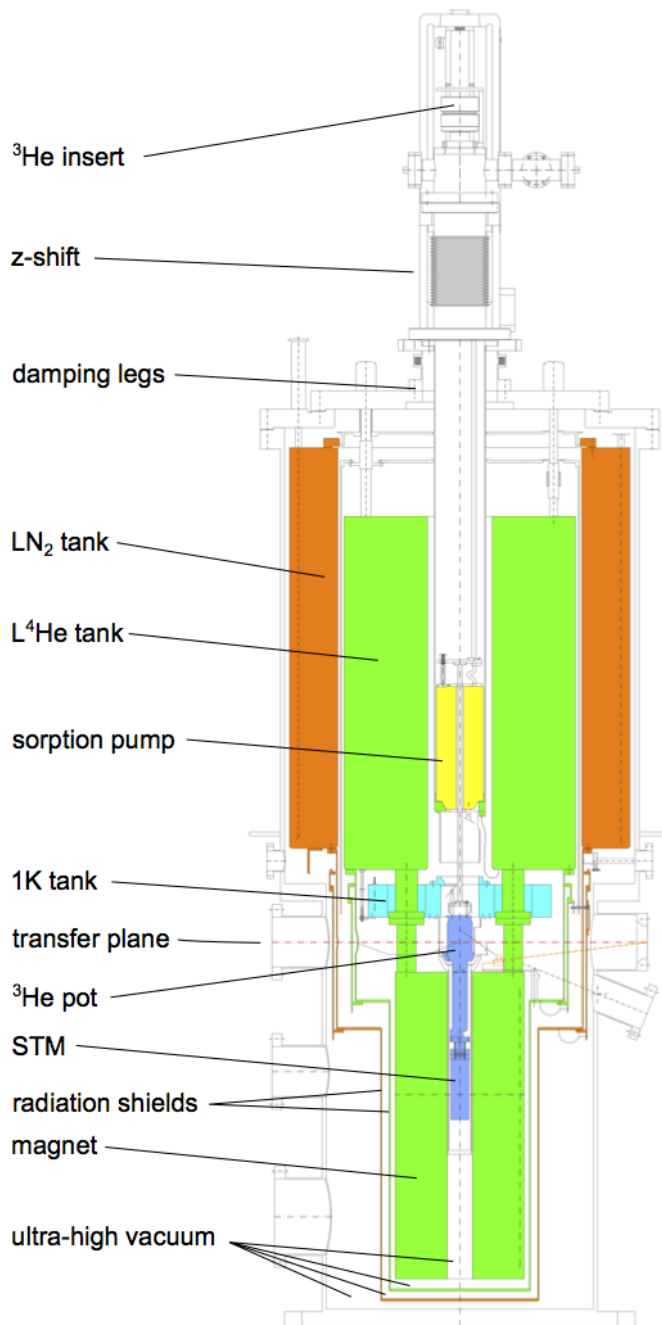


Figure 3.1: **Cross-sectional view of STM chamber with cryostat.** The STM chamber contains the cryostat with several tanks for cryoliquids and the magnet, embedded in ultra-high vacuum. The central insert with the STM contains the  $^3\text{He}$ . It can be moved vertically to change between operation and liquefaction mode, and rests on damping legs for vibrational decoupling of the STM. Cylindrical liquid helium and liquid nitrogen tanks with shields enclose the insert like onion shells to reduce radiative heat input. Liquid helium is also used to cool the  $\text{Nb}_3\text{Sn}$  magnet to superconducting temperatures. In the 1K tank,  $^4\text{He}$  is cooled by pumping with an external pump. Engineering drawing by Cryovac.

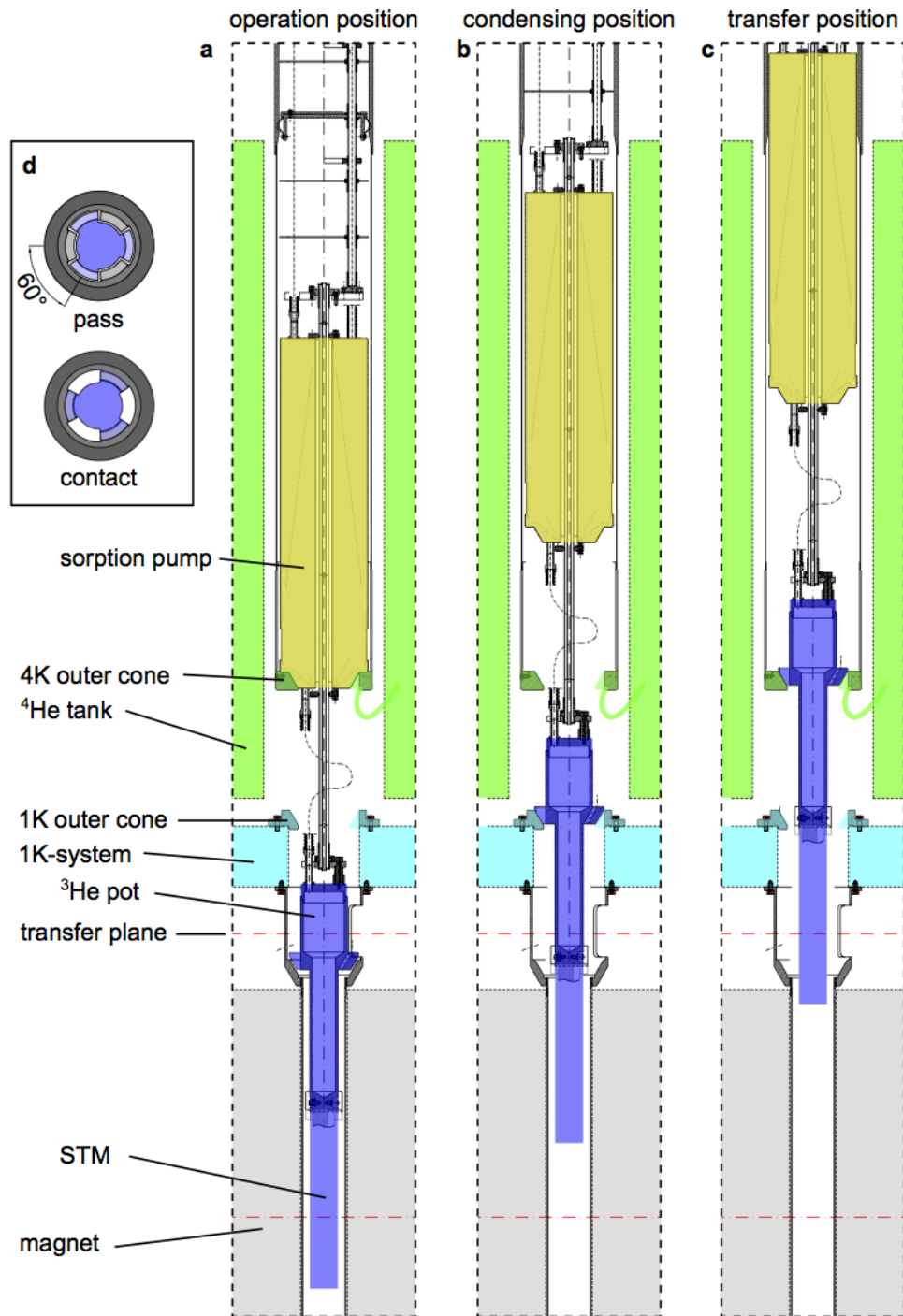


Figure 3.2: **Cross-sectional view of  $^3\text{He}$  insert positions.** The  $^3\text{He}$  insert is moved vertically to bring different cones into contact, providing thermal connections for operation or liquefaction mode. (a) operation position. The sorption pump (inner) cone is pressed into the 4K outer cone, which is thermally connected to –but vibrationally decoupled from– the  $^4\text{He}$  bath. The  $^3\text{He}$  pot and STM hang free. The cooled sorption pump adsorbs the  $^3\text{He}$  evaporating from the liquid  $^3\text{He}$  in the  $^3\text{He}$  pot. (b) condensing position. The sorption pump hangs free and is heated; the  $^3\text{He}$  gas desorbed from it condenses in the  $^3\text{He}$  pot, whose cone is pressed into the 1K outer cone for cooling. (c) transfer position. The  $^3\text{He}$  pot inner cone is pressed into the 4K outer cone to position the STM in the transfer plane, where the sample can be accessed. (d) top view of inner  $^3\text{He}$  pot cone (blue) and outer 1K cone (grey). A rotation of the insert by  $60^\circ$  displaces them to contact or pass. Engineering drawing by Cryovac.

cold sample surface, allowing for a preparation of isolated single atoms or molecules as the low temperature reduces mobility. For deposition of single atoms, the STM temperature should not exceed  $\sim 10$  K [63, 64, 30]. To achieve this, the microscope is cooled by pressing the  $^3\text{He}$  pot inner cone into the 4K outer cone. With radiation shields closed, the temperature of the microscope does not exceed 8 Kelvin. During sample transfer, the wobble stick applies forces to the microscope. These should not act laterally onto the fragile insert. To ensure that, as the  $^3\text{He}$  pot is fixed with the 4K cone and the microscope rigidly connected to the  $^3\text{He}$  pot, forces applied by the wobble stick act directly on the damping system of the insert.

### Condensing time

The condensing time (i.e. the period required to liquefy all  $^3\text{He}$ ) of two days is extremely high, as compared to just half an hour in a comparable system designed by Oxford Instruments [60], which still operates for about a day following liquefaction. Other parameters such as base temperature and consumption of liquid  $^4\text{He}$  and  $\text{LN}_2$  are somewhat comparable. This long condensing time is a tremendous concern as it gives rise to significant waiting time before starting the actual experiment after sample preparation, and the condensing time as compared to the holding time of about six days reduces the effective measurement time by 25%. Reasons for this long condensation time are the following: The (sufficiently large) 1K system needs an efficient thermal connection to the  $^3\text{He}$  pot to condense  $^3\text{He}$ . In contrast to other designs [60] the 1K system is not located in the damped insert to avoid vibrations from the 1K pump. The contact is done by pressing cones into each other, so the force is applied by, and through, the insert. On the one hand, the insert has to be strong to apply a high force, on the other hand, it needs to be thin to reduce the heat input from top, which is at room temperature. These interests compete and limit the pressing force and thereby the heat transfer to the 1K system. Secondly, the amount of  $^3\text{He}$  used is 100l (gas), as opposed to only a few litres for comparable systems. With a holding time of the same order this means that more  $^3\text{He}$  is needed for cooling, i.e. the heat input on the 300 mK parts is obviously higher than in other systems.

### Cryostat installation

During the installation and tests of the cryostat in our lab, several problems occurred. Some of them could be solved by us, others required the cryostat to be sent back to the manufacturer several times. A short overview is given to illustrate the kind of caveats occurring with newly developed designs and

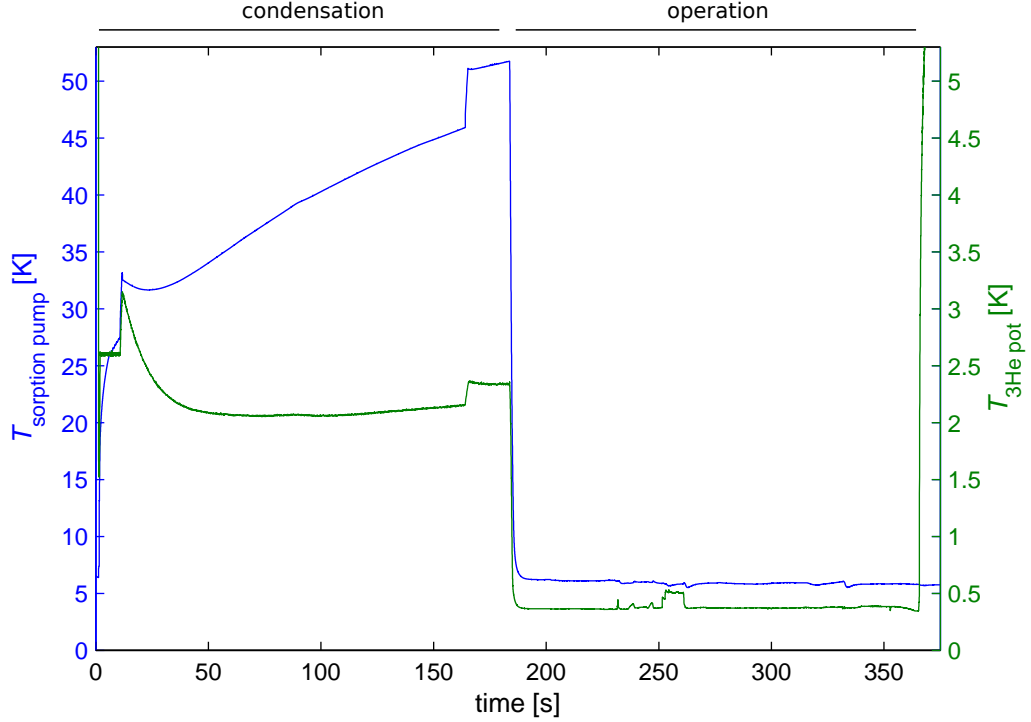


Figure 3.3: **Test of condensation and operation time as well as temperatures.** Initially, the insert is in transfer position. Both sorption pump (blue) and  $^3\text{He}$  pot (green) have a temperature of around  $T \sim 6$  Kelvin. Then, the insert is driven to condensing position. A resistive heater heats the sorption pump. Different control mechanisms are tested and cause jumps and plateaus. After 184 hours, condensation is considered to be complete, and the insert is driven to operation position. This cools the sorption pump. The plateau at  $t \sim 255$  h is caused by a heat load test. The dips in the sorption pump temperature at  $t \sim 260$  h and  $t \sim 340$  h stem from refills of liquid  $^4\text{He}$ . These lower the sorption pump temperature as all of its cooling connection becomes covered by liquid  $^4\text{He}$ , but leaves the  $^3\text{He}$  pot and thereby the STM temperature unchanged, avoiding thermal drift in the STM. Over time, the  $^3\text{He}$  pot temperature increases slowly from  $\sim 360$  mK to  $\sim 380$  mK, and never exceeds 385 mK. After 180 hours of operation, all liquid  $^3\text{He}$  is used up, and the  $^3\text{He}$  pot warms up slowly.

present the solutions.

After the first tests in our lab, the cryostat had to be sent back to the manufacturer because of three problems, each of them preventing use of the system:

- When applying a magnetic field, magnetised stainless steel employed in lower parts of the insert made it incline and touch non-damped components, circumventing the damping system, and thereby preventing STM use.
- The sorption pump could get stuck in a too high position, not reaching the 4K cone any more, thus rendering it unable to reliably pump  $^3\text{He}$ .
- The system reached only 650 mK, and liquid  $^3\text{He}$  ran out within a few hours, both indicating a too high thermal load.

Other, minor problems included:

- A bellow containing the  $^3\text{He}$  gas touched the (sharp-edged!) z-shift vacuum bellow from inside when moving the latter. A damage of the vacuum bellow would result in a sudden vacuum leak in the cryochamber. A leak of the  $^3\text{He}$  high-pressure bellow would result in loss of expensive  $^3\text{He}$ . The bellow is needed to connect the  $^3\text{He}$  reservoir fixed with the non-rotating part of the insert to the rotating part. The bellow forms a loop which widens and contracts with the rotation of the insert. In the widened position, the diameter of the loop was too large, touching the z-shift bellow. A quick calculation revealed that the gain of diameter given from a  $60^\circ$  rotation and an ideal minimum inner diameter defined by the pillars of the insert left an insufficient one millimetre distance to the z-shift bellow. A protecting shield sent by the manufacturer therefore also did not fit. We solved the problem with a rotation of the fixed part by  $15^\circ$  (one screw hole of the CF200 flange) to further contract the  $^3\text{He}$  bellow, and by wires confining the bellow to define an equal widening.
- The rotary feedthrough moving the radiation shutters failed twice. First its internal bellow had a vacuum leak, then another – by far too thin-walled – bellow translating the torque to move the shutters cracked. The manufacturer replaced it by a solid PTFE cylinder. Still, such a problem causes about a week of delay as the cryostat needs to be warmed up for access.
- We tightened screws of a  $^4\text{He}$  radiation shield with insufficient force. As a result, the shield had small protrusions of up to 1 mm, which made it

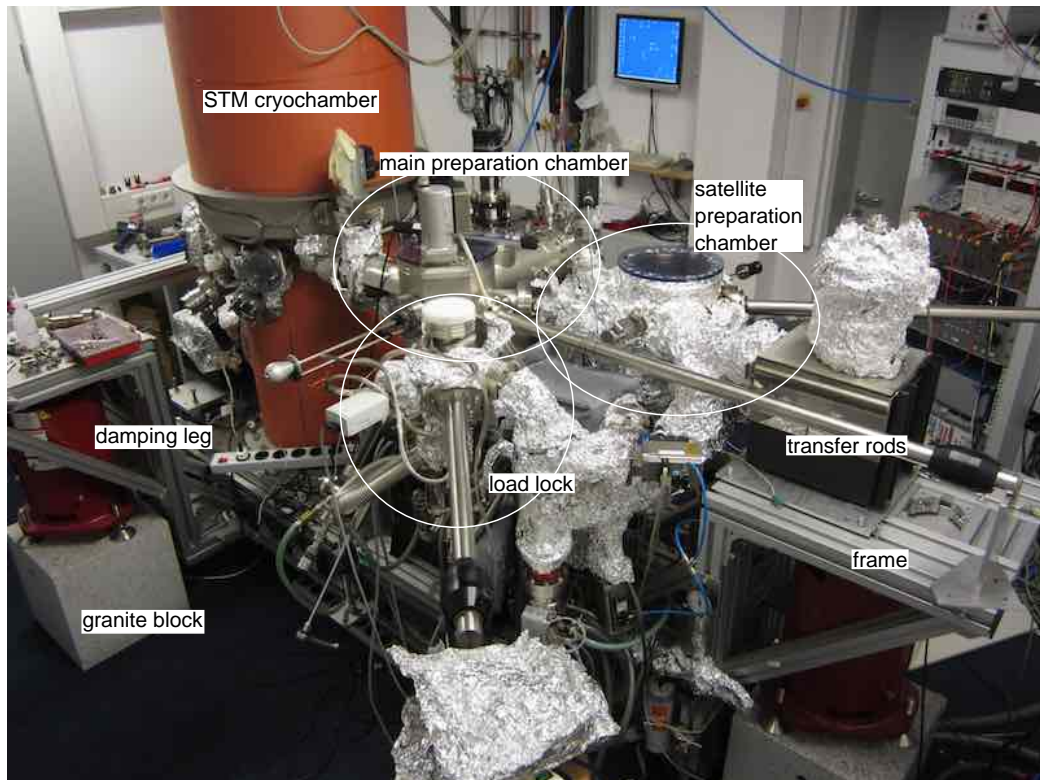


Figure 3.4: **300mK-17T-STM setup.** The system rests on a frame supported by three damping legs (2 visible). STM chamber with cryostat, satellite preparation chamber and load lock are arranged around the central main preparation chamber.

inevitably get stuck when trying to disassemble the cryostat, without a chance to access those screws through the  $\sim 1$  mm slit. Luckily, horizontal access to the screws was possible through the outer LN<sub>2</sub> system after partial disassembly.

- An adaptor between two thin tubes connecting sorption pump and <sup>3</sup>He pot in the insert bent. The tubes were replaced by a single one. (Update: This turned out to be the crucial weak spot of the system. Ultimately, no solution providing both low thermal conductance and sufficiently high mechanical stability was found.)

### 3.3 Vacuum chambers overview

This section explains the functional structure of the system being separated into several chambers with different purpose.

The system is divided into separate chambers to separate functionality and allow for separate maintenance. Most important is the separation into measurement (STM) and preparation chamber. Since the measurements should not be disturbed by contaminations and the STM chamber cannot be modified quickly due to the long warm up and cool down procedures of the cryostat, most preparation facilities are located in the preparation part of the system. The main preparation chamber houses facilities for sample cleaning, deposition of metal films and molecules, provides storage space for samples and mobile evaporators, and offers a LEED/Auger system for analysis. A satellite preparation chamber provides facilities for cleaning crystals at very high temperatures, and does not contain any molecule facilities to maintain a very high level of cleanliness. All chambers offer ultra-high vacuum conditions (see section 3.3.1). To introduce or exchange crystals, mobile evaporators, or other parts, a small separate load-lock chamber is used.

#### 3.3.1 Vacuum

To allow for experiments on molecules in an atomically well-defined environment, contamination of the sample needs to be prohibited during both sample preparation and measurement. Therefore, all vacuum chambers provide ultra-high vacuum (UHV) of less than  $2 \cdot 10^{-10}$  mbar. To maintain UHV, materials used inside the chambers are well chosen (compare section 3.3.2 for the even more demanding conditions for the microscope), UHV capable pumps are used, and the system is baked out after each opening to remove adsorbates from the chamber walls.

#### Pumps

While STM and preparation chamber have separate turbomolecular and ion getter pumps, the load lock turbo pump is shared between the load lock and the satellite preparation chamber, and also serves the purpose of differential pumping of the sputter gun in the preparation chamber.

### 3.3.2 Materials

The choice of materials used in the system is limited by several requirements: UHV, low temperatures and high magnetic fields. UHV compatibility requires the vapour pressure of a material to be low. The strong magnetic field and stray field of the magnet requires materials in its vicinity to be non-magnetic, as magnetisable materials in the magnetic field apply a force onto the magnet. For the  $^3\text{He}$  insert, the choice of materials is further reduced as some materials (e.g., Al, Ti, or Mo) become superconductive already above 300 mK. As they expel magnetic fields due to the Meissner effect, they also apply a force onto the magnet when placed in the inhomogeneous part of the field (cf. levitation effect).

UHV compatibility is a common constraint for vacuum technology. Many metals can be used (except for, e.g., zinc and lead), a number of insulating materials is available too ( $\text{Al}_2\text{O}_3$ , macor), some of which have a finite but sufficiently low vapour pressure (PTFE, kapton). Many useful materials exhibit a too high vapour pressure: organic materials like wood, fluids like oil and other lubricants. A vast number of suppliers of UHV-compatible products (e.g., glues, ball bearings, and button heaters) helps to realise designs.

A less common constraint is the need to avoid magnetic materials. They give two problems when used in the field of the magnet. Firstly, magnetisable materials in the (inhomogeneous part of the) magnetic field apply a force onto the magnet. The maximum allowed force is limited as the magnet mounting is kept weak in order to reduce thermal input. Secondly, if magnetic materials are used in the  $^3\text{He}$  insert, the force applied onto it by the magnetic field might push the insert against a wall. This connection of insert and its surrounding bypasses the damping system of the insert and renders it useless. Vibrations from the machine are then introduced to the STM. Even without mechanical contact, the force applied by the magnet onto the insert couples these components and can introduce vibrations from the undamped magnet to the insert and the STM. Originally, the ceiling of the  $^3\text{He}$  pot was made from weakly magnetic stainless steel. The manufacturer had to replace this by the titanium alloy “titanium grade IX” as the insert touched the wall with the weakly magnetic material employed. Pure titanium is avoided for the  $^3\text{He}$  pot, as it is superconductive at the base temperature of 300 mK ( $T_{sc} = 0.40\text{ K}$ ). In the microscope, superconducting materials can be used as the field is homogeneous. Still the amount of superconducting material employed is kept low, and no weakly magnetic material is used. Titanium and molybdenum are used in the microscope, as replacements are hard to get: titanium replaces stainless steel for screws and nuts, molybdenum replaces the weakly magnetic Inconel steel for the front spring (which is parallel to

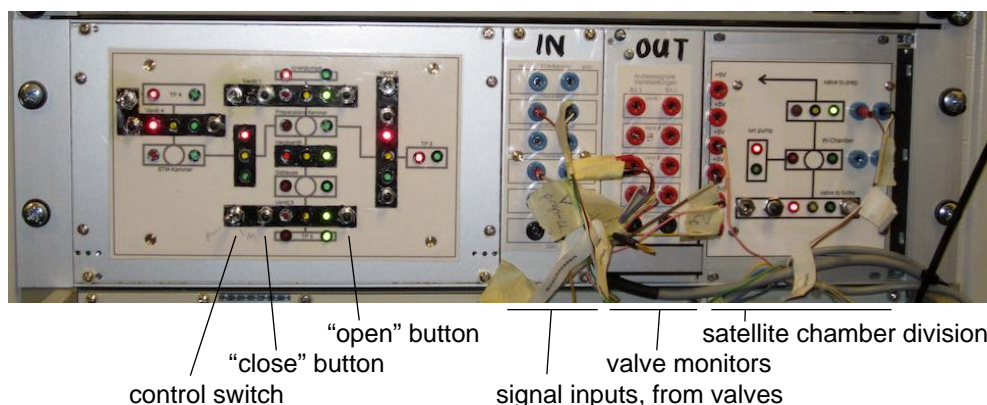


Figure 3.5: **Pump monitoring and valve control unit** Left section: top view layout of the system (without satellite chamber). Red and green LEDs with hollow circle in between represent chambers and monitor their pressure; traffic light LEDs on black background represent valves, indicating the valve position (red: closed. green: open. yellow: half open. no light: error) and provide manual control; red and green LEDs without circle in between represent pumps and monitor their status. Section “IN”: signal inputs from manually driven valves. Section “OUT”: pneumatic valve status output (+5 Volt). Right section: later addition for satellite chamber, functionality identical to left panel.

the magnetic field lines).

### 3.3.3 Pump monitoring and valve control

The pump monitoring and valve control unit provides manual as well as computer control over the valves of the vacuum system, and preserves the UHV in case of power failure, accidental leakage or pump failure. It also provides a fast overview of the vacuum functionality of the system, in order to simplify usage and avoid user mistakes. The unit is mounted in the rack, with most cables connected in the rear for free access of front panel elements. For fast overview, the panel layout maps a top view of the vacuum system.

The unit conserves the UHV in case of power failure in absence of experimenters. In case of power failure of the uninterruptible “UV”-line powering pumps and this unit, all pneumatic valves close automatically, driven by compressed air. This disconnects the UHV from all fore-vacuum lines. When the power returns, the unit does not re-open the valves until a user manually opens them. This ensures the UHV remains untouched. In case of pump failure or leakage the valves are automatically closed as soon as the associ-

ated pump controller reports malfunction, such as a turbomolecular pump decelerating below two thirds of full rotating speed.

The unit is connected to a computer via an A/D interface to provide the functionality of the manual front panel to a PC running Labview. This is used by the Labview program controlling automated sample cleaning (section 3.9.2).

## 3.4 Preparation chamber

This section describes the main preparation chamber and introduces its main features. The preparation chamber provides facilities for all preparation steps, i.e. sample cleaning, metal film and molecule deposition.

Most devices of the chamber are arranged to point to a central spot in the chamber where the sample can be positioned. With the sample kept in this position, several preparation steps can be performed without the need for manually moving the sample, opening the possibility of automating these steps. In this position, the sample sits in the transfer rod and is accessible by the wobble stick, it can be sputtered, heated, and coated with metal films or molecules without the need to change position. Both transfer rods mounted on preparation chamber and load lock pass this spot for access by the wobble stick. Two electron beam metal evaporators are mounted in a 45° angle from the bottom. Metal deposition is started and stopped by shutters. The mobile evaporator stage, described in more detail below (section 3.4.3), is mounted in the front to provide easy access. The sputter gun is mounted in the lower right to keep it close to the load lock turbo pump, which is needed for differential pumping. Below the transfer plane, all around the chamber, a carousel offers 20 storage places for all kinds of samples. For access, it is turned until the sample receptor is behind the cut-out in the cooling shield in the central position. A LEED/Auger system (section 3.5) is installed on a vertical CF200 flange in the rear of the chamber.

### 3.4.1 Transfer stage

The transfer stage is mounted on the preparation chamber transfer rod and serves two purposes: the transfer of sample and mobile evaporators between preparation and STM chamber, and the preparation of samples in the central position of the preparation chamber. While the former is surprisingly not trivial and described in section 3.10, the latter is described in this section.

The transfer stage (Figure 3.7) provides three sample receptors to load and transfer samples, mobile evaporators, tip shuttles and others. The heater

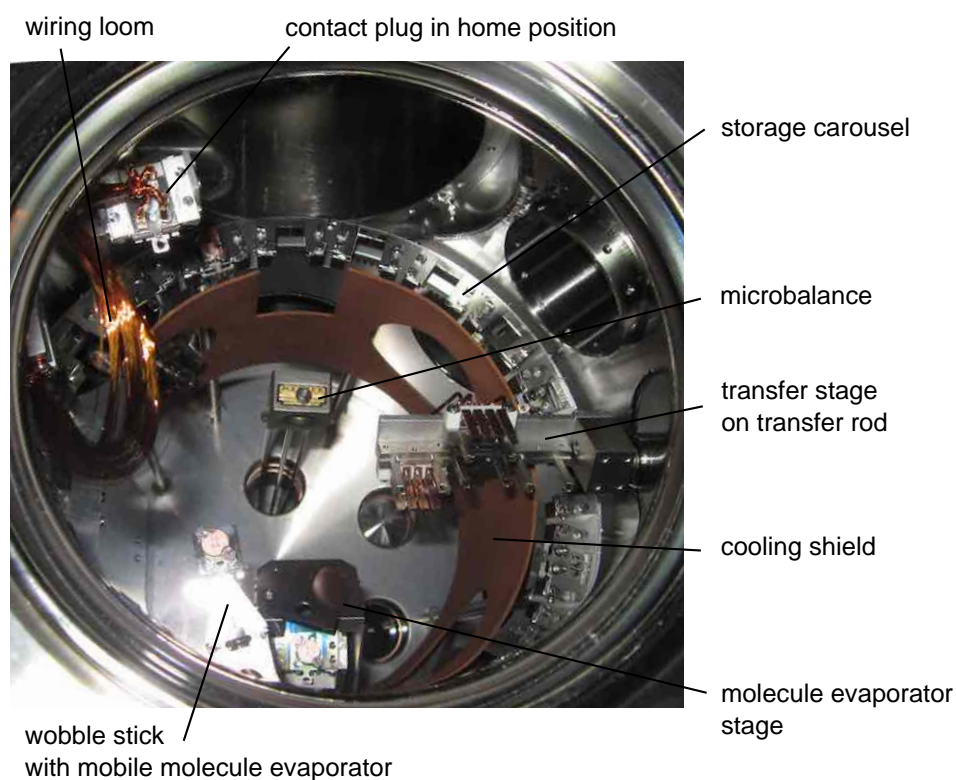


Figure 3.6: **Top view into main preparation chamber, from experimentalist's perspective.** The wobble stick (front, bottom of the image) accesses all sample receptors. Molecule evaporator stage (front) and transfer rod (right) move axially to grant access by the wobble stick in the centre of the chamber. The wiring loom (left) provides electrical contact from a vacuum feedthrough when plugged into the transfer stage on the transfer rod. The microbalance can be raised into the axis of the molecule evaporator to determine the rate of sublimed molecules. Samples and molecule evaporators are stored in the storage carousel, protected from transfer stage radiation heat by a cooling shield.

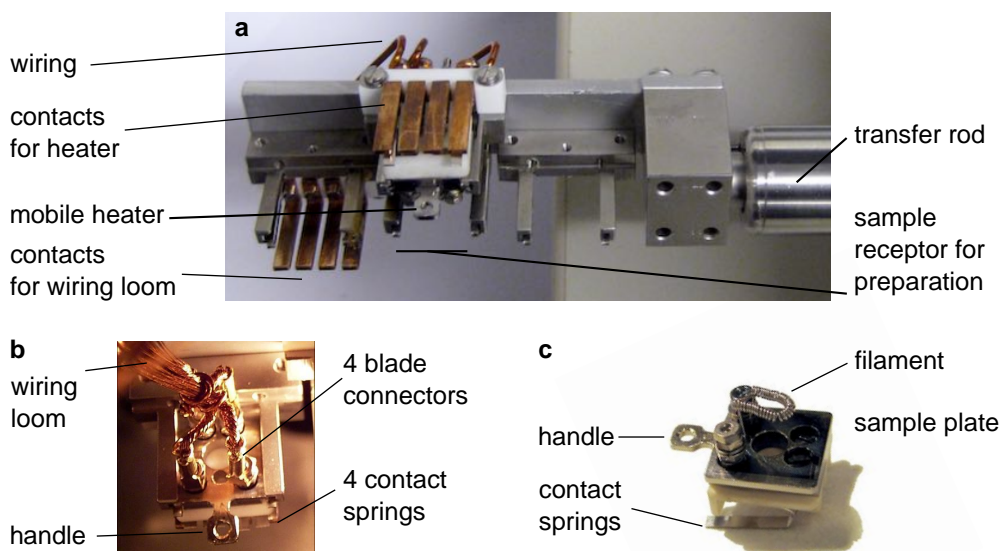


Figure 3.7: **Transfer stage.** (a) transfer stage mounted on transfer rod, with the central sample receptor exposed to the filament of the mobile heater. (b) contact pad with wiring loom in the left position of the transfer rod. (c) mobile heater with U-shaped filament, as mounted in the top centre sample receptor in (a).

filament is a home-built coil of 0.2 mm diameter tungsten wire. It is U-shaped parallel to the sample plane to provide equal heating of the crystal surface plane and also to closely surround a tip mounted in a tip shuttle. The filament is mounted on a mobile sample plate following the mobile molecule evaporator design. It can thus easily be replaced without opening the chamber. For electrical contact of the heater the contacts of the upper receptor are connected to the lower left connector, which is designed to house a contact plug with a wiring loom connected to a vacuum feedthrough. In contrast to a previous design, the ends of the wire bundles are clamped in blade connectors for reliable separation. One of the wiring loom contacts connects the sample in the lower middle receptor to measure the sputter current and to set it to a high voltage potential. The latter functionality is needed to flash tips (compare section 3.8.2) by electron beam bombardment. As the U-shaped filament surrounds the tip apex, it is heated very locally, and temperatures of  $T = 2000^{\circ}\text{C}$  can be reached while the stainless steel parts of the transfer rod stay sufficiently cool. Flashing or even annealing crystals in the transfer stage is however not possible as an entire crystal requires a much higher heating power, heating stainless steel sample receptor and Inconel spring beyond their specification.

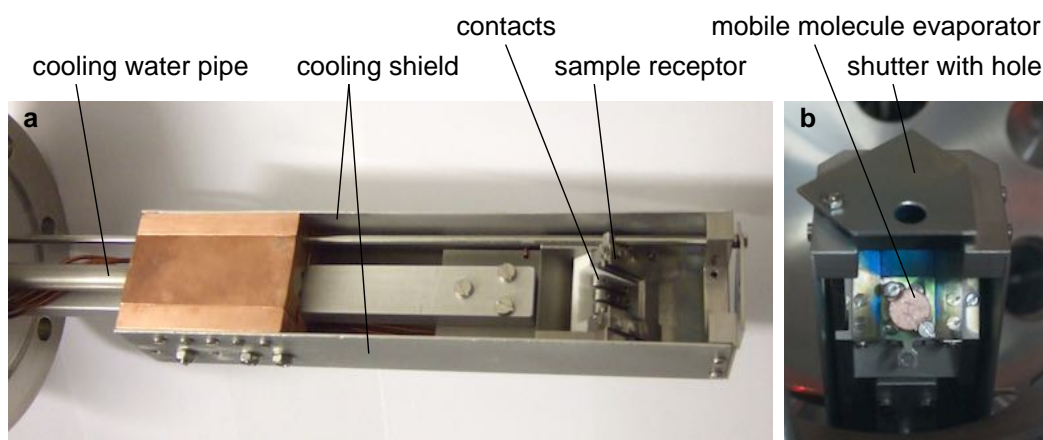


Figure 3.8: **Mobile evaporator stage.** (a) Full view of the stage, with empty sample receptor. (b) Top view of the upper part of the stage with mobile molecule evaporator and opened shutter.

### 3.4.2 Microbalance

The microbalance is used to determine the flux of the mobile molecule evaporators. The oscillating quartz becomes heavier by molecule deposition, therefore its resonance frequency decreases. This frequency decrease is recorded. As the commercial microbalance is designed to be sensitive for metal film coating of several nanometre thickness, it is just sensitive enough for our purpose of submonolayer molecule deposition, with noise on the frequency signal of the same order as a typical deposition rate. The frequency is therefore recorded and averaged (by a Labview program, section 3.9.1) over about 20 seconds to receive a reasonable rate value.

### 3.4.3 Stage for mobile evaporators

The mobile evaporator stage provides electrical connection for mobile evaporators. It has a four-contacts design to load different kinds of mobile evaporators and points towards the central spot of the chamber. It is mounted on an axial z shift, so the distance between evaporator and sample can be modified to control the deposition rate without changing the evaporation temperature.

The evaporator is surrounded by a water cooled shield<sup>2</sup> and a shutter in

<sup>2</sup>In contrast to the original design, the cooling is also connected to the sample receptor as mobile metal evaporators turned out to heat up the sample receptor too much and weaken the Inconel springs.

the beam line to minimise contamination of the vacuum chamber.

### 3.4.4 Molecule deposition techniques

A prerequisite for the investigation of individual molecules on surfaces in an atomically clean environment is the deposition of intact molecules without contaminations from the deposition process. This section provides a short overview of techniques employed and describes the implementation of those techniques used here.

Molecules are typically provided as a powder with  $\sim 95\text{-}99\%$  purity, contaminated mostly by the solvent from synthesis. The standard deposition technique employed is sublimation of molecule powder *in vacuo* directly onto the substrate, without any additional preparation step required. The molecules are heated in a Knudsen cell until they sublime. This technique also provides means to clean the evaporant: setting the crucible temperature slightly below the sublimation temperature of the molecules makes species with higher vapour pressure, in particular the solvent, outgas. This technique therefore provides preparations with a very high degree of cleanliness. Also, preparation of individual molecules is possible: molecules are simply deposited onto a cooled surface, suppressing their mobility. The technique however faces some limitations. Molecules with very high vapour pressure contaminate the vacuum chamber by raising its pressure (e.g., 1,3,5-Tribromobenzene), or even leave the crucible before heating. A vast number of molecular species, namely most classes of single-molecule magnets with their rather complex and fragile geometry [6], dissociate at a temperature below their sublimation temperature. Also, fragile molecules might dissociate or deform when landing on the substrate. This means a severe limitation for the choice of molecules, very noticeable indeed for the class of single-molecule magnets, where only a few could be prepared *in vacuo*, and only for LnPc<sub>2</sub> both intact deposition and a high degree of cleanliness could be achieved so far [47, 11].

Other *in situ* preparation methods include deposition from gas or liquid phase from external vessels via leak valves or pulsed valves, respectively. Soft-landing techniques employing argon layers adsorbed on the surface tackle the problem of dissociation upon landing. *Ex situ* preparations do not provide a sufficiently high level of cleanliness. Annealing the substrate after deposition can remove contaminations, but also increases the mobility of molecules and makes them form assemblies, prohibiting the investigation of individual molecules. Inert surfaces can also decrease desorption of contaminants, but magnetic surface layers typically used for SP-STM (Fe, Co) are rather reactive. Substrates or films which are both magnetic and inert could therefore widen the scope of molecules investigated by SP-STM. Methods rarely used are a

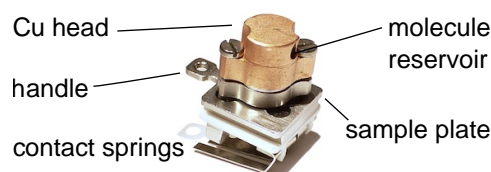


Figure 3.9: **Mobile molecule evaporator.** The Knudsen cell evaporator is mounted on a sample plate fitting into standard sample receptors. The copper head is mounted on a button heater whose electrical contacts are provided by four springs on the bottom of the mobile evaporator. The image size corresponds to the actual size of the evaporator.

stamp imprinting technique successfully employed by Vitali *et al.* [11], and electrospray deposition with mass selection which just very recently scaled down from lab scale to small devices attachable to chambers.

### Mobile molecule evaporators

In the present system, the thermal sublimation technique is implemented by using small mobile molecule evaporators (Figure 3.9). They are mounted on sample plates fitting into receptors designed for regular sample plates and therefore share wobble sticks, transfer rods, and storage space with them. This mobility makes it possible to introduce molecules to the vacuum chamber via the load lock, quickly exchange molecule evaporators to allow for deposition of several species on the same substrate, and deposit both on warm (in the preparation chamber) and cold (from a second stage in the STM chamber) substrates without the need for a second evaporator. The crucible is a small copper cylinder with a bore hole for the molecule powder. It is clamped to a commercially available button heater, ensuring reproducibility when exchanging evaporators. Button heaters and crucible dimensions are identical to those used in a VT-STM system [65] of the group to keep deposition parameters comparable. The button heaters offer a convincing design to minimise heat transfer to the evaporator sample plate, being mounted on a thin-walled molybdenum tube. For high melting point evaporants (e.g., lead) or those being reactive to copper, molybdenum heads are used. As molybdenum is expensive and hard to machine, all but two crucibles are made from copper. The mobile molecule evaporator has four contacts wired to the two heater contacts, allowing for a four-point measurement on the heater. This tells the voltage drop over the heater, independent of cable and contact resistances, and is used for faster heating (section 3.9.4).

### Ceramic crucible evaporators

A further miniaturisation of mobile molecule evaporators is achieved following a design by Knud Lämmle [66]. A small ceramic (Shapal-M) crucible is heated by a tungsten wire wrapped around it. The bore hole is smaller by about a factor of two compared to the standard copper crucibles. This is not a problem as the quantity of molecular powder needed is yet smaller, still being sufficient for several months of experiment. Due to its small size, the evaporator draws less heating power (in case of  $\text{TbPc}_2$   $P \approx 1$  W vs.  $\approx 2.5$  W) and reaches the final temperature faster. Disadvantages of these evaporators are a lower stability as the heating wire is also used as support, and variation of heating parameters between different units as the position of the heating wire is not sufficiently well-defined.

### 3.4.5 Gas inlet stage

As mentioned above, alternative molecule deposition techniques include deposition from liquid or gas phase through valves into the vacuum chamber. Equipment for this purpose is installed in the STM chamber.

Deposition in the STM chamber provides the option of deposition on cold sample substrates. For molecules from gas phase this is necessary to make the volatile molecules stick on the surface. For molecules from liquid, the solvent needs to be separated *in vacuo* by annealing the substrate. The desired sample temperature still might be below room temperature to ensure molecular self-assembly does not set in yet, so the option of a preparation in the STM rather than the preparation chamber is desirable. Vessels with molecules in gas phase or liquid phase are attached externally to the system. The inlet is controlled by a leak valve and by a pulsed valve, respectively. Two tubes guide the molecules to the sample surface right within the STM. The tubes have to pass several cooling shields. To avoid thermal connection to room temperature, those are not thermally connected, and holes are kept small to minimise radiation heat input. The straight tube passing through a hole in the  $\text{LN}_2$  shield can be retracted with a z shift to permit the shield to be opened and closed. The removable tube is pushed into a cone attached to the  $\text{L}^4\text{He}$  shield. This cone is attached to the second, rigid, tube which ends just before (to avoid thermal contact) an opening in the 1K shield around the STM. To guide the molecules onto the horizontal sample surface, the tube approaches from below, and is bent to account for this. To avoid condensation or adsorption of molecules on the wall of the cold tube, it can be heated by driving current through it. One electric contact is provided by the chamber ground, the other by the approaching tube itself; as the front

of the tube ends open, the ground contact is provided by a wire connected to the cooling shield. The outermost part of the gas inlet stage provides two flanges for inlet, one pointing in-line, the other equipped with a bent tube pointing into the outermost cone.

## 3.5 LEED/Auger system

The setup employs a commercial “Omicron SPECTALEED” LEED/Auger system mounted in the rear of the preparation chamber. As LEED and Auger are volume-averaging techniques, they are not particularly useful for the investigation of individual molecules, nor do they provide a sufficient resolution to determine sample cleanliness on the very high level needed for STM. Molecular self-assemblies, however, can be investigated by LEED. Furthermore, isolated molecules sticking on well-defined positions of patterned samples [67] could be investigated.

### 3.5.1 Test measurements

To check the working condition of the LEED/Auger system, test measurements were performed. Clean Cu(111) and Cu(100) crystals were investigated and show clear LEED patterns as shown in Figure 3.5.1. Further details can be found in the diploma thesis of Matthias Nohme [68]. The Auger functionality was also used to check the adsorption of NaCl; both elements could be identified.

## 3.6 Satellite preparation chamber

The satellite preparation chamber serves the purpose of crystal preparation at very high temperatures in the absence of potentially contaminating molecules. The main preparation chamber, in contrast, stores a number of molecules, some of which might also be reactive to the oxygen which is needed for oxygen annealing of crystals. The satellite preparation chamber is mounted next to the main preparation chamber between LEED and transfer rod. Sample transfer between the chambers is performed by a dual shaft transfer rod which moves the sample and rotates it towards the wobble sticks. The satellite chamber is pumped by an ion getter pump and a turbomolecular pump shared with the load lock. This section describes the electron heating stage and its refinements (section 3.6.1) and the later added cooling stage (section 3.6.2) in more detail. The satellite chamber itself including the electron beam heating stage and the transfer rod were designed and partly

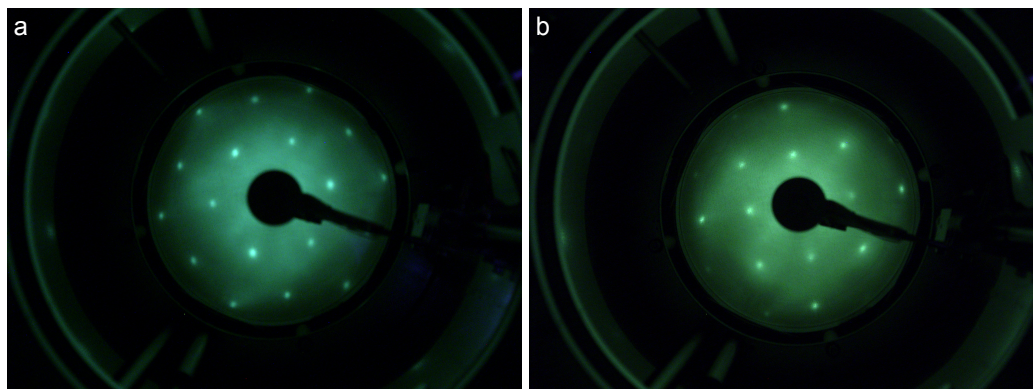


Figure 3.10: **Photographs of the LEED phosphor screen with patterns of Cu crystals.** (a) hexagonal LEED pattern of Cu(111) at  $E = 228$  eV. (b) square LEED pattern of Cu(100) at  $E = 213$  eV. LEED test performed and image taken by Matthias Nohme [68].

mounted by Matthias Nohme [68], installation and refinements of the electron beam heating stage, and design and installation of the cooling stage as well as assembly of the home-built metal evaporator were done by me.

### 3.6.1 Electron beam heating stage

A number of crystals cannot be cleaned with the sputtering and annealing facilities of the main preparation chamber only, but need to be flashed or annealed to higher temperatures of up to  $T = 2000^\circ\text{C}$ , exceeding the capabilities of the stainless steel transfer stage of the main preparation chamber. The satellite preparation chamber offers a cleaner environment as molecular deposition and storage is performed in the main preparation chamber, where the high sample temperature could release molecules adsorbed to chamber walls by radiant heat.

The design of the functional parts of the electron beam heating stage is adopted from Meckler *et al.* [61]. The size and number of parts exposed to heat is kept small to keep the amount of material released upon heating low. Electrons are accelerated by high voltage from a heated filament towards the sample and heat it with their kinetic energy ( $P_{HV} \sim 2000 \text{ V} \cdot 0.2 \text{ A} = 400 \text{ W}$  for  $T = 2000^\circ\text{C}$ ). The heat input by radiation from the filament ( $P \lesssim 10.4 \text{ V} \cdot 3.6 \text{ A} = 37 \text{ W}$ ) is much smaller.

The sample is held by two tungsten rods with slits cut by electrical discharge machining. The rods are connected to high voltage and insulated from

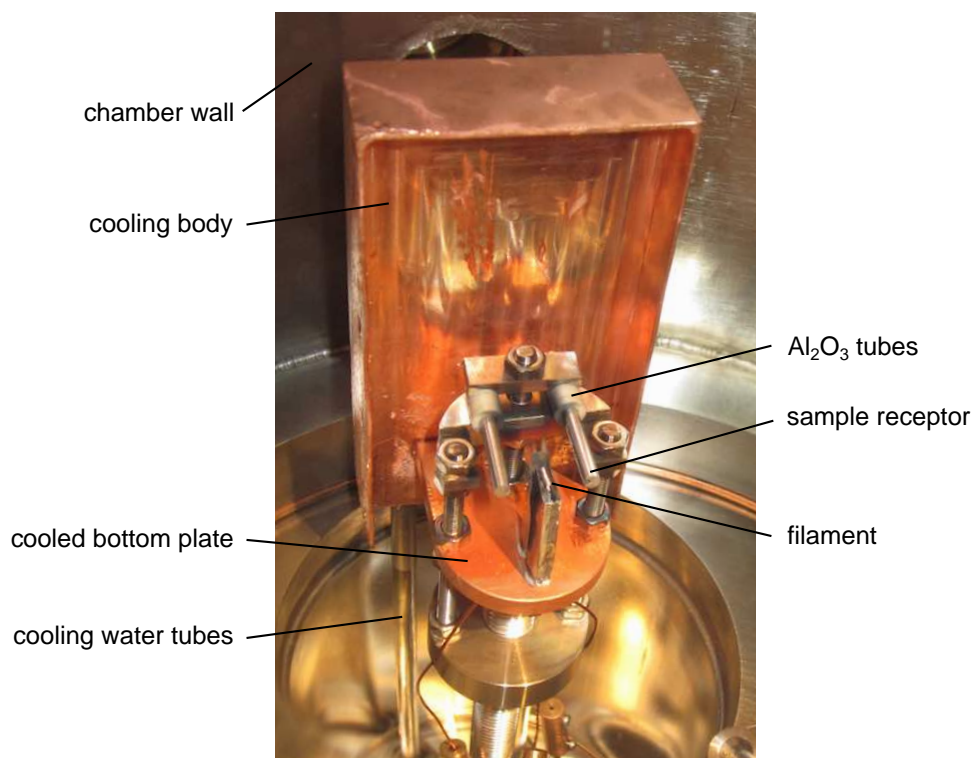


Figure 3.11: **Electron beam heating stage.** The sample receptor is electrically insulated from ground to be set to a high voltage. The high voltage accelerates electrons from the filament to the sample, heating it to up to  $T = 2000^{\circ}\text{C}$  for cleaning. To minimise pressure increase due to particles released from chamber walls because of thermal radiation, cooled shields (copper) are employed to block thermal radiation.

the support by  $\text{Al}_2\text{O}_3$  spacers. The filament mounted close to the sample plate plane is taken from commercial halogen bulbs (50 W, OSRAM) by cracking and removing the glass bulb. It is surrounded by a thin tantalum foil connected to a filament electrode to shape the electric field and thereby focus the electron beam. The filament can easily be exchanged by manually removing it from the socket.

The main difference and improvement over the previous design is a cooling shield surrounding the sample (Matthias Nohme [68]). This is introduced as the thermal radiation of the sample heats up chamber walls exposed to it. Heated walls release adsorbates, thereby increasing the background pressure and contaminating the sample during the cleaning process. The design of the cooling shield used here comprises a solid panel behind the sample, which is directly cooled by cooling water flowing through a  $\varnothing = 6$  mm tube, and a front door connected by copper braids. The electron beam heating stage was assembled according to these plans. Tests of both flashing and annealing a dummy tungsten sample resulted in exceedingly high pressure increases ( $p > 10^{-8}$  mbar) despite the water cooling. Type K thermocouples added to check the temperatures of the cooling shield showed that all cooled components but the rear copper panel heated up by more than  $100^\circ\text{C}$ , raising the pressure even after extensive bake-out. A quick calculation based on Fourier's law of heat conduction with the thermal load derived from the electric power of electron beam heating reveals that the dimensions of the front door as well as the cross-sectional area of the copper braids were designed much too small. A thicker front door ( $> 3$  mm) and thicker or more copper braids could improve this, but the cooling braids are mounted onto an only 1 mm wide plate directly connected to the rear panel, giving the bottleneck of cooling. Also, the copper braids have a large surface area and are moved when the door is opened (i.e. when the sample is clean!) raising the pressure due to friction. Therefore, a simpler solution was realised: front door and its copper braids are removed. The rear cooling panel stays in place as it is cooled effectively and blocks thermal radiation to the closest wall. The top window is close as well, but was not shielded from radiation anyway as optical access to the sample is needed to determine its temperature by a pyrometer. All other components are sufficiently far away from the sample. A new copper bottom plate is fixed rigidly to the rear panel, omitting the copper braid used before. With the new configuration, the pressure stays below  $\sim 10^{-9}$  mbar.

### 3.6.2 Cooling stage

Some preparations, for example oxygen treatment of Si surfaces, require the sample to be kept at temperatures lower than room temperature. The cooling

stage mounted in the satellite preparation chamber adds this functionality.

The oxygen gas inlet (for annealing samples in the electron beam heating stage) is installed in the satellite preparation chamber, so a cooling stage was designed for the latter. The cooling body follows a design home-built in the group of Prof. Qi-Kun Xue. The cooling stage is cooled by liquid nitrogen. Its temperature can be controlled to higher temperatures between LN<sub>2</sub> and room temperature by a heating filament located at the end of the cooling body. The temperature is read by a type E thermocouple, which is more sensitive at temperatures close to 77 K than the standard type K. The liquid nitrogen enters the cooling body through a central tube ending close to the end. The back flow is slowed down by blocking sections swirling the flow. The sample receptor is designed to keep the sample exposed to the bottom flanges, one of which is already equipped with a metal evaporator.

## 3.7 STM chamber

The STM chamber contains the cryostat with the STM. Its shape closely follows the dimensions of the cryostat. The number of additional devices in the STM chamber is kept to a minimum, as the microscope should not be exposed to contaminating processes, and replacement or repair in the STM chamber is slow due to long warm-up, bake-out, and cool-down periods of the cryostat. Those facilities which require low temperatures need to be located in the cryostat, i.e. in the STM chamber, such as devices for deposition of isolated molecules (section 3.4.5 and 3.7.1) and for cooled storage of samples (section 3.7.2).

### 3.7.1 Molecule evaporator stage

The molecule evaporator stage in the STM chamber allows for deposition of molecules directly onto the cold sample surface in the STM. This is mandatory for the preparation of individual molecules (section 3.4.4). During deposition, the radiation shutters remain closed, minimising thermal load from room temperature radiation, and avoiding release of hydrogen from moving parts. Repair or replacement of the molecule evaporator stage does not require disassembly of the cryostat, but the stage can be taken out through the front CF63 flange. To make this possible, its wires can be disconnected by removing the plug in the front part of the stage.

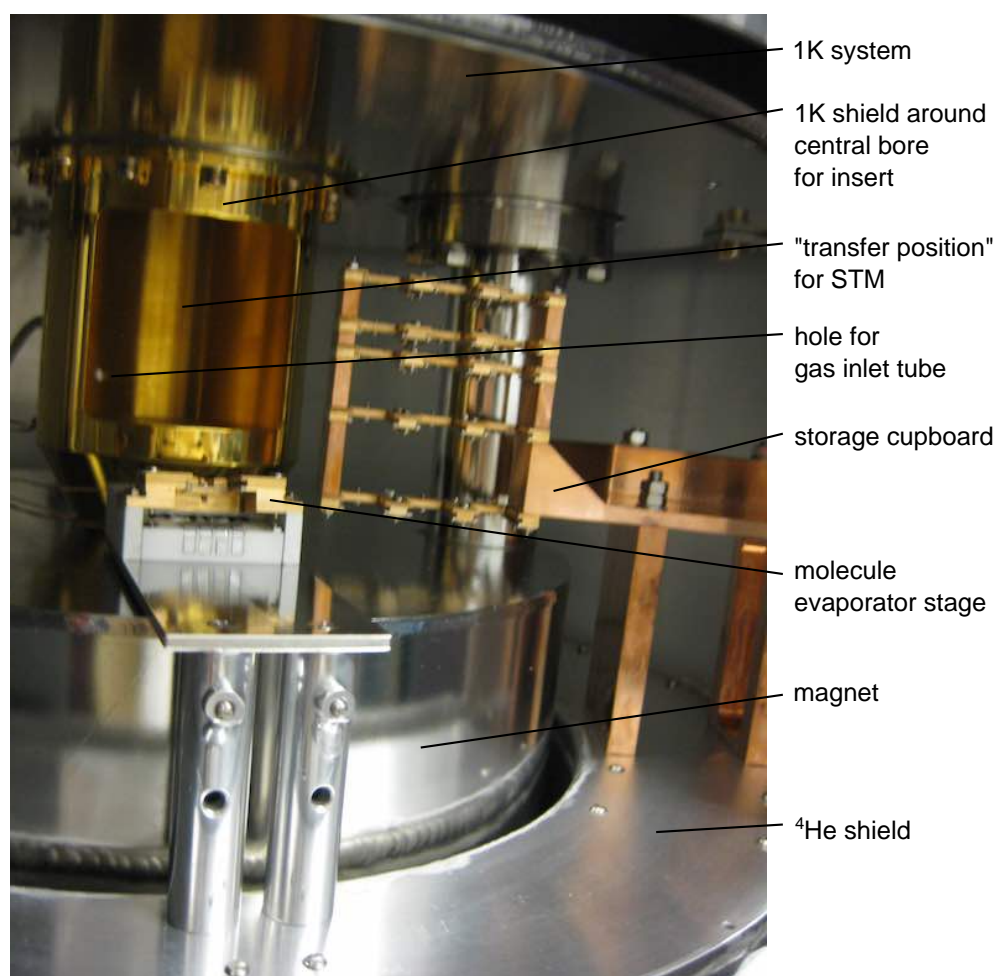


Figure 3.12: **Transfer plane in STM chamber**, between 1K system (top) and magnet (bottom), accessible to the user by the wobble stick. The central gold-plated cylinder contains the STM when the insert is in transfer position. The molecule evaporator stage as well as the hole for gas inlet point towards it for deposition of molecules onto a cold sample surface.

### 3.7.2 Storage cupboard

The storage cupboard in the STM chamber provides storage space for samples, molecule evaporators, tips and others, kept at low temperature ( $T \sim 4$  K) and protected from contaminating preparation processes. This can be particularly useful for example to conserve a sample preparation during tip exchange, suppressing mobility of surface films or individual molecules. It is mounted on the rather distant bottom of the  $^4\text{He}$  shield, as contact to the 1K-system above is avoided in order not to give heat input and mounting on the magnet housing below is not possible as belated adding of anchors was not feasible. For future additions of other devices, a number of tapped holes was drilled into the bottom plate of the shield, and for the present sealed by dummy screws to block thermal radiation. As the storage cupboard is mounted very close to the magnet in its stray field, normal, weakly magnetic stainless steel cannot be used. For sample receptors, phosphor bronze is used for stability, all other bulk parts are made from copper for good thermal conductivity. Screws and nuts are made from non-magnetic V4A stainless steel, sample receptor springs from Inconel 718, which exhibits a relative permeability of less than 1.0032 below 5 K [69, p. 584].

## 3.8 Microscope

This section describes the scanning tunnelling microscope, which has a design similar to a number of STMs in the group [70, 60] and was built by Robert Ravlić. It is mounted at the lower end of the  $^3\text{He}$  insert.

The microscope is compact to be rigid against vibrations and to fit into the narrow bore of the magnet. To avoid thermal fluctuations, the microscope body is made from phosphorous bronze, a material with rather low thermal conductivity and high thermal capacity (as compared to copper, at low temperatures). The phosphorous bronze parts are coated with a  $5\ \mu\text{m}$  gold layer<sup>3</sup> to reflect thermal radiation and enhance thermal contact. The sample is mounted face down in the sample receptor, which is electrically insulated from the microscope body by a thin sapphire (for high thermal conductivity) plate. The spring keeping the sample in place is made from bronze rather than the weakly magnetic Inconel used for most other sample receptors in the system. The scanning motion as well as (nanometre scale)  $z$  motion of the tip is performed by applying high voltage (up to 300 V) to a piezo tube. This tube has five electrodes: four outer electrodes for lateral

---

<sup>3</sup>The gold plating is performed without a nickel barrier metal layer, which is normally used to suppress diffusion of copper atoms but cannot be employed in the magnetic field.

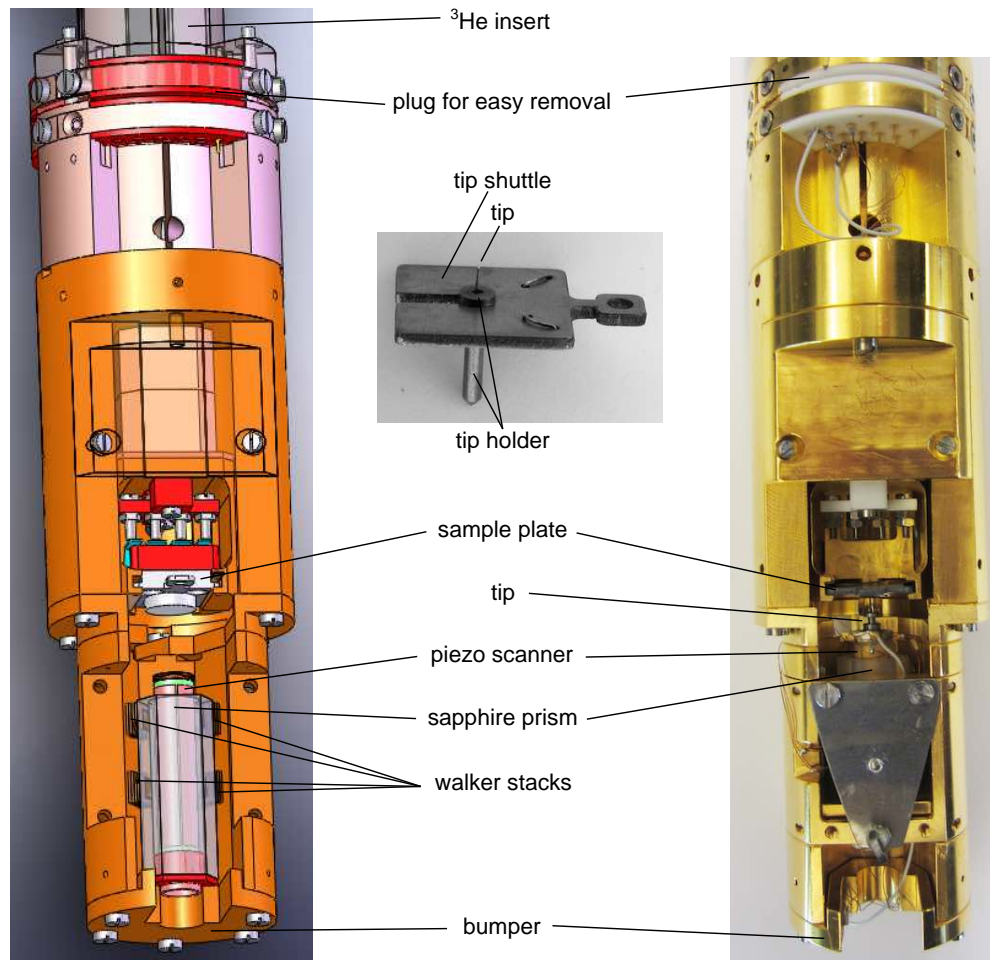


Figure 3.13: **Drawing and photograph of the STM.** The STM is attached to the bottom of the  $^3\text{He}$  insert using a home-built plug. The sample is mounted face down, with the tip approaching from below. The tip wire is fixed in a tip holder, which is plugged into the piezo scanner controlling its microscopic position. The sapphire prism contains the piezo scanner and can be moved for vertical coarse approach by piezo walker stacks. The bottom bumper prevents the scanner from falling down in case of piezo stack malfunction. The microscope body consists of phosphorous bronze and is coated with a thin layer of gold. Central image: tip shuttle with tip holder, for tip exchange.

(x,y) motion and one inner electrode for stretch (z) motion. For a motion in x direction, a voltage is applied to one of the outer electrodes (X+) and a voltage of opposite sign to the opposite electrode (X-). The piezo tube can retract the tip just by nanometres, which is an insufficient distance to insert the sample without touching the tip. The coarse approach is therefore performed by six piezo (“walker”) stacks glued to the STM body, moving a sapphire prism containing the piezo tube. The motion is based on a “slip-stick” scheme. A kilohertz sawtooth wave voltage is applied to all six walker stacks. At the ramp of the sawtooth wave, all six walker stacks perform a slow shear motion to one direction, with the sapphire prism following as the friction to the aluminium oxide plates glued on top of the walker stacks is sufficiently high. Then the sharp drop of the sawtooth wave makes the walker stacks move back quickly to their original position. The sapphire prism does not follow this backward movement, but slips owing to its inertia and the limited friction between alumina plates and the polished sapphire. To adjust the friction between too low (the scanner slides down by gravity) and too high (the prism doesn’t slip) a molybdenum spring presses the two front walkers against the sapphire. Thermal expansion of the microscope changes the resulting spring force when cooling down, so the spring needs to be re-adjusted at low temperature. For this purpose, a tungsten handle accessible by the wobble stick is glued onto one of the screws adjusting the distance of the spring. To make the spring less sensitive to temperature changes it is cut from the original rectangular shape to its current triangular shape, reducing its spring constant and thereby allowing for a larger displacement. To prevent the scanner from falling down in case of a much too weak spring, a bottom plate is installed on the microscope body, serving as a bumper.

### 3.8.1 Wiring

The wiring of the STM deserves attention for two reasons: first, the wires carry the measured signal, second, they give a significant contribution to thermal load, as they connect parts at 300 mK with room temperature. All electronics controlling the STM is situated outside the chamber. This also holds for the current preamplifier, which translates the tunnelling current  $I$  to a voltage. As the tunnelling current is very low ( $\sim 1$  pA to 1 nA), it is very vulnerable to external noise, so the preamp should be situated as close as possible to the STM. In-situ installation is, however, not possible because the preamp can’t operate in a high magnetic field. The preamplifier (femto DLPCA-200) is attached directly to the BNC vacuum feedthrough to avoid any unnecessary cabling between STM and preamp. To protect the  $I$  cable against external electromagnetic noise, coaxial cables are used all

the way through from the preamplifier to the STM tip. The shield connects the preamp to the tip. The shield is connected to the preamp ground but not the STM ground; its end connects to the electrically conductive paint on a cylinder around the tip holder to leave only the last 2 mm of the tip unshielded. For the other important signal cables, bias voltage  $U$  and piezo stretch voltage “ $Z$ ”, coaxial cables are used as well, whereas all other cables are not shielded to avoid the comparably fragile coaxial cable connections where not necessary. Within the STM, coaxial cables are elspec mk5001, which are very thin and flexible to follow the scanner for coarse approach. For the insert, these cannot be used as the copper conductors give a much too high thermal conductivity. Instead, stainless steel is used. The impedance of the wires differs, being  $50\ \Omega$  for the copper cable and the ex-situ BNC cable, and  $60\ \Omega$  for the stainless steel wire. This does not give significant reflections at the highest frequencies used ( $\sim 10\ \text{kHz}$ , limited by the frequency cut-off of the preamplifier), but might be significant for well-shaped pulses of a pump-probe scheme as in [62]. For now, experiments of this kind could not be performed with such a long wiring anyway, owing to high damping. Non-coaxial cables are chosen as thin as possible to minimise thermal load. Manganin is used, being a material with a high ratio of electrical conductivity to thermal conductivity, about a factor of 30 better than copper. The six walker piezo stacks are wired individually (still sharing the same ground) to be able to disable walker stacks individually in case of failure<sup>4</sup>. This way the STM remains operational, and immediate opening of the chamber for repair can be avoided. To keep the thermal input on the 300 mK part low, the wires are thermalised with the temperature gradient on the insert at several positions. Thermalisation is ensured by wrapping the wires multiple times around gold-plated copper cylinders.

### Grounding

To reduce electrical noise from grounding, the STM ground is separated from system ground. While the STM body is connected to system ground through the electrically conductive insert, the crucial STM signals are not: the piezo voltages of the scanner are applied with respect to each other, and the shields of the coaxial  $I$ ,  $U$ , and  $Z$  cables are open at the microscope side. The ground of these parts is therefore defined by the data acquisition electronics. With a vast number of laboratory devices potentially generating noise on the system ground, this offers the possibility of using a separate ground for the STM.

---

<sup>4</sup>Failure of soldering points on walker stacks is a problem even if leaving the stack operational; the stack then evaporates material owing to local heating, which adsorbs on neighbour stacks and gives shorts. Therefore, these stacks need to be disabled too.

The building provides a separate ground shared with the three neighbour labs. Using a separate ground also avoids ground loops.

### 3.8.2 Tip exchange

The possibility to exchange the tip *in situ* is crucial for SP-STM, as the tip needs to be magnetically coated. Tip preparation (flash to clean, deposit magnetic material, and anneal the magnetic film) is performed in the preparation chamber. The tip and its tip holder is taken out of the STM by using a tip shuttle which has a slit opening for the tip holder and holds it with a spring. To exchange the tip, the piezo scanner is driven up until the clearance of the tip holder is aligned with the sample plate plane, then the tip shuttle (Figure 3.13) can be inserted by the wobble stick into the sample receptor to make the tip holder slide into its opening. The shuttle grabs the tip holder with its spring; now the tip holder is kept tight in the tip shuttle. As the scanner moves down by the coarse approach mechanism, the tip holder stays with the shuttle and is pulled out of the scanner. When the top of the scanner is below the bottom end of the tip holder, the shuttle with the tip holder inside can be taken with the wobble stick, and subsequently transferred to the preparation chamber. To re-insert the tip, the tip shuttle with tip holder inside is pushed all the way into the sample receptor (the length of the tip shuttle opening and the shape of its spring are adjusted accordingly) and the scanner driven up to grab the tip holder. This requires more force than a normal tip-to-sample coarse approach, so a higher piezo voltage, and more intact walker stacks are required. While the scheme is straightforward, a tip exchange is nevertheless risky as the piezo ceramics scanner is very fragile and its cable connections are exposed. The very limited view, due to large distance and limited viewing angle (in particular, no view from top) increases the risk of damage. The crucial step is the precise positioning of the shuttle with respect to the tip holder. The flat tip shuttle makes it easy to align the tip holder clearance with the shuttle, in contrast to previous designs where a bulkier shuttle partially blocked the view. The bumper at the bottom of the STM prevents the scanner from falling down in case of handling error (or weakened front spring, see section 3.8).

## 3.9 Labview control

This section briefly describes a small number of Labview programs written to access and improve functionality of the system.

### 3.9.1 Microbalance

The microbalance program computes and monitors the deposition rate of molecules or other material on the microbalance. To do so, the microbalance frequency is read, averaged to improve the signal-to-noise ratio, and differentiated to give a rate rather than a film thickness. The statistical read error is  $\pm 0.15$  Hz (at 6 MHz), while a typical rate is about  $-1$  Hz/min. To receive a value for the rate within a couple of minutes, the frequency is read several times per minute and averaged over several read-outs.

### 3.9.2 Automated sample cleaning

The automated sample cleaning in the transfer stage is controlled by this Labview program written by Karl-Philip Gemmer. It controls the sputter gun including the automatic leak valve, the heating filament with possible high voltage on the sample for electron beam heating. Cycles of sputtering and subsequent annealing can be defined and scheduled, providing the ability of automated overnight sample cleaning.

### 3.9.3 Temperature control

This is a simple program plotting read-outs of the temperature sensors of the cryostat, useful for bake-out and  $^3\text{He}$  condensing procedure.

### 3.9.4 Quick heating of molecule evaporators

This program shortens the time needed for a mobile molecule evaporator to reach its final temperature. This is useful as the previously employed method of simply setting the desired current leads to unnecessarily long heating-up times and thereby to a significant loss of liquid helium when this is done in the STM chamber. It takes 45 minutes for a mobile molecule evaporator of the standard copper design to reach its final temperature. With typical parameters of  $I = 1.5$  A and  $U \sim 1.5$  V, the thermal energy generated is  $E = UIt = 1.5 \text{ A} \cdot 1.5 \text{ V} \cdot 45 \cdot 60 \text{ s} \approx 6 \text{ kJ}$ . As the evaporator and nearly everything exposed to its thermal radiation is cooled by  $^4\text{He}$ , this thermal energy needs to be removed by cooling with  $^4\text{He}$ . The amount of liquid helium needed, calculated from the heat enthalpy of vaporisation only, is  $V = \frac{E}{\Delta H_{\text{vap}}}$ .  $\frac{M(^4\text{He})}{\rho} = \frac{6 \text{ kJ}}{0.0829 \text{ kJ/mol}} \cdot \frac{4 \text{ g/mol}}{0.125 \text{ g/cm}^3} \approx 2300 \text{ cm}^3 \approx 2.31 \text{ } ^4\text{He}$ . Another concern is contamination by adsorbants released from warming up surfaces, in particular hydrogen. To save both liquid helium and time, and still use the standard mobile molecule evaporator (the smaller ceramic crucible evaporator, see

section 3.4.4, draws less power and heats up more quickly), a faster heating scheme is used. The button heater uses a metal coil as heater. Metals are positive temperature coefficient (PTC) thermistors, i.e. their resistance increases with temperature. This means that with the old method of setting a constant current, the heating power  $P = UI = RI^2$  rises with time.<sup>5</sup> Keeping the voltage constant instead gives the reverse effect of first heating with increased power. Still the evaporator reaches the final temperature asymptotically. The drawback of this method is that the voltage set at the power supply does not entirely drop over the evaporator heater, but the feed cable contributes as well, resulting in different power-supply voltages for the different stages in the preparation and the STM chamber. Setting a constant voltage directly at the power supply is therefore unfavourable, and external control is used. The Labview program reads (via an A/D board) the voltage drop over the evaporator using the 4-point contact and regulates the applied current accordingly. The resulting heating-up time is reduced from 45 to less than 20 minutes. A further decrease of heating-up time is feasible by regulating on the heater temperature, as determined by its PTC  $R(T)$  characteristics. However, with the first method already the current has to be limited to its maximum specified current for the first minutes. The second method could therefore save only little time, but introduces uncertainties such as the assumption of ohmic resistance at a given temperature, and overshooting temperature due to the PID loop. Nevertheless, the second method is implemented in the Labview program.

### 3.10 Sample transfer

To transport samples from the STM to the preparation chamber, the transfer rod of the preparation chamber is used. While granting free optical access to all fixed sample receptors in the STM chamber (STM, storage cupboard, and mobile evaporator stage), this is not the case for the sample receptors in the transfer rod when accessed with the STM wobble stick: when the wobble stick is pointing straight, the sample receptor in the transfer rod can only be seen through the lower right viewport and the viewport on axis with the transfer rod. The viewport on the lower left is blocked externally by the damping leg, and both side viewports don't give optical access to the spot as their CF63 tubes point towards the STM rather than to the transfer rod receptor, and

---

<sup>5</sup>A PTC set to constant current is in principle unstable, as temperature fluctuations can increase the temperature, resulting in an increase of resistance, thereby an increase of power as the current is kept constant, and thus another temperature increase, closing the loop. However, sufficiently high thermal energy loss to the environment prevents this.

are too narrow to grant off-axis view. Sample transfer using the lower right viewport for optical access is awkward as the off-axis CF63 viewport does not provide binocular vision, and the wobble stick has to be operated left-handed and overhead. This turned out to be a considerable problem, as the hand becomes shaky very quickly that way. This makes fragile sample holder handles break, and slows down the transfer. For some experiments, a fast transfer is needed, e.g., to stop room-temperature intermixing of thin cobalt films on Cu(111). Also, this viewport is normally blocked by the camera monitoring tip approach and exchange. To provide access to the port, a quick mount mechanism for fast removal and installation of the camera is installed, as tip approach follows shortly after sample transfer. Additionally, a pad is installed on the frame to provide rest for the left arm elbow; this measure provides significant improvement for motor activity. As transfer using this viewport is still challenging for those with less skilled left hands, the on-axis viewport is also considered for use. With on-axis view only, on-axis positioning of the sample in front of the sample receptor is not possible. Coarse grain aiming can be done by moving the wobble stick parallel to the frame. For precise positioning, a small piece of phosphorus bronze, which can be distinguished from other parts owing to its yellow colour, is glued onto the side of the sample receptor.

Both methods have proven to work, still this transfer is the by far most tedious one of the system. Other attempts to improve optical access by mirrors, or to transfer with inclination, did not provide satisfactory solutions. The problem emerged as all viewports are pointing towards the STM, and are of limited size. Larger CF100 viewports would have given a great advantage at reasonable cost, but can't be installed now unless the entire chamber is unmounted.

## Part III

# Experimental results and discussion



This experimental part is divided into two chapters; the first (chapter 4) tackles the spin-resolved investigation of  $\text{TbPc}_2$  adsorbed on ferromagnetic nanostructures, the second (chapter 5) reports on the switching between  $\text{TbPc}_2$  conformations on a non-magnetic surface.

The spin-resolved investigation of  $\text{TbPc}_2$  by means of SP-STM reveals that the lowest unoccupied molecular orbital (LUMO) is spin-split by 200 mV. This observation indicates that the molecule is charged upon adsorption due to a charge transfer from the substrate, and the ligand spin is quenched. No spin polarisation uniquely stemming from the terbium centre was observed.

Adsorbed on Ir(111),  $\text{TbPc}_2$  is found to show two stable conformations, one of which is chiral, the other achiral. At low temperature, the achiral conformation (present in two enantiomers) can be reliably switched into the chiral one by manipulation with the STM tip. A different manipulation scheme for the reversed switching from the achiral to the chiral conformation is found. This allows for switching between enantiomers, which was hereby demonstrated for the first time. Controlling chirality is of fundamental interest in chemistry and life sciences.



# Chapter 4

## SP-STM investigation of TbPc<sub>2</sub>

For the first SP-STM investigations of a single-molecule magnet, TbPc<sub>2</sub> is chosen because it exhibits one of the highest blocking temperatures observed so far, because it is comparably compact, is sublimable, adsorbs flat (and thus well-defined) onto surfaces [11], has been shown to retain SMM features upon adsorption on a metal surface [12], and exhibits signatures of Tb 4f states in (non-SP) STM [11].

TbPc<sub>2</sub> contains two electronic spin systems: the central Tb ion and the ligand spin. Ishikawa *et al.* [52] found the ligand spin to slow down reversal of magnetisation and thus stabilise the SMM TbPc<sub>2</sub> in a comparison of [TbPc<sub>2</sub>]<sup>0</sup> with ligand spin and [TbPc<sub>2</sub>]<sup>-</sup> without ligand spin. Komeda *et al.* [47] studied layered TbPc<sub>2</sub> by spin-averaging STM exploiting the Kondo effect and showed that the ligand spin can be switched on and off by rotating one Pc ligand. Vitali *et al.* [11] found that Tb 4f states are accessible to spin-averaging STM. Element specific techniques so far only investigated the coupling of Tb centre and magnetic substrates [71, 72], but not the role of the ligand spin. The high spatial resolution of STM, combined with its energy sensitivity and the spin sensitivity of SP-STM might resolve the ligand spin spatially and energetically, and separate it from effects stemming from the Tb centre.

SP-STM combines spin sensitivity, energy resolution and high spatial resolution [13]. Applying SP-STM to molecules, Iacovita *et al.* [14] have found spin contrast on the magnetic metal centre of CoPc on thin cobalt islands on Cu(111). Brede *et al.* [15] have found new spin-polarised hybrid states arising from high molecule–substrate interaction for CoPc on iron double layers on W(110). Spin-resolved images of pristine molecular orbitals have not been seen yet.

The present experimental setup offers a base temperature of 6 Kelvin. This is too high to directly investigate SMM hysteresis in the timeframe of STM imaging. Now, the first step is to visualise the spin systems. TbPc<sub>2</sub>

is placed on thin ferromagnetic nanostructures on a non-magnetic substrate. The magnetic nanostructures shall couple the magnetic moments of TbPc<sub>2</sub> to make them accessible to SP-STM.

## 4.1 Magnetic substrate system

The application of STM requires conducting substrates; metal substrates satisfy this condition. Thin layers of magnetic material on a non-magnetic metal single crystal represent a simple magnetic substrate system. Full crystals from magnetic metal are not used as they produce a high stray field. A magnetic substrate is chosen for two reasons: Firstly, the magnetisation of the molecules is defined by the magnetisation of the underlying substrate by exchange coupling. Secondly, the magnetic substrate serves as a reference to characterise the tip's spin polarisation. A non-magnetic crystal with thin ferromagnetic films grown on top (such as the similar Co/Cu(111) system used in [14] or the Fe/W(110) spin spiral system in [15, 16] for SP-STM on single-decker Pc molecules) offers both non-magnetic surface regions and magnetic surface domains with opposite magnetisation directions for different ferromagnetic islands. The tip's spin sensitivity can be quickly determined by taking point spectra above two islands with opposite magnetisation. Molecules adsorbed on islands with opposite magnetisation can also directly be compared. As TbPc<sub>2</sub> adsorbs flat on the surface and has an easy-axis magnetic anisotropy perpendicular to the Pc rings, a magnetic substrate with out-of-plane magnetisation is suitable. A common system for out-of-plane magnetised islands are triangular double-layer cobalt islands grown on Cu(111) [14, 73, 74, 75]. Bickel *et al.* [76] presented a very similar, yet more useful system of flat triangular monolayer cobalt islands grown on Ir(111). These islands have out-of-plane magnetisation, i.e. their magnetisation points either perpendicularly out of or into the plane. Unlike on copper, the cobalt atoms do not intermix with the iridium surface after a room-temperature preparation. This simplifies modelling by *ab initio* calculations and the experimental preparation process. In case of room temperature Co/Cu(111) preparation, intermixing continues while molecules are deposited on top, thereby limiting the deposition time. Also unlike Co/Cu(111), nearly all islands point towards the same direction, i.e. they follow the same crystal stacking. It remains unclear whether they follow fcc or hcp stacking. A key feature of Co/Ir(111) is the very high magnetic coercivity; the magnetisation of clean and well-shaped cobalt islands remains stable up to a field applied opposite to the magnetisation direction of the islands of 4 Tesla [76]. This means that comparably large magnetic fields can be applied without

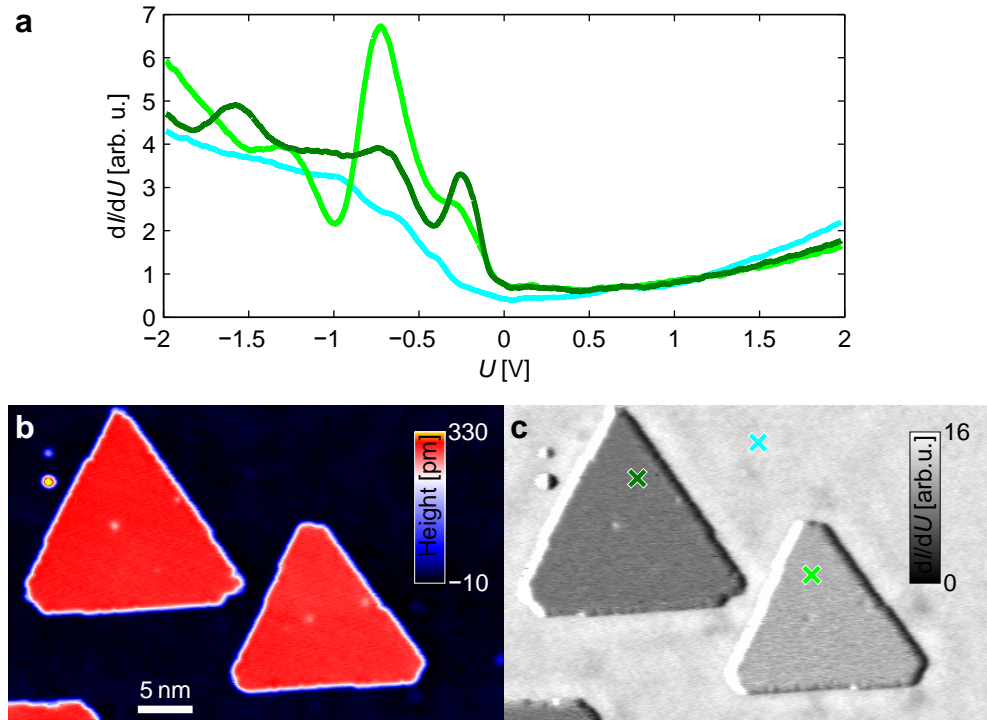


Figure 4.1: **Two oppositely magnetised cobalt islands on Ir(111).** (a) Point spectroscopy taken on both cobalt islands (green, dark green) and iridium (cyan).  $U_{\text{stab}} = +2$  V. Cobalt shows a pronounced peak at  $U = -0.25$  V with higher intensity in the minority (antiparallel alignment of tip and island magnetisation) spin channel (dark green). At  $U = -0.5$  V, the spin contrast reverses. (b) Topograph of two oppositely magnetised triangular cobalt islands on Iridium(111), taken with an iron coated tungsten tip with out-of-plane spin sensitivity. (c) Simultaneously recorded map of differential tunnelling conductance. The islands show different  $dI/dU$  intensity depending on their magnetisation direction.

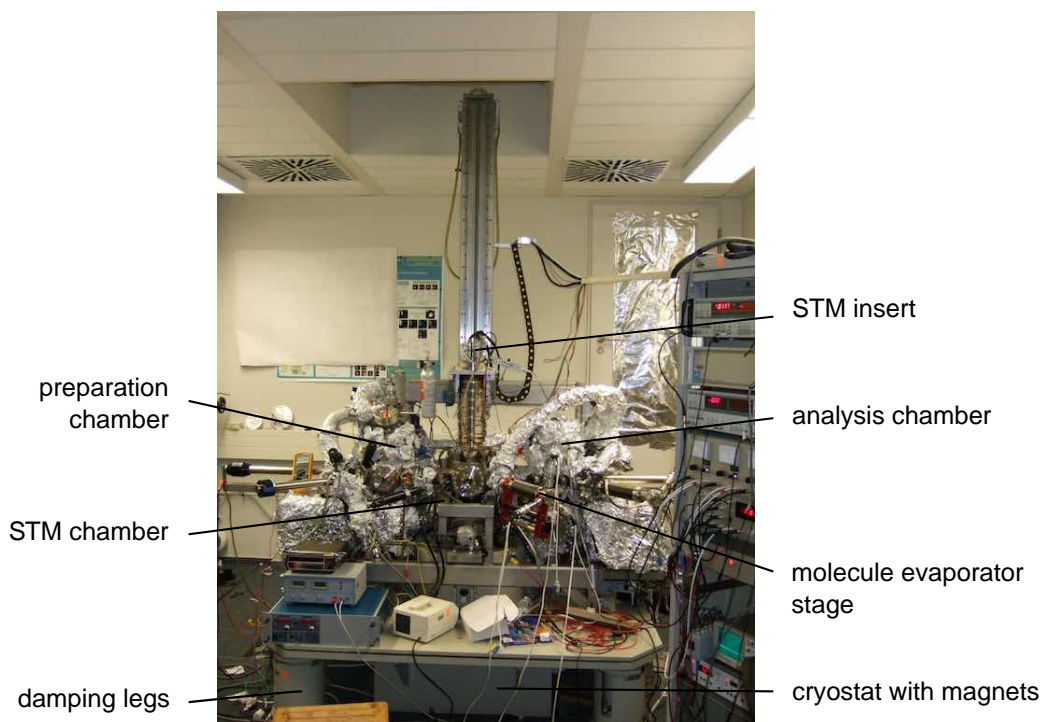


Figure 4.2: **Photograph of the 6 Kelvin STM system.** The STM system consists of a central STM chamber and satellite preparation (left) and analysis (right) chamber. The STM itself is mounted on an insert, which can be lowered into the cryostat.

switching the magnetisation direction of the sample, and allows to employ an SP-STM scheme as presented in chapter 1.6.

## 4.2 Experimental setup

The experiments reported in this part are performed with a  $^4\text{He}$  bath cryostat STM setup depicted in Figure 4.2. It operates under ultra-high vacuum conditions at  $T = 6\text{ K}$  and is equipped with two magnets to apply up to  $B = \pm 6\text{ T}$  perpendicular to the sample surface plane or  $\pm 2\text{ T}$  parallel to the surface plane. Samples and tips are cleaned in the preparation chamber. Co or Fe are deposited in the analysis chamber. Three molecular evaporators are available in the STM chamber, which houses a home-built STM. To avoid potential reactions of molecules with the crucible, the original Cu crucibles were replaced by ceramic crucibles made from Shapal-M (cf. chapter 3.4.4).

### 4.2.1 Sample preparation

The sample preparation described here is performed for experiments on  $\text{TbPc}_2$  on both bare iridium as well as on cobalt islands. All preparation steps are performed *in situ*, in ultra-high vacuum conditions. For cleaning, the iridium single crystal surface is sputtered with argon ions at  $E = 1500$  eV for 30 minutes, flashed to  $T = 1450$  K for 2 minutes, subsequently annealed in an oxygen atmosphere of  $p = 3 \dots 5 \cdot 10^{-7}$  mbar at  $T < 1400$  K for 30 minutes to reduce carbon contaminations, and flashed again for 3:30 minutes.<sup>1</sup> After cooling down for 30 minutes, cobalt is evaporated from an electron-beam metal evaporator onto the iridium sample kept at room temperature. At this temperature, cobalt atoms are mobile on the iridium surface and assemble to form islands.  $\text{TbPc}_2$  powder is heated in a ceramic Knudsen cell evaporator [66] to about  $400^\circ\text{C}$  to sublime.<sup>2</sup> For room-temperature deposition, the sample is kept at room temperature and exposed to the molecular beam. For an alternate low-temperature deposition, the sample is pre-cooled in the STM to about 40 K, then taken out and held in the wobble stick for deposition; the sample temperature is estimated to be roughly 100 K. Directly after molecule deposition the sample is transferred *in vacuo* into the STM, and the STM is subsequently cooled down to  $T = 6$  K.

### 4.2.2 Tip preparation

The tip preparation follows a well-established procedure, similar to the one described in chapter 3.8.2. The tip exchange is possible via tip shuttles fitting into sample receptors, and tip holders both fitting the STM scanner and the tip shuttles. This way, tips can be removed from the STM, cleaned, coated, and put back into the STM *in vacuo*. A flash to  $T \sim 2250$  K at the electron beam heating stage in the preparation chamber cleans the tip. The electron-beam metal evaporator in the analysis chamber deposits about 50 atomic layers of iron onto the tip. Radiative heating to about 500 K on the electron-beam heating stage in the preparation chamber anneals the iron film. The iron film exhibits in-plane spin sensitivity in absence of an external magnetic field [13]. However, the film acts as a soft magnet, so external magnetic fields align its magnetisation and spin sensitivity direction.

---

<sup>1</sup>The cleaning recipe differs from the neighbour lab where a yet longer “flash” at lower temperature is performed [76]. Here, lower temperature proved insufficient to remove all carbon released in the annealing process, possibly due to the higher amount of carbon from organic molecules.

<sup>2</sup>This value is inferred from evaporation from calibrated copper crucibles, as the ceramic crucibles used here are not equipped with temperature sensors.

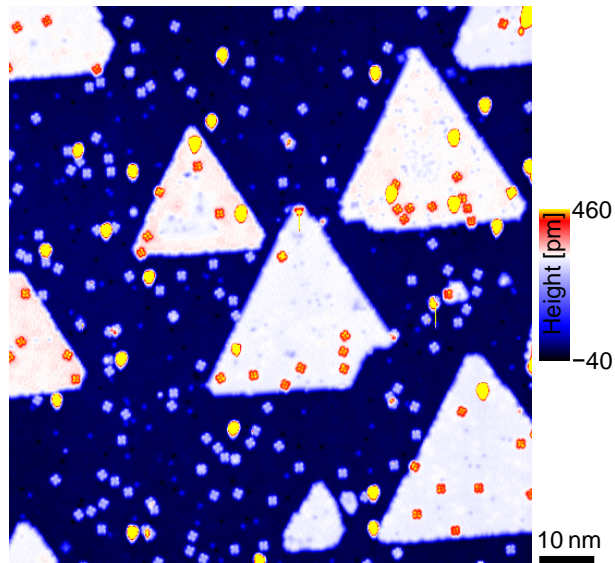


Figure 4.3: **Large surface area with  $\text{TbPc}_2$  molecules on Co/Ir(111).** Cross-shaped  $\text{TbPc}_2$  molecules (red and light blue) adsorb individually both on cobalt islands (appearing white) and bare iridium (dark blue).  $U = -0.5$  V,  $I = 600$  pA, W tip. Data recorded by Yingshuang Fu.

### 4.3 Spin-averaged investigation of $\text{TbPc}_2$ on Co/Ir(111)

This chapter reports on  $\text{TbPc}_2$  molecules adsorbed on cobalt islands. The ultimate goal of this experiment is a spin-resolved investigation, aiming at conclusions about the magnetic properties of  $\text{TbPc}_2$  and its coupling to the substrate. The first sections present the basic work, using conventional spin-averaged STM to investigate adsorption, conformations, geometric structure and spin-averaged electronic structure.

Figure 4.3 presents a typical topograph of the resulting substrate system. The topograph shows the bare iridium substrate and triangular cobalt islands. Well separated cross-like shaped objects of about two nanometre lateral size are distributed randomly on both iridium and cobalt:  $\text{TbPc}_2$  molecules. Despite the fact that the sample is held at room temperature for deposition, the molecules are homogeneously distributed over the substrate, and they do not cluster at step edges and island rims. This low mobility indicates a strong molecule–substrate interaction which immobilises the molecules even at room temperature. In contrast,  $\text{TbPc}_2$  deposited on Au(111) [47] assemble to layers, indicating a weaker molecule–substrate interaction typical

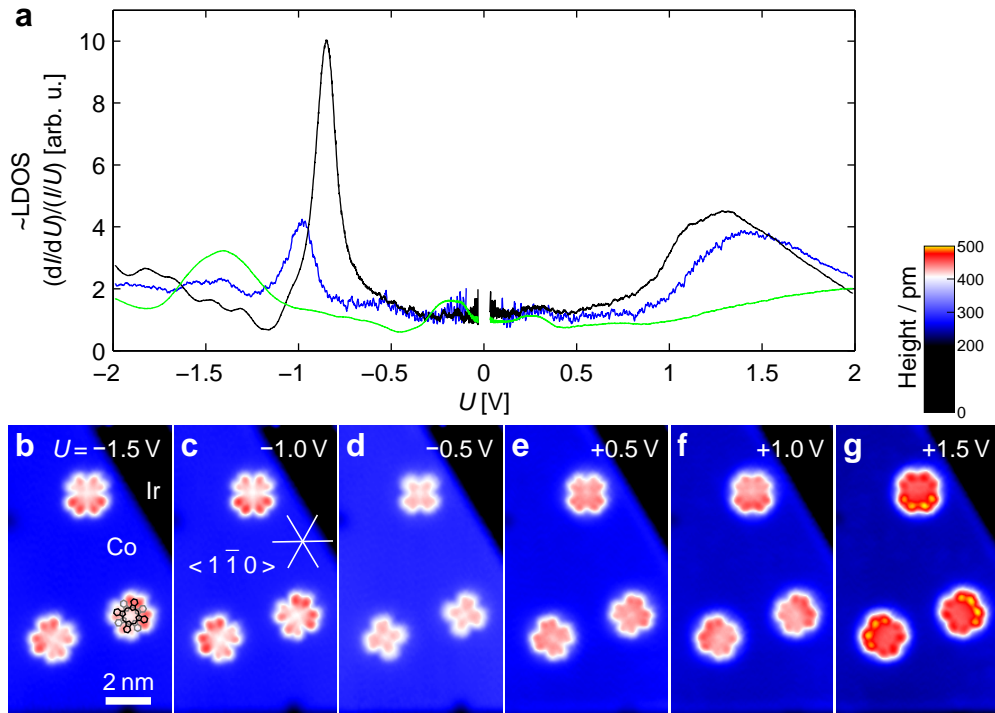


Figure 4.4: **Point spectroscopy and energy-dependent topography of  $\text{TbPc}_2/\text{Co}/\text{Ir}(111)$ .** (a) Point spectra taken above molecular lobes (black), centre (blue), and cobalt island (green). The  $dI/dU$  signal is normalised by dividing by  $(I/U)$ , the resulting quantity is dimensionless.  $U_{\text{stab}} = +2$  V,  $I_{\text{stab}} = 1$  nA,  $f_{\text{mod}} = 6777$  Hz,  $U_{\text{mod}} = 20$  mV<sub>rms</sub>. (b-g) Topographs of three  $\text{TbPc}_2$  molecules on Co (blue) on Ir(111) (black). The island rim follows an iridium close-packed row. Height is given with respect to the iridium surface.  $I = 100$  pA, W tip.

for the more inert gold substrate.

The next steps of the spin-averaged investigation are energy-dependent topography,  $dI/dU$  maps, and point spectroscopy to reveal the spin-averaged electronic structure of  $\text{TbPc}_2$  on  $\text{Co}/\text{Ir}(111)$ .

The topographs in Figure 4.4b-g show three molecules adsorbed on cobalt in higher resolution. They appear identical apart from being rotated by  $120^\circ$  with respect to each other, following the hexagonal symmetry of the surface. They appear 140 to 240 pm high, depending on the applied bias voltage. Given the much larger lateral size of 1.8 nm, the molecules adsorb flat on the surface. They are stable at reasonable tunnelling parameters ( $|U| \lesssim 3$  V,  $I \lesssim 3$  nA), that is, they do not move, desorb or decompose in this bias voltage and current range.

Above a bias voltage with absolute magnitude  $\geq 1$  Volt, all molecules show eight pronounced lobes, arranged in four pairs. Lower bias voltages show only four lobes, clearly revealing a cross-like appearance. Point spectroscopy performed above one of the eight lobes (Figure 4.4a) reveals a sharp peak at  $-0.875$  V, and a wide peak centred at about  $+1.3$  V. Both energies correspond with the eight-lobe appearance in topography. Between these two peaks, the LDOS is significantly lower. They are therefore identified as the highest occupied molecular orbital (HOMO) and lowest unoccupied molecular orbital (LUMO), respectively. The point spectrum taken over the molecular centre also reveals two peaks at very similar energies, both shifted away from the Fermi level.<sup>3</sup> The overall shape of the spectrum, i.e. a sharp HOMO, a wider LUMO, a HOMO–LUMO gap size of about  $1.9$  eV, agrees well with findings by Zhang *et al.* [77, Figure 2c] for YPc<sub>2</sub> on Au(111) and by Fahrendorf *et al.* [78] for NdPc<sub>2</sub> on Cu(100). The eight-lobe appearance of the frontier orbitals (HOMO and LUMO) is highly reminiscent of single-decker Pc molecules adsorbed on decoupling layers [79, 80] and represents their  $\pi$  orbitals. The topographs therefore image the molecular orbital of the upper Pc ring, which is hardly disturbed by the adsorption on the metal substrate.

Between HOMO and LUMO, in the “HOMO–LUMO gap”,<sup>4</sup> the lobes appear  $\sim 50$  pm lower than at bias voltages corresponding to HOMO or LUMO. The reason for this reduction of apparent height is the considerably lower local density of states, as clearly visible in the point spectrum (Figure 4.4a). As the frontier orbitals are not accessible by low bias voltages  $|U| < 0.7$  V, STM images the shape of the molecular backbone [67]. The four-lobed cross visible in the topograph taken at  $U = -0.5$  V therefore follows the upper Pc ring.

Both HOMO–LUMO gap appearance as well as the eight-lobe orbital follow the geometry of the upper Pc ring. The axes of this upper Pc cross are rotated by  $45^\circ$  with respect to a close-packed row of the iridium substrate, visible from cobalt island edges. In contrast, several single-decker Pcs have been found to align with close-packed rows of different fcc(111)

---

<sup>3</sup>For a weakly adsorbed molecule, or a well decoupled upper Pc ring, such a shift would be qualitatively expected: in a double barrier junction picture, a smaller tip–sample distance lowers the effective bias potential on the molecule, and thereby makes the peaks shift to higher energies. Here, this is tested by performing point spectroscopy with an increased ( $+100$  pm) tip–sample distance. The HOMO does shift outwards, but only by  $15$  mV, much smaller than the peak shift observed here. A shift on the LUMO is not discernible, as the LUMO is much wider than such a shift.

<sup>4</sup>The presence of density of states within the “gap” indicates that the HOMO–LUMO gap is not a perfect gap.

surfaces [81, 82]. Combining these two observations, the internal staggering angle of TbPc<sub>2</sub> adsorbed on cobalt is found to be 45°.

The apparent height of TbPc<sub>2</sub> adsorbed on Co/Ir(111) is about 180 to 240 pm, depending on the bias voltage. Literature values for Pc<sub>2</sub> on other metal substrates are significantly higher and range from about 300 to 400 pm [83, 11, 47]. This difference can partly be explained by the electronic configuration of the cobalt surface. The high density of states of the cobalt surface close to the Fermi level [76] makes the cobalt surface appear higher by roughly 60 pm, and the molecule lower in comparison.

A wider voltage range from -3.5 to +3.5 V does not reveal any feature that is unique to the centre, and thereby unique to the central terbium ion. Also, the investigated bias voltage range does not show the cross-like structure observed by Vitali *et al.* [11, Figure 4a, centre], which they assign to 4f states. Thus, no direct access to the SMM features of TbPc<sub>2</sub> is found in this spin-averaging study, in agreement with Zhang *et al.* [84].

### 4.3.1 Decomplexation

In general, decomplexation of TbPc<sub>2</sub> is the removal of a Pc ligand. In the case of surface adsorbed species, the upper ligand is removed. Here, the decomplexation is performed through a manipulation by the STM tip. This decomplexation experiment is applied in order to shed light on two questions: Is the investigated adsorbant an intact double-decker or a single-decker Pc, and if it is a double-decker, what is the internal staggering angle?

In literature, both double-deckers and single-deckers are found after thermal evaporation of double-decker Pcs. Katoh *et al.* [85] conclude that double-deckers decompose. In the present study, it is not entirely clear yet which species is present. Only one species is found after deposition. While the eight-lobe appearance in Figure 4.4 clearly indicates a double-decker, the comparably low apparent height rather resembles data found for single-decker molecules adsorbed on other surfaces.

Different internal staggering angles are found in literature. Komeda *et al.* [47] find layered TbPc<sub>2</sub> on Au(111) to exhibit two different staggering angles, 30° and 45°. Also, eclipsed rather than staggered double-deckers have been suggested to be stable [86]. In the present study, the staggering angle is not immediately discernible as the lower Pc ring is not directly visible to STM.

Both issues can be resolved by removing the upper Pc ligand: To prove that the double-decker is intact, and to find the staggering angle, manipulation by the STM tip is performed in order to split the double-decker molecule into two halves. For manipulation, the STM tip is stabilised next

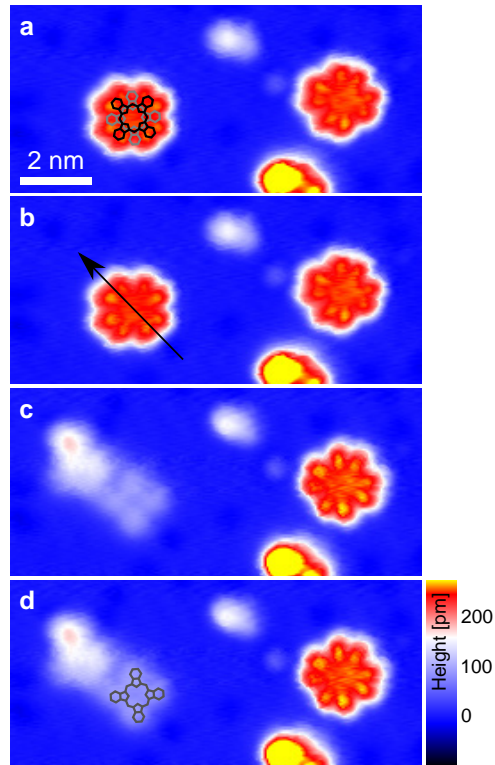


Figure 4.5: **Decomplexation of  $TbPc_2$  via manipulation by the STM tip.** (a) Topograph of two  $TbPc_2$  double-deckers on Ir(111). The structure model shows the direction of the upper Pc ring in black.  $U = -1.05$  V,  $I = 200$  pA. (b) Lateral manipulation by the STM tip to remove the upper Pc ligand. The tip is stabilised at  $U = +0.3$  V and  $I = 50$  nA. The feedback loop is opened and the tip dragged as indicated by the black arrow, in constant height and with  $400$  Å/s. (c) Subsequently recorded topograph, showing a remaining single-decker Pc. (d) The geometry of the remaining Pc follows the  $45^\circ$  rotated lower Pc ring in (a).

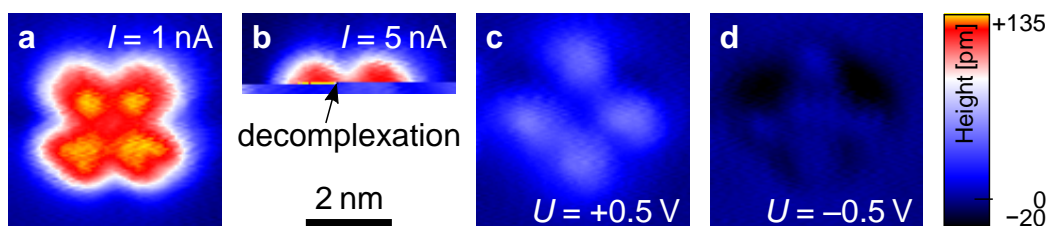


Figure 4.6: **Decomplexation of  $\text{TbPc}_2$  by elevated tunnelling current.** Sequence of topographs of a  $\text{TbPc}_2$  double-decker on a cobalt island on  $\text{Ir}(111)$ . (a)  $U = -0.5 \text{ V}$ ,  $I = 1 \text{ nA}$ . (b)  $U = -0.5 \text{ V}$ ,  $I = 5 \text{ nA}$ ; at elevated tunnelling current, the double-decker decomplexates. (c)  $U = +0.5 \text{ V}$ ,  $I = 1 \text{ nA}$ ; remaining single-decker Pc, rotated by  $45^\circ$  with respect to the upper Pc ring in (a). (d)  $U = -0.5 \text{ V}$ ,  $I = 1 \text{ nA}$ ; at elevated negative bias voltage, parts of the single-decker appear lower than the cobalt surface.

to a molecule, approached towards the surface, and dragged across the molecule in constant-height mode (cf. Figure 4.5). This removes the upper Pc ring, which often adsorbs on the tip. The eight-lobe cross observed for intact  $\text{TbPc}_2$  transforms into a four-lobed cross twisted by  $45^\circ$ , and with lower profile. This four-lobed cross highly resembles single-decker Pcs adsorbed on metal surfaces [87, 85], where hybridisation with the substrate washes out the molecular eight-lobe  $\pi$  orbital; the leftovers can therefore be identified to be the lower Pc ring of  $\text{TbPc}_2$ . The twist by  $45^\circ$  with respect to the eight-lobed cross of the intact double-decker corroborates that the two Pc rings are staggered by  $45^\circ$ . Manipulation for decomplexation is performed for  $\text{TbPc}_2$  adsorbed on bare  $\text{Ir}(111)$  and on cobalt nanostructures, yielding the same result for  $\text{TbPc}_2$  in both cases.

### $\text{Pc}_1/\text{Co}/\text{Ir}(111)$

The single-decker Pc resulting from the decomplexation experiment is briefly discussed in this section.

On bare  $\text{Ir}(111)$ , the remaining single-decker Pc has an apparent height of  $\sim 100 \text{ pm}$ , while on cobalt islands it appears as a depression for elevated negative bias voltages (cf. Figure 4.6d). The latter observation is in agreement with investigations of single-decker  $\text{CoPc}$  molecules adsorbed on  $\text{Co}/\text{Ir}(111)$  whose ligands also appear as depressions for small negative bias voltages [88, Figure 3c].  $\text{CoPc}$  however shows a pronounced protrusion at the centre of the molecule, i.e. at the position of the cobalt ion. Single-decker  $\text{TbPc}_1$  molecules adsorbed on  $\text{Au}(111)$  [85] show a central depression or protrusion, depending on bias voltage. Here, the absence of any protrusion over the energy range

investigated hints towards the Tb ion being missing in the remaining Pcs observed after decomplexation. The precise configuration of the centre of the remaining Pc remains unclear; open bonds, bonding to the substrate, or formation of full phthalocyanine  $H_2Pc$  by saturation of the open bonds by itinerant hydrogen are possible. For a deeper investigation, co-deposition of  $H_2Pc$  would be needed for direct comparison. All remaining Pcs showed a depression in the centre, indicating that Tb is absent in all cases. Further attempts to move the lower Pc, or the double-decker as a whole, proved unsuccessful, corroborating the strong molecule–substrate interaction.

### 4.3.2 Analysis of molecular adsorption

In this section, the molecular adsorption is investigated in terms of orientations and symmetry reduction upon adsorption to determine the adsorption site and the strength of molecule–substrate interaction.

Other means to investigate molecule–substrate interaction include the study of molecular self-assembly, comparison of STS spectra to LDOS data of free molecules, or manipulation to move or desorb the molecule. Analysis of the symmetry of the adsorption of single molecules can provide information about the molecule–substrate interaction with very little prerequisites. In contrast, analysis from self-assembly experiments requires detailed knowledge about molecule–molecule interaction.

The set of observations available for the discussion of symmetry is the following: the stable conformation of  $TbPc_2$  on Co on Ir(111) shows a  $C_s$  mirror symmetry with the symmetry axis perpendicular to a close-packed row of Ir(111), and is found in three orientations (Figure 4.7a,b).

#### Molecular orientations

For molecules not too weakly interacting with the substrate, the number of orientations (of each molecular conformation) on a surface is determined by substrate and molecular symmetry. A  $C_n$  surface symmetry yields  $n$  orientations, unless a molecular symmetry makes some of these  $n$  orientations indistinguishable ( $C_n$  means identity after rotation by  $360^\circ/n$ ,  $C_{nv}$  additionally  $n$ -fold mirror symmetry). The latter can occur for instance in case of molecules with  $C_2$  symmetry on a  $C_{6v}$  surface: the number of orientations is reduced from six to three.

The surface of single-layer Co on Ir(111) has  $C_{6v}$  symmetry (Figure 4.7c). With the  $C_s$  symmetry observed for the  $TbPc_2$  molecule adsorbed on it, six distinct orientations should be found. The observation of only three orientations can only be explained by a reduction of the surface symmetry to  $C_{3v}$ .

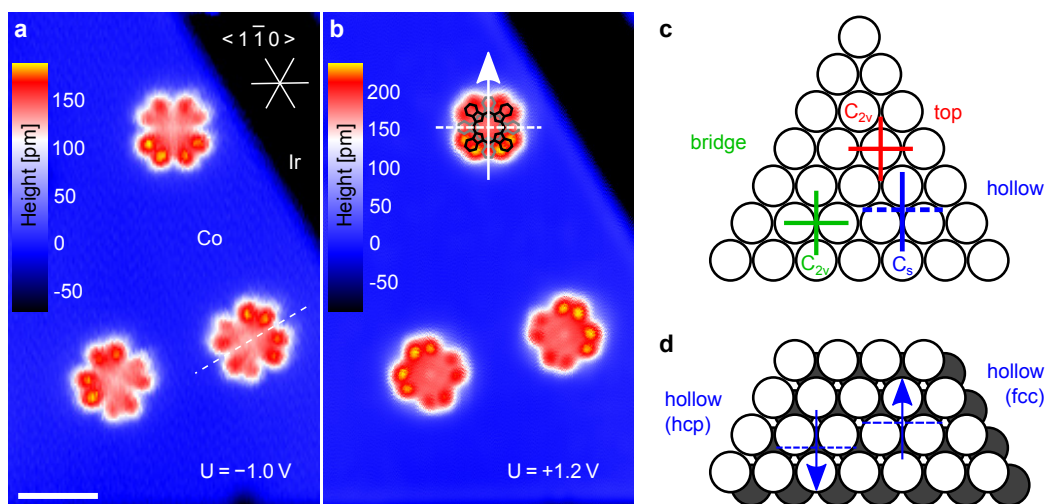


Figure 4.7: **Reduction of molecular symmetry on different adsorption sites.** (a,b)  $TbPc_2$  molecules on a Co island, with their symmetry axis of reflection perpendicular to a close-packed row of Ir(111). An island rim, parallel to a close-packed row, is visible in the top right corner of the image. (c) reduction of the  $D_{4d}$  symmetry of free  $TbPc_2$  on different high symmetry sites. Only the hollow-site position gives the observed symmetry. (d) When the first sub-surface layer (grey filled circles) is considered, two distinguishable hollow sites exist, either with or without a sub-surface atom beneath the hollow site. Each kind of hollow sites has  $C_{3v}$  symmetry and therefore yields three orientations.

To explain this symmetry, the first sub-surface layer (in this case the top layer of Ir) needs to be considered: its fcc or hcp stacking reduces the symmetry to  $C_{3v}$  (Figure 4.7d). Islands grown in an fcc or hcp stacking sequence with respect to the Ir substrate both provide a  $C_{3v}$  substrate symmetry, and are simply rotated by  $60^\circ$  with respect to each other. In fact, molecules adsorbed on rotated triangular islands, i.e. those pointing down rather than up, are found to be rotated by  $60^\circ$  as well, substantiating the argument. An influence of a sub-surface layer on the molecular adsorption is very unusual; at this point there is only one published example [89]. The influence of the sub-surface layer indicates a very strong molecule–substrate interaction of  $TbPc_2$  to the cobalt surface.

### Reduction of molecular symmetry

The reduction of molecular symmetry upon adsorption provides information about the adsorption site. The molecule can adsorb on different sites on the surface, where the adsorption site is defined to be the spot on the surface below the centre of the molecule. Different adsorption sites have different symmetry, e.g., full  $C_{6v}$  symmetry for a top site (on top of a surface atom) of an fcc(111) surface versus only  $C_{2v}$  symmetry for a bridge site (between two neighbouring surface atoms). Given a sufficiently strong interaction, the substrate reduces the symmetry of the adsorbed molecule depending on the adsorption site. If the molecular symmetry is reduced upon adsorption, the location is narrowed down to a number of adsorption sites, which are compatible with the observation.

$TbPc_2$  adsorbed on Co on Ir(111) has  $C_s$  mirror symmetry, in contrast to the  $D_{4d}$  symmetry of free  $TbPc_2$  molecules. Only adsorption sites with symmetries whose greatest common subset with the  $D_{4d}$  molecular symmetry is  $C_s$  cause that observed symmetry. With the full surface symmetry being  $C_{6v}$ , only sites with  $C_{3v}$  or  $C_s$  symmetry satisfy this condition. Top ( $C_{6v}$ ) and bridge site ( $C_{2v}$ ) do not reduce the molecular symmetry sufficiently (only to  $C_{2v}$ ), the hollow site ( $C_{3v}$ ) as well as all positions on straight lines between top and bridge, bridge and hollow, and hollow and top sites (all:  $C_s$ ) do. All other sites do not provide any symmetry and are therefore incompatible with the observation. With the mirror axis on  $TbPc_2$  being perpendicular to a close-packed row, positions between top and bridge are incompatible as well. Therefore, only hollow sites and positions on straight lines between hollow and bridge, or hollow and top sites are possible locations. Considering again a possible influence of the first sub-surface layer rather than the surface only, a top site adsorption would be possible too, as its symmetry reduces to  $C_{3v}$ . However, an influence of the sub-surface layer is rare, as pointed out

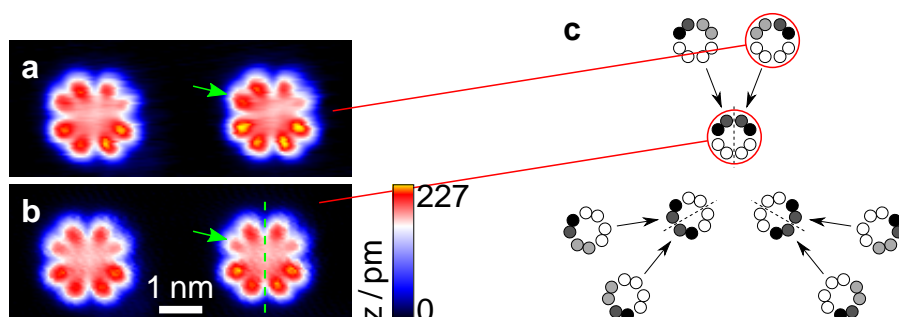


Figure 4.8: **Conformations of  $\text{TbPc}_2$  on Co on  $\text{Ir}(111)$ .** (a) Unstable conformation of  $\text{TbPc}_2$  on  $\text{Co}/\text{Ir}(111)$ . It switches by scanning with  $U_{bias} = -1.5 \text{ V}$  into the (b) stable conformation. The unstable conformation does not exhibit a symmetry axis, while the stable one is mirror symmetrical; the green dashed line indicates the axis of reflection. The most pronounced difference is the apparent height difference for the lobe marked by the green arrow,  $\Delta z \sim 30 \text{ pm}$ .  $U = -1.5 \text{ V}$ ,  $I = 100 \text{ pA}$ . (c) Schematic of the six orientations of the unstable conformation and their resultant stable conformations. Bright circles represent high lobes. The orientations of the conformations in (a) and (b) are marked by red circles.

above. A strong symmetry reduction as observed here, with the lowest lobes appearing 30 pm lower than the highest ones, is unlikely to be caused by a sub-surface layer. A top site adsorption is therefore considered very unlikely. The importance of the determination of the adsorption site becomes evident when considering that DFT calculations showed a preference for bridge site adsorption and therefore failed to reproduce the observed reduction to  $C_s$  symmetry.

### 4.3.3 Conformations

$\text{TbPc}_2$  adsorbed on cobalt islands on  $\text{Ir}(111)$  appears in two conformations. Only the one already described above is stable against tunnelling at elevated voltages  $U \sim \pm 1 \text{ V}$ , and is subject of detailed investigation in this chapter. The other conformation is briefly discussed in this section.

There are two distinct prevalent conformations of  $\text{TbPc}_2/\text{Co}/\text{Ir}(111)$  (Figure 4.8a,b), and a number of irregular appearances. The latter occur in particular for molecules very close to each other or to island rims or step edges; only undisturbed molecules take one of the prevalent forms. One of the two conformations (“stable”, Figure 4.8b) is the one already described above, the other one (“unstable”, Figure 4.8a) can easily be distinguished by its six

high and two lower appearing lobes. It is nearly identical in lateral size and apparent height, and similar in LDOS. It switches into the stable conformation at elevated bias voltages of around  $U \sim \pm 1$  V. The two lower lobes remain being low lobes in the switched molecule. There are six orientations for the unstable conformation and only three for the stable one. Two orientations of the unstable conformation always switch into one orientation of the stable conformation (Figure 4.8c). The unstable conformation switches at bias voltages corresponding to HOMO or LUMO. The switching process is therefore likely to be triggered by tunnelling into molecular orbitals, or by the elevated bias voltage. A slow high-resolution image or a high-quality point spectrum induce a switch (implying that the switching probability per electron is about  $10^{-13}$  to  $10^{-11}$ ). A detailed investigation of this conformation, in particular its molecular orbitals, is therefore not possible. The process is generally unidirectional; only once an unstable conformation molecule switched back into the stable conformation, telling that the switching is not destructive. A manipulation scheme for this back-switching mechanism was not found. The stable conformation was stable throughout the experiments. Both conformations are present after both room temperature and low temperature ( $T \sim 100$  K) preparation. Their proportion ( $48 \pm 5\%$  stable) does not change significantly with preparation temperature. Given these observations, a minor geometric deformation seems the most likely reason for the small difference of the two conformations. The stable conformation investigated here exhibits the same geometrical deformation observed on other fcc(111) surfaces [47, Figure 1a]. The subtle height differences between conformations emphasise the importance of high-quality STM images for pre-characterisation in, e.g., XMCD experiments.

## 4.4 Spin-resolved investigation

This section presents the spin-resolved investigation of TbPc<sub>2</sub> adsorbed on Co/Ir(111). Cobalt islands and TbPc<sub>2</sub> molecules exhibit a number of spin-polarised features (section 4.4.1). To disentangle effects and artefacts, the experimental scheme is modified to rule out tip height effects (section 4.4.2). Quantitative analysis (section 4.4.4) settles that the LUMO is spin-split.

### 4.4.1 Constant-current mode measurements

Before seeking for spin-polarised features on molecules, the spin sensitivity of the tip is established by probing reference cobalt islands (compare section 4.1). An iron coated tungsten tip is used. The iron film acts as a soft

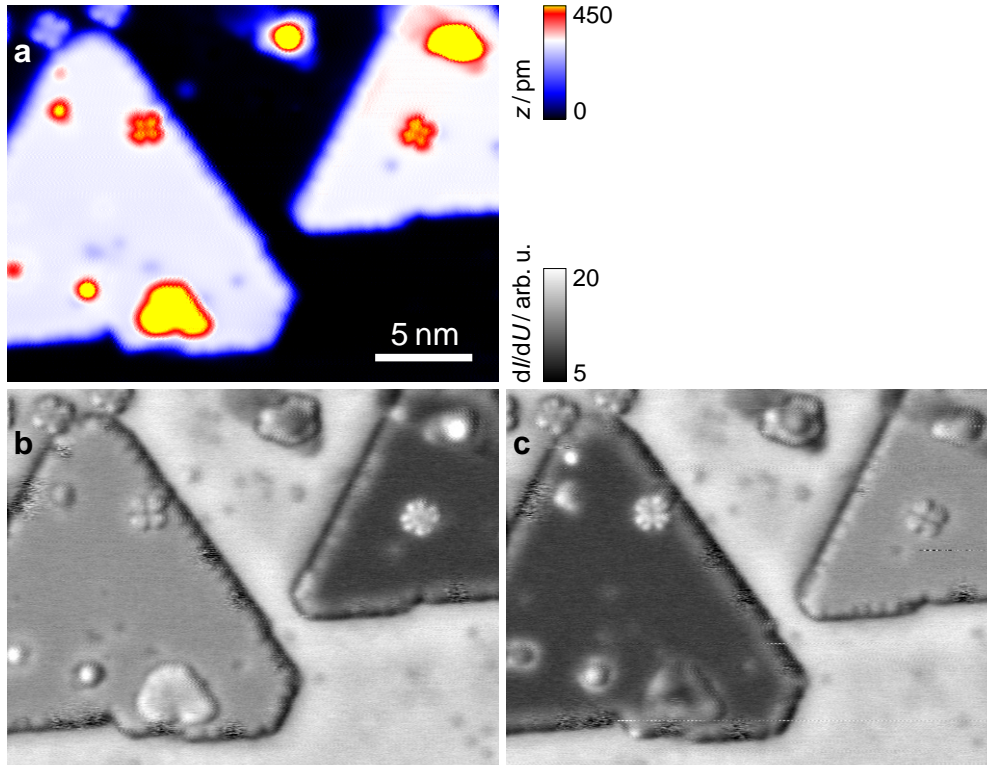


Figure 4.9: **Spin-resolved TbPc<sub>2</sub> on Co/Ir(111)**. (a) topograph showing two cobalt islands with one TbPc<sub>2</sub> molecule adsorbed on top of each. Both islands and molecules appear identical.  $U = -0.5$  V,  $I = 1$  nA,  $B = 1$  T, Fe coated W tip. (b) map of differential conductance, acquired simultaneously to (a). The different brightness of the islands indicates different spin-resolved differential conductance, and reveals that the islands are oppositely magnetised.  $U_{\text{mod}} = 20$  mV,  $f_{\text{mod}} = 6777$  Hz. The TbPc<sub>2</sub> molecule on the bright island shows four lobes, whereas the one on the dark island shows eight and is brighter. (c) same as (b), with the external magnetic field direction reversed;  $B = -1$  T. The contrast on the cobalt islands reverses with respect to (b), as well as the brightness and the structural contrast of the molecules.

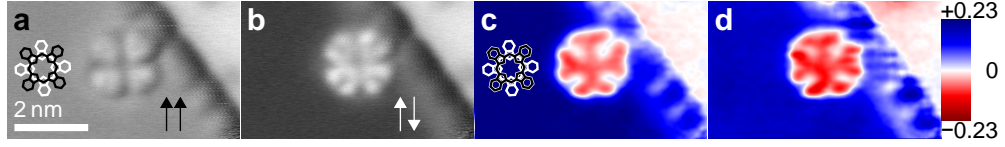


Figure 4.10: **Spin asymmetry and effective spin polarisation of  $\text{TbPc}_2$**  at  $U = -0.5$  V. (a,b) High resolution maps of differential conductance of the  $\text{TbPc}_2$  molecule on the left-hand-side island in Figure 4.9b,c. The four/eight lobes follow the upper (black) Pc ring of the structure model of  $\text{TbPc}_2$ . (c) Spin asymmetry map calculated from (a,b). The cross follows the lower Pc ring of  $\text{TbPc}_2$ . (d) Effective spin polarisation map calculated from (a,b) and corrected by tip height. Artefacts appear on the Ir substrate at the upper edge of the image, on the island rim, and on the right-hand side of the molecule. Data recorded by Yingshuang Fu.

magnet, and its magnetisation rotates with an external magnetic field. The cobalt islands are hard magnets and keep their magnetisation, as they exhibit high magnetic coercivity [76]. As the cobalt island magnetisation is parallel to the surface normal, out-of-plane spin sensitivity is desired, and the tip magnetisation is therefore aligned by an out-of-plane magnetic field of  $B = \pm 1$  T. Figure 4.9a shows two oppositely magnetised cobalt islands with one  $\text{TbPc}_2$  molecule adsorbed on top of each. The molecules are rotated horizontally by  $120^\circ$  with respect to each other. While the topograph gives no visible spin contrast, the simultaneously recorded map of differential conductance does: the left-hand-side island clearly shows higher differential conductance and therefore appears brighter than the one on the right (Figure 4.9b). Also, the  $\text{TbPc}_2$  molecules appear differently. The molecule on the brighter island shows only four lobes, while the other one shows eight. Additionally, the molecule on the darker island appears slightly brighter. To clearly establish that the contrast is of magnetic origin, the magnetic field direction is reversed to rotate the magnetisation direction and thereby the spin sensitivity of the tip, and the same surface area is scanned again. Figure 4.9c shows that in fact all contrasts observed before reverse; the bright island now appears darker, and the molecules have changed their appearance from four to eight lobes and vice versa.

Figure 4.10 shows a high-resolution map of the molecule of the left-hand-side island. To rule out scan direction artefacts, images of the same molecule, measured in different spin channels, are compared. While the different number of lobes is clearly discernible, the different intensity is hard to perceive by looking at images side-by-side. To get an idea about the magnetic contrast contribution, the spin asymmetry (cf. chapter 1.6, equation 1.12) is

computed. The result is shown in Figure 4.10c. The spin asymmetry on the iridium substrate is zero because it is non-magnetic. The cobalt island exhibits a large and uniform spin asymmetry of about +22%. The rim of the island shows a spatially inhomogeneous spin asymmetry with a width of about 1 nm. The spin asymmetry of the molecule has opposite sign. The geometric difference observed above manifests in a pronounced cross and eight lobes of approximately equally high ( $\sim -20\%$ ) spin asymmetry. Note that this cross is rotated by  $45^\circ$  with respect to the upper Pc ring. Correcting the constant-current  $dI/dU$  maps for tip height differences is possible by multiplication with an exponential  $e^{\kappa z}$  containing the height  $z$  from the respective topographs (chapter 1.6.1). The resulting map of effective spin polarisation (Figure 4.10d) is similar to the spin asymmetry map. The magnitude of the spin contrast is larger for the molecule but weaker for the cobalt substrate, which appears about 3 pm higher in the topograph of the parallel spin channel due to the spin-polarised contribution from the pronounced  $-250$  mV feature. Also, the image shows more distortions due to the introduction of additional noisy data. Especially, the non-magnetic iridium surface shows artefact spin polarisation due to low-frequency  $z$  noise of the topographs.

### Magnetic field dependence

To study the influence of the external magnetic field, a series of images at different magnetic field values is taken (Figure 4.11). In Figure 4.11a, taken at  $B = +1.0$  T, the  $dI/dU$  map shows the magnetic contrast presented above (Figure 4.10): oppositely magnetised cobalt islands show different differential conductance, and the TbPc<sub>2</sub> molecule adsorbed on the island with lower differential conductance shows eight lobes, while the one adsorbed on the cobalt island with higher differential conductance shows only four. Reducing the magnetic field to  $B = +0.1$  T (Figure 4.11b) reduces the magnetic contrast between the oppositely magnetised cobalt islands and resolves eight lobes on both molecules. At zero magnetic field (Figure 4.11c), the spin contrast of islands and molecules is gone, and both molecules show weakly resolved eight lobes. Ramping the magnetic field to negative field values ( $B = -0.3$  T in Figure 4.11d) inverts the magnetic contrast: the left-hand-side island is brighter now, and the molecule adsorbed on it shows only four lobes. Reducing the magnetic field to  $B = -0.1$  T (Figure 4.11e) again reduces magnetic contrast on cobalt and molecules. In absence of an external magnetic field (Figure 4.11f) the molecules do not show magnetic contrast, while a faint contrast remains between the cobalt islands. Ramping the magnetic field to  $B = -1.0$  T (Figure 4.11g) restores full contrast, a bit stronger than at  $-0.3$  T.

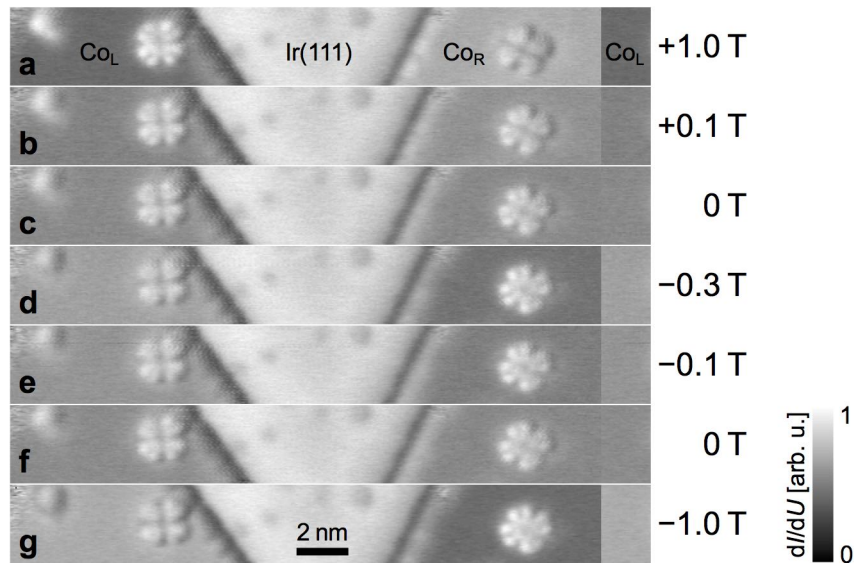


Figure 4.11: **Magnetic field dependence of  $dI/dU$  maps.** The images show spin-resolved  $dI/dU$  maps of the same area as in Figure 4.10 at different magnetic field strengths. At the far right-hand side, a small section of the left-hand side cobalt island is shown to clearly discern its spin contrast. All maps are given with the same colour scale. The images are taken consecutively, and the field is ramped directly from value to value. The cobalt islands and the  $TbPc_2$  molecules show spin contrast in different intensity and sign depending on the magnetic field. The  $dI/dU$  signal intensity on non-magnetic iridium does not change, as expected.

Fe coated W tip.  $B$  normal to sample plane.  $U = -0.5$  V,  $I = 1$  nA,  $f_{\text{mod}} = 6777$  Hz,  $U_{\text{mod}} = 20$  mV<sub>rms</sub>.

To summarise, the intensity of the magnetic contrast of cobalt islands and  $\text{TbPc}_2$  molecules depends monotonically on the strength of the applied external magnetic field, and the sign of the contrast on the sign of the field. The molecular spin contrast follows the sign and strength of the cobalt island spin contrast. Cobalt islands and molecules thus retain their magnetisation throughout the measurement, while the magnetisation and thus spin sensitivity of the tip change with the field. The faint remaining magnetic contrast at zero field (Figure 4.11f) indicates inherent hysteresis of the tip magnetisation; it shows magnetic remanence at zero field. The small difference in contrast between the maps taken at  $B = -0.3$  and  $-1.0$  T means that the tip magnetisation is nearly fully aligned at  $-0.3$  T already, giving almost the same out-of-plane spin sensitivity. These observations agree well with previous experiments with Fe coated W tips [31]. Their magnetisation typically fully aligns with an external out-of-plane field at about  $\pm 0.5$  Tesla. At zero field, their magnetisation does not disappear, but rotates to an in-plane magnetisation direction. Here, the remaining z component gives the magnetic contrast, while neither cobalt island nor molecules display any new features related to the in-plane magnetic sensitivity.

### Energy-dependent spin asymmetry maps

After the first successful observation of spin contrast on  $\text{TbPc}_2$ , the next step is an investigation of a larger voltage range, including the frontier orbitals. As it proves difficult to subtract images of molecules rotated with respect to each other (cf. Figure 4.9b), and the window size is too large to provide high resolution within a reasonable time frame, the scheme is modified. A smaller surface area is chosen, with two molecules on the same cobalt island (Figure 4.12a). They have different orientations to rule out tip geometry and scan direction artefacts. Without a second, oppositely magnetised cobalt island in the image, spin contrast within a single measurement is not feasible. For spin contrast, each image is recorded for both field directions, probing opposite spin channels.<sup>5</sup> The cobalt island maintains its magnetisation direction throughout the experiment. The integrated spin polarisation can be inferred from the differences of topographs. These suffer from low-frequency noise below 1 Hz and from hydrogen contaminations. Even after careful flattening, artefact differences from noise are typically as high (see Figure 4.12g)

---

<sup>5</sup>In general, this approach provides advantages. Unnoticed differences between different molecules, such as different adsorption sites, adsorption environments or nearby adsorbates, as well as distortions from a canted tip apex vanish in the subtraction. Also, a single suitable molecule is sufficient. Disadvantages are the need for an expensive magnet in the STM setup, and long ramping times of the magnet.

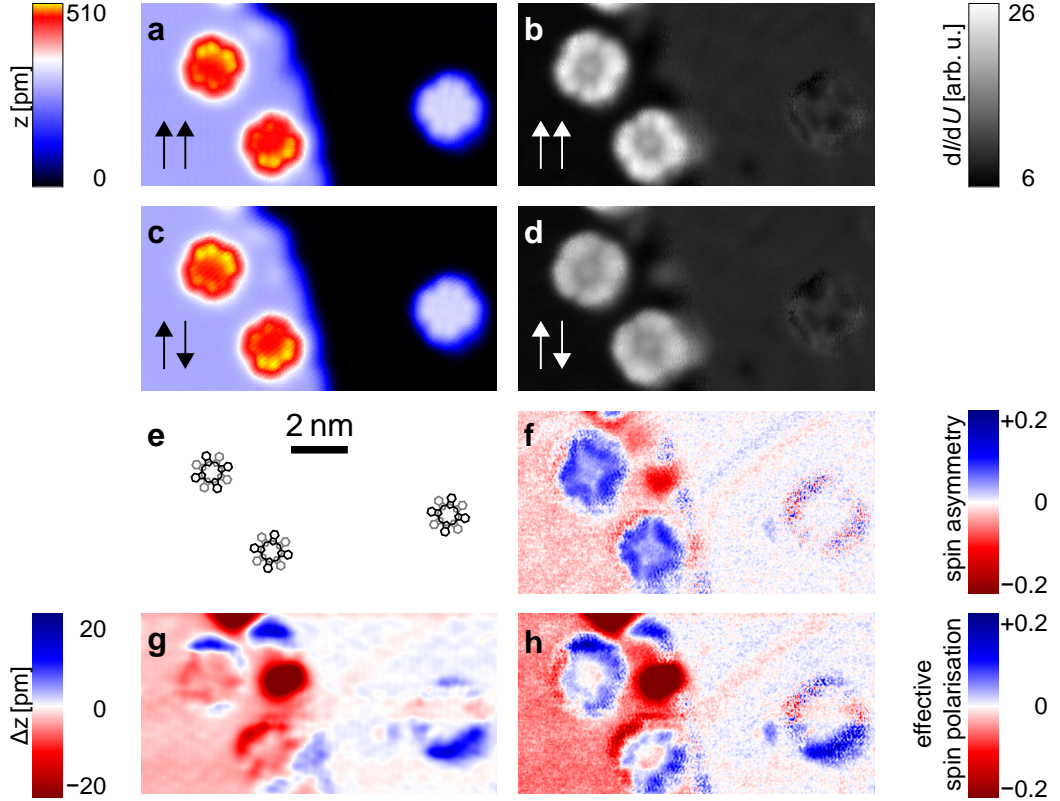


Figure 4.12: **Spin-resolved topographs and maps.** (a) Topograph of two  $TbPc_2$  molecules adsorbed on Co and one on bare iridium. The tip's magnetisation is aligned parallel with the cobalt island magnetisation. All images:  $U = +1.3$  V,  $I = 1$  nA,  $B = \pm 1$  T, Fe coated W tip. (b) Simultaneously recorded map of differential conductance.  $U_{\text{mod}} = 50$  mV<sub>rms</sub>,  $f_{\text{mod}} = 6777$  Hz (c,d) As (a,b), with the magnetic field direction reversed to align tip and sample magnetisation antiparallel. (e) Structure models of  $TbPc_2$  molecules in (a,c). (f) Spin asymmetry, calculated from maps of differential conductance (b,d). Both iridium and the molecule on iridium disappear as they are not magnetic. The cobalt island shows a negative spin asymmetry, both molecules on cobalt a strong positive spin asymmetry, with higher magnitude over the lobes than over the centre. (g) Difference of topographs (a) and (c), related to the integrated spin polarisation. Here, dominated by artefacts and noise (see text). (h) Effective spin polarisation, calculated from maps of differential conductance with corrections from topographs. This introduces artefacts from (g); the map is barely usable. Data recorded by Yingshuang Fu.

as the spin polarisation of  $\text{TbPc}_2$ , which does not exceed 10% for most energies. However, the feedback loop follows the low-frequency noise well and keeps current and tip-sample distance constant. The time constant of the lock-in amplifier further averages the signal, leading to smooth  $dI/dU$  maps.

Hence,  $dI/dU$  spin asymmetry maps (Figure 4.13) are analysed in the following paragraphs. The bare iridium substrate and the  $\text{TbPc}_2$  molecule adsorbed on it show no spin asymmetry throughout the investigated energy range, whereas both the cobalt island and the two adsorbed molecules show a number of features with spin contrast.

The bare iridium substrate shows no spin asymmetry because it is not magnetic. The  $\text{TbPc}_2$  molecule adsorbed on iridium exhibits no spin asymmetry either. This behaviour matches the expectations since in absence of a ferromagnetic support, both tip and magnetic moment of  $\text{TbPc}_2$  align with the field. In principle, the SMM  $\text{TbPc}_2$  might maintain its magnetisation direction for a short period of time after reversal of the magnetic field, but at the setup temperature this period of time is likely less than a second (cf. chapter 2.2.1), making the molecule's magnetisation relax and align with the field before the first image is recorded.

The cobalt island shows an oscillatory behaviour of high (about 20%) spin asymmetry for occupied states, reflecting the spin-polarised LDOS presented in the point spectra in Figure 4.1, no spin asymmetry for low-energy unoccupied states, and weakly (up to  $-2\%$ ) negative spin asymmetry above  $U = +1.0$  V. Cobalt shows negative spin asymmetry at  $U = -0.2$  V, reflecting the spin asymmetry of its pronounced  $-0.25$  V peak. For higher binding energy, the observed spin asymmetry then changes sign three times, below  $-0.2$  V,  $-0.8$  V, and  $-1.7$  V (cf. Figure 4.1a). Cobalt thus shows positive spin asymmetry from  $-2.0$  to  $-1.8$  V, negative from  $-1.7$  to  $0.9$ , positive from  $-0.8$  to  $-0.3$ , and negative for  $-0.2$  V.

The two molecules adsorbed on the cobalt island always show identical spin asymmetry distributions for a given bias voltage, rotated by  $120^\circ$  following their different orientation. The spin asymmetry does not follow, or reversely follow, the cobalt spin asymmetry, but exhibits individual magnetic behaviour. At  $U = -0.3$  V, the cobalt island reveals a spin-polarised edge state of about 1 nm width. Still both molecules show identical spatial distributions of spin asymmetry without a change above the edge state. Throughout the HOMO-LUMO gap ( $U = -0.6$  to  $+0.7$  V), the spin asymmetry changes only slightly and reproduces the observation at  $U = -0.5$  V presented above (Figure 4.10). For both molecules, the symmetry axis visible in topographs is the symmetry axis of the spin asymmetry maps as well. For  $U = +0.8$  to  $U = +1.0$  V, a pronounced (up to about  $-20\%$ ) negative spin asymmetry is visible on the ligands. Maps at  $U = +1.2$  to  $+1.5$  V show

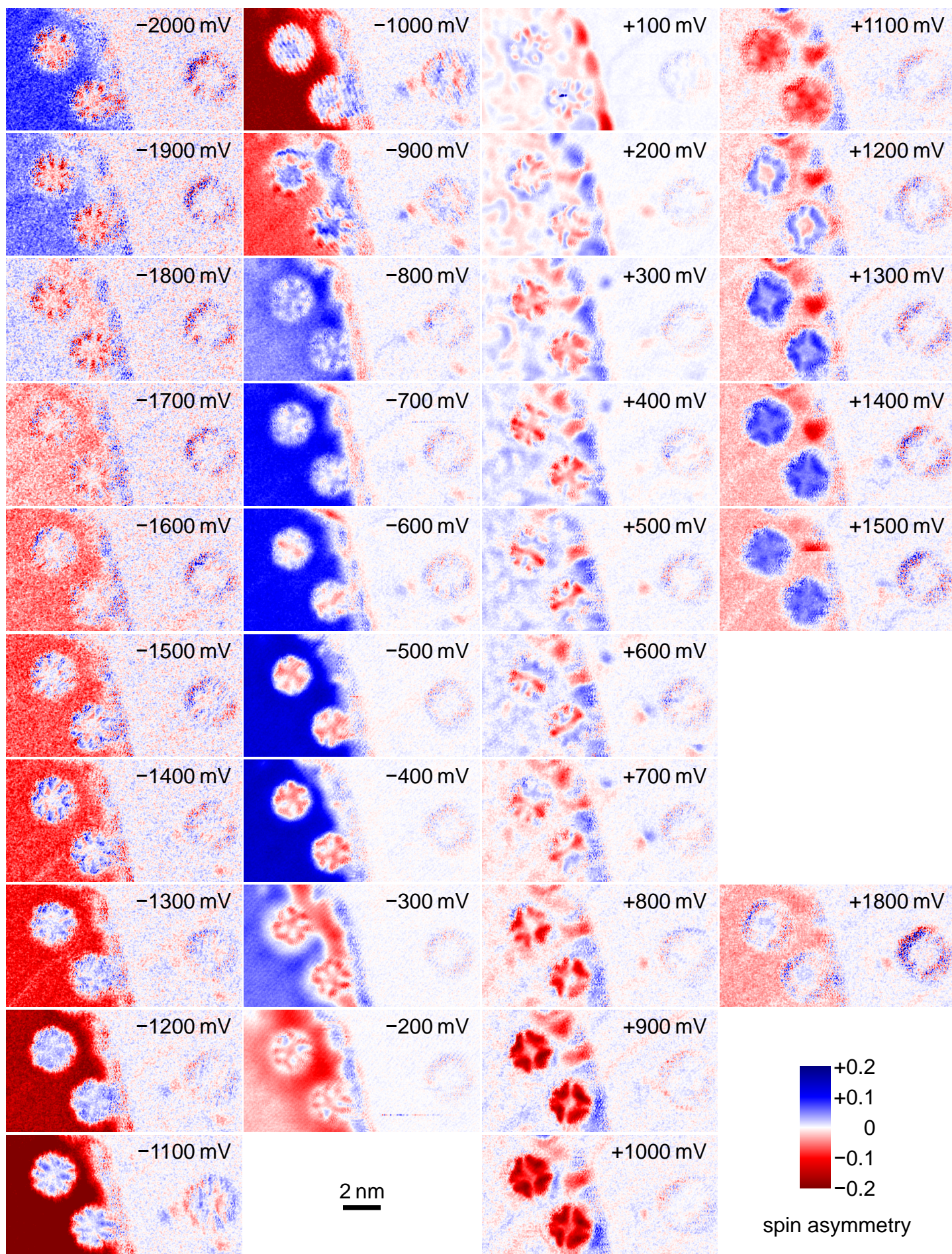


Figure 4.13: **Energy dependent spin asymmetry maps of TbPc<sub>2</sub>/Co/Ir(111)**, presenting the same surface area as Figure 4.12. Spin asymmetry maps are calculated from maps of differential conductance, recorded in constant-current mode (analogue to Figure 4.12f). Blue colour denotes a positive spin asymmetry, i.e. a stronger signal for parallel alignment of tip and sample magnetisation, red a negative spin asymmetry. Data recorded by Yingshuang Fu.

identical spatial distributions of spin asymmetry, but with opposite sign. The spin asymmetry map taken at  $U = +1.1$  V – between these opposite effects – shows lower positive spin asymmetry on the lobes, but negative spin asymmetry over the centre and around the lobes. At +1.8 V, TbPc<sub>2</sub> has no spin asymmetry. For occupied states, lower spin asymmetries of up to 10% are observed. For  $-2.0$  to  $-1.7$  V, the eight lobes of the  $\pi$ -like orbitals show negative spin asymmetry, for  $-1.5$  to  $-1.4$  V their spin asymmetry reverses to positive. At  $-2.0$  and  $-1.9$  V, a weak negative spin asymmetry over the centre accompanies the asymmetry of the lobes. From  $-1.4$  to  $-1.0$  V, the spin asymmetry is weak (up to 5%) and positive all across the molecule, showing eight lobes for  $-1.3$  and  $-1.1$  V, and faintly resembling a reversed  $-0.5$  V map at  $-1.2$  V. At  $-0.9$  V, the eight lobes have negative spin asymmetry while the centre shows a uniform positive spin asymmetry. The map at  $-0.8$  V resembles a reversed  $-0.5$  V map, with the central cross not well resolved, and the map at  $-0.7$  V appears like a mixture of the former two, with positive spin asymmetry dominating.

Additionally, the island rim shows a number of effects. The spin asymmetry visible for the full island rim at  $-0.2$  and  $+0.1$  V might or might not be real, as sub-nanometre misplacement of relative lateral positioning of the spin-resolved  $dI/dU$  maps gives an artefact asymmetry when the difference is computed. The maps at  $U = +0.9$  to  $+1.5$  V show a spot on the island rim right next to the molecules, with negative spin asymmetry. In the map at  $+1.5$  V its origin is revealed: the spot ends with a scan line, indicating that it stems from an adsorbate being desorbed (without changing the tip). The cobalt island shows patterns at low positive bias voltages, reminiscent of scattering patterns. These can either be real spin-polarised scattering patterns around molecules and persistent adsorbates, or again an artefact from smaller desorbing or moving adsorbates: in this case, adsorbates changing position between recordings of the two spin channels would produce two different non-spin-polarised scattering patterns, generating an artefact pattern when taking the difference of those spin channels.

Spin asymmetries calculated from uncorrected  $dI/dU$  maps suffer from

small systematic errors if the tip heights for different spin channels differ (see section 1.6.1). Here, constant-current mode is used, which does not ensure equal tip heights in both spin channels. Such a difference in tip height is expected here for example for bias voltages above +1.0 V. The higher LDOS in the spin channel with antiparallel alignment of tip and sample magnetisation direction between  $U = +0.8$  and 1.0 V causes higher conductance in this spin channel. To yield equal tunnelling currents in both spin channels, the feedback loop retracts the tip further when probing this spin channel in order to compensate for the higher conductance. A hypothetical unpolarised feature at the given bias voltage then appears weaker in this spin channel, and stronger in the opposite spin channel. The effect therefore produces an artefact spin asymmetry opposite to the spin asymmetry observed at lower bias. In this example, a reversed (apparent) spin asymmetry above +1.0 V is expected. This matches the experimental observation at  $U = +1.2$  to +1.5 V. A correction of tip height differences is required to determine the real effective spin polarisation at  $U = +1.2$  to +1.5 V. The tip height is available from the topographs. Compensation of the tip height difference (assuming a parameter for the exponential decay of wave functions into vacuum) is, in principle, possible. For the given data set, the topograph noise is too high (see Figure 4.12g,h), and it introduces artefacts of the same order as the observed spin asymmetry itself; compensated spin asymmetry maps do not yield meaningful results here.

#### 4.4.2 Constant-height mode measurements

A different scheme is used to obtain a map of effective spin polarisation revealing the correct sign and spatial distribution of the LUMO spin polarisation at  $U = +1.3$  V. To rule out tip stabilisation artefacts, the tip is stabilised over a non-magnetic surface area, so its height does not depend on the spin channel (cf. chapter 1.6.1). Here, the tip is stabilised over non-magnetic iridium, the feedback loop is opened, the tip is retracted by  $z = 450$  pm to allow for scanning over the higher molecule, and an image is scanned with the tip kept in constant height over the molecule. To reduce effects from  $z$  noise, the feedback loop is slowed down before opening, thereby averaging over  $z$  noise. Figure 4.14a presents a topograph of the chosen surface area, with a narrow strip of iridium at the top, as the acquisition software starts the image and thus stabilises the tip on the top centre position of the image. The  $TbPc_2$  molecule resides on a cobalt island. The constant-height current and  $dI/dU$  maps (Figure 4.14b) only show the molecule and a faint signal from the cobalt surface. The cobalt surface is about 200 pm farther from the tip than the molecule, and the iridium surface is  $z \sim 450$  pm farther. Since

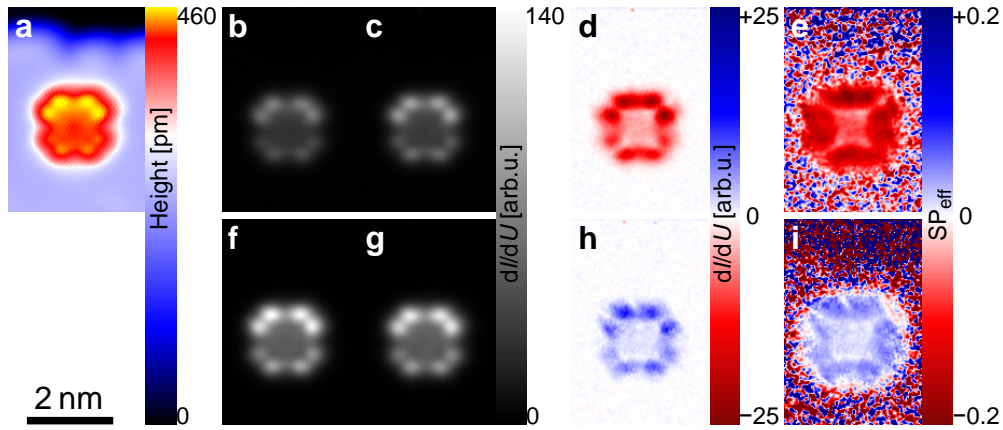


Figure 4.14: **Spin-resolved  $dI/dU$  maps of the LUMO.** (a) Topograph of a  $\text{TbPc}_2$  molecule (red to yellow) adsorbed on Co (blue) on Ir(111) (black).  $U = +1.0$  V,  $I = 1$  nA, Fe coated W tip. (b,c) spin-resolved  $dI/dU$  maps taken in constant-height mode, with (b) parallel and (c) antiparallel alignment of tip and sample magnetisation direction.  $U = +1.0$  V,  $I_{\text{stab}} = 1$  nA,  $\Delta z_{\text{stab}} = -4.5 \text{ \AA}$ ,  $f_{\text{mod}} = 6777$  Hz,  $U_{\text{mod}} = 50 \text{ mV}_{\text{rms}}$ ,  $B = \pm 1$  T. (d) difference of (b) and (c). (e) spin asymmetry from (b,c). The surrounding of the molecule appears garbled as the signal is close to zero (due to the larger tip-sample distance) and computation of spin asymmetry implies division by these small noisy numbers. (f-i) as (b-e), for  $U = +1.3$  V.

the tunnelling current decreases by a factor of about 10 for every 100 pm tip-sample distance, signals from cobalt and iridium are close to and below the noise level, respectively. The  $TbPc_2$  molecule shows eight well resolved lobes with the mirror symmetry observed before, detailing the LUMO  $\pi$ -type orbital. The desired information, i.e. the sign of the spin asymmetry and the spatial distribution of spin-polarised orbital(s), is best visualised in  $dI/dU$  difference maps. The  $dI/dU$  spin difference map at  $U = +1.0$  V (Figure 4.14d) shows eight well resolved lobes with the mirror symmetry observed before, very similar to the spatial distributions of the  $dI/dU$  maps of both spin channels. This indicates that the spin-polarised orbital is identical with the orbital imaged at this energy, the LUMO. The  $dI/dU$  spin difference map at  $U = +1.3$  V (Figure 4.14h) shows the very same spatial distribution as before, but with the sign reversed. This clearly and unambiguously shows that one orbital, the LUMO, is spin-split into a negative spin polarisation at lower energy and a positive spin polarisation at higher energy.

Normalising the spin difference maps (d) by dividing by the sum of the spin channel  $dI/dU$  maps (b+c) yields the spin asymmetry (Figure 4.14e,i). Since a compensation for tip height is not necessary due to the chosen tip stabilisation scheme, the spin asymmetry is identical to the effective spin polarisation here. The spin asymmetry maps show spin polarisation with the same sign as above, but higher magnitude for  $U = +1.0$  V ( $\sim 15\%$ ) than for  $U = +1.3$  V ( $\sim 5\%$ ). Eight lobes can hardly be distinguished, they connect to a squarish ring of nearly constant intensity, slightly reduced over the nodal planes between the pairs of lobes over isoindole groups, similar to the result obtained from constant-current data (cf. Figure 4.13). The spin polarisation over the centre of the molecule is significantly reduced compared to the lobes at both energies. The garbled structure around the molecule does not reflect any physical effect, it is an artefact of the signal being lower than noise due to large tip-sample distance over the metal surface. The constant spin asymmetry over the lobes means that there is little non-spin-polarised contribution to the tunnelling current at these positions (see chapter 1.6.2), the LUMO  $\pi$ -type orbital dominates the signal. Over the molecular centre however, the LUMO orbital gives a much lower contribution, the non-spin-polarised contribution is more significant, resulting in a lower spin polarisation.

### 4.4.3 Occupied states

Varying the bias voltage for the molecules presented in Figure 4.9 shows spin asymmetry on the HOMO at  $U = -0.8$  V, whereas Figure 4.13 clearly shows opposite spin asymmetry at the very same tunnelling and field conditions ( $U = -0.8$  V,  $I = 1$  nA,  $B = \pm 1$  T). For  $U < -0.9$  V both data sets agree,

showing negative spin asymmetry with eight-lobe spatial distribution first, and reversed positive polarisation for higher binding energy. Point spectroscopy data are similarly unreliable.

While the positive bias side reproducibly shows identical results both in point spectra and  $dI/dU$  maps, the negative bias side features are strongly tip dependent, giving spin polarisation on  $\text{TbPc}_2$  but with different magnitude and energy position from tip to tip. These observations match the findings of Ukraintsev [22], who derives a stronger tip LDOS influence for the negative bias side (cf. chapter 1.6.1).

Also, as the spin asymmetry is weaker than the spin asymmetry of the LUMO by a factor of about three to four, features are harder to nail down, especially as both the HOMO–LUMO gap feature and the eight-lobed HOMO feature change sign, making it necessary to rule out tip stabilisation artefacts by using an appropriate scheme. While no conclusion can be drawn regarding higher binding energy states, the first spin asymmetry observed for occupied states after the gap feature is always negative. The data do not show whether this orbital is negatively spin-polarised only or spin-split into a negative and a positive component.

#### 4.4.4 Spin-resolved point spectroscopy

The spin asymmetry maps from constant-current mode  $dI/dU$  maps do not tell whether the observed spin asymmetry on the LUMO shows a spin splitting or a spin asymmetry into one spin channel only. Spin-resolved point spectroscopy reveals the spin-resolved local density of states of the LUMO and returns a quantitative measure for the LUMO spin splitting and the occupation of both spin channels. An appropriate choice of tip stabilisation parameters rules out tip stabilisation height artefacts.

For spin-resolved point spectroscopy, the tip is stabilised at  $U = +2.0$  V because the integrated spin asymmetry over  $\text{TbPc}_2$  vanishes at this bias voltage, resulting in equal tip stabilisation height for both spin channels. As above, the spin channels are probed by aligning the magnetisation of the iron coated tungsten tip with the external magnetic field. Figure 4.15 presents normalised  $dI/dU$  point spectra of molecular lobes and centre. The spectrum taken with antiparallel alignment of tip and sample magnetisation reveals a wide peak with two local maxima at +1.0 V and +1.3 V. The spectrum taken with parallel alignment shows a wide peak as well, starting at about 0.1 eV higher energy, and having only one peak. The antiparallel SP-LDOS is higher than the parallel SP-LDOS from +0.7 to +1.1 V and lower from +1.1 to +1.7 V. At lower and higher energies, the spin difference is nearly zero. This is even more clearly visible in the difference of the spin channels

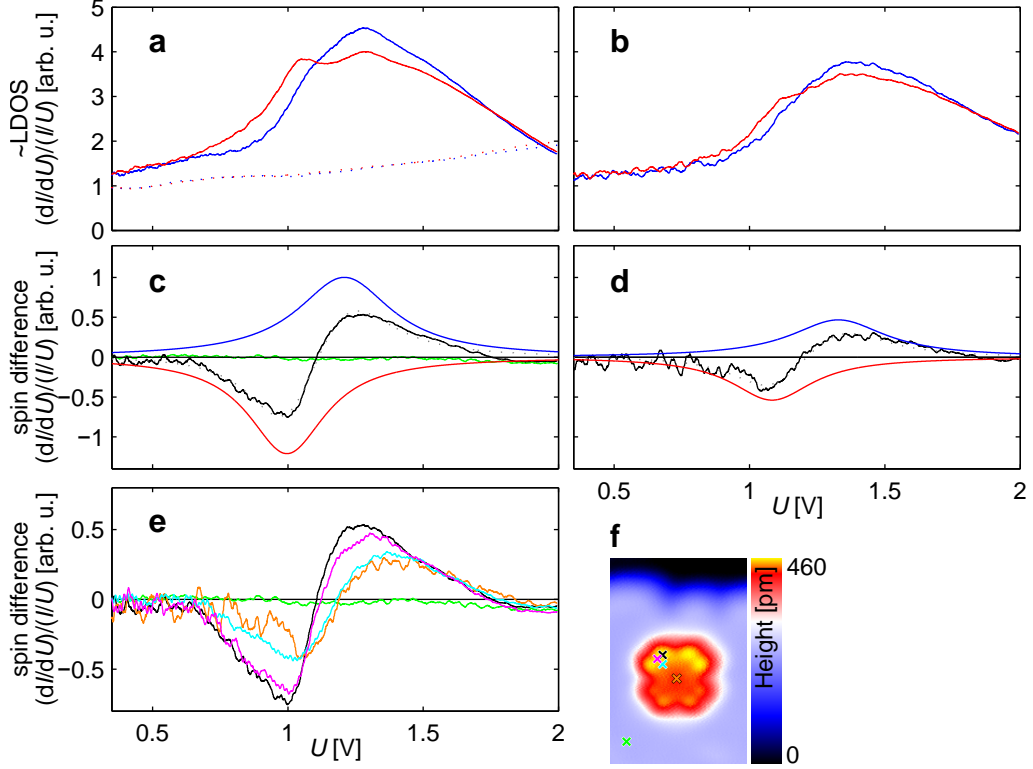


Figure 4.15: **Spin-resolved point spectra of the LUMO.** (a) spin-resolved  $dI/dU$  point spectra, normalised by dividing by  $(I/U)$  to better approximate the LDOS, taken above the lobes. Red: antiparallel alignment of tip and sample magnetisation direction. Blue: parallel. Spectra are averaged over all eight lobes. Dashed lines: Co surface for reference. (b) as (a), taken above the molecular centre. (c) difference of  $dI/dU$  spectra plotted in (a), revealing sign and LDOS of the spin difference (solid black curve), fit (dashed grey) using two Lorentzian profiles (smooth blue, red curves). Green: spin difference for cobalt, computed from spectra in (a). (d) as (c), for molecular centre. (e) spin difference for point spectra taken above several locations, as marked in (f). Black curve: lobes. Magenta: between lobes. Cyan: centred over isoindole group. Orange: centre. Green: cobalt surface. (f) Topograph of  $TbPc_2$ , with marked positions of point spectra presented in (e).  $U = +1.0\text{ V}$ ,  $I = 1\text{ nA}$ . All spectra:  $U_{\text{stab}} = +2.0\text{ V}$ ,  $I_{\text{stab}} = 1\text{ nA}$ ,  $f_{\text{mod}} = 6777\text{ Hz}$ ,  $U_{\text{mod}} = 10\text{ mV}_{\text{rms}}$ ,  $B = \pm 1\text{ T}$ .

plotted in Figure 4.15c. The spin difference gives a sinusoidal curve with two extrema at about +1.0 and +1.3 V. This clearly reveals a spin splitting into an antiparallel component at lower energy and a parallel component at higher energy. To quantitatively determine the magnitude of the spin splitting,  $dI/dU$  point spectra are normalised by dividing by  $(I/U)$ , which provides a good approximation to the local density of states according to Feenstra *et al.* [23].<sup>6</sup>

To quantify the magnitude of the spin splitting, the energy positions of antiparallel and parallel component are determined by fitting two Lorentzian profiles to the spin difference. The peaks are much wider than thermal broadening (2 mV) and lock-in broadening (10 mV<sub>rms</sub>), so using a convoluted fit function is unnecessary, and a simple Lorentzian sufficient. The resulting two Lorentzian peaks sit at 0.996 V and 1.209 V and are 348 mV and 425 mV wide, respectively. The energy difference gives the spin splitting  $U = (210 \pm 20)$  mV. Despite the different width, the areas of the two peaks are almost equal (0.662 vs. 0.668 (Volt)), which means that the number of states in antiparallel and parallel components equal. This clearly indicates that the LUMO is simply spin split into two spin components without any additional spin asymmetry.<sup>7</sup> The magnitude of the spin splitting indicates that it is caused by exchange coupling or direct coupling purely from hybridisation. Zeeman energies for the ligand spin and the terbium ion with  $J = 6$  are significantly lower.

The spin asymmetry of the cobalt island is below  $(2 \pm 1)\%$  for  $U = 0$  V to +2 V. Specifically, there is no sign of a spin splitting on cobalt at an energy corresponding to the molecular spin splitting. Therefore, the observed spin

---

<sup>6</sup>For the current  $I$  in the denominator, the current of the corresponding spin channel is taken, as this agrees with the reasoning of Feenstra *et al.* [23, 90]. They do not consider spin-resolved experiments however. Alternatively, the spin-averaged current computed by the average of both spin channels could be used. Here, this would unnecessarily introduce data of an independently measured spectrum. For orbitals behind spin-polarised frontier orbitals, however, both procedures are arguable, as both kinds of normalisation introduce effects of the spin polarisation of the frontier orbital into the normalised LDOS of the orbital at higher energy. To my knowledge, there is no better normalisation for spin-polarised spectra so far.

<sup>7</sup>Note that the observation of zero integrated spin asymmetry at the stabilisation voltage, +2.0 V, already implies that integrated (from 0 to +2.0 V) SP-LDOS in antiparallel and parallel spin channel balance. At first glance, this seems to contradict with the observation of additional spin asymmetry at low positive bias voltage (cf. Figure 4.13). However, the spin asymmetry at low bias voltage is lower than the spin asymmetry of the LUMO, and, more importantly, the contribution of the LUMO to the total tunnelling current is much larger than the contribution of the low LDOS in the HOMO–LUMO gap. Finally, spin asymmetry does not equal spin polarisation, but even normalised spectra only approximate it.

splitting originates from the molecule and neither from a sign change of tip spin polarisation nor from a substrate spin splitting observed through a non-magnetic molecule.

The results presented above clearly demonstrate the spin splitting of the LUMO, manifested in point spectra taken above the  $\pi$ -orbital lobes. Similarly, point spectra taken at other positions, such as between the lobes, centred above the isoindole group, and above the centre also reveal a spin splitting with the same sign and very similar energy splitting. The spin difference between lobes closely follows the behaviour on the lobes, with identical energy positions and polarisation. For spectra taken over the isoindole group and the centre, the splitting shifts to higher energies by about 100 mV, and the polarisation is reduced to about half the magnitude observed over the lobes. The shift to higher energies matches the energy shift of the full peak already observed in the spin-averaged point spectrum (Figure 4.4a). The explanation for the lower magnitude of spin polarisation is simple: As visible from  $dI/dU$  maps in Figure 4.14b,c, the LDOS of the LUMO is significantly higher over the lobes than over centre and macrocycle. A lower contribution of the spin-split LUMO to the total LDOS measured at the given energy results in a lower polarisation.

### **Error estimation of spin splitting magnitude fit**

The error of tip stabilisation height is dominated by  $z$  noise, lateral mispositioning due to lateral creep, and  $z$  creep. The last contribution is visible in the comparison of start and end current of a forth-and-back spectrum and is reduced by introducing waiting times. Equal recording times for both spin channels reduce the effect upon the spin difference. The other two noise sources contribute a systematic error of about 1% for the signal and thus about 2% for the computed spin asymmetry. Additionally, there are random errors from  $z$  noise and  $I$  noise. The error from the fit of the Lorentzians is comparably low. Modification of the energy interval or restriction to fewer curves gives very similar results. The error of the spin splitting is dominated by the systematic error from approximating LDOS by normalised spectra and the potentially energy-dependent spin polarisation of the tip; it is estimated to be about 20 mV.

## **4.5 Discussion and Outlook**

In summary, two effects of spin polarisation are identified on TbPc<sub>2</sub>/Co/Ir(111): spin polarisation with cross-like spatial distribution following the lower Pc

ring in the HOMO–LUMO gap, and a spin splitting of the LUMO.

The effect in the HOMO–LUMO gap originates from hybridisation of states of substrate and lower Pc ring, evident from the spatial distribution of the spin polarisation. A similar effect was observed by Brede *et al.*, where CoPc molecules adsorbed on ferromagnetic iron double layers on W(110) showed even newly arising spin-polarised states with highly structured spatial distribution not resembling orbitals of free molecules. Here, the observation evidences magnetic interaction between cobalt nanostructures and lower Pc ligand. The effect is visible only in the HOMO–LUMO gap, in absence of molecular orbitals. For elevated bias voltages, their contribution dominates the tunnelling current, so further potentially existent hybrid states cannot be observed.

The spin splitting of the LUMO is a quite new result. Literature provides only sparse examples about splitting of orbitals of single molecules in contact to magnetic substrates. At the same time as the publication of the findings presented in this work, Kawahara *et al.* [91] reported the observation of a spin-split molecular orbital on C<sub>60</sub> molecules on Cr(001), spatially mapped and energetically resolved by SP-STM as well. The magnitude of the spin splitting is about 0.5 eV. Getzlaff *et al.* [92] investigated single benzene molecules on iron films on W(110) and did not find an exchange splitting of molecular orbitals. For phthalocyanines, double or single-deckers, spin splittings have not been observed so far. The magnitude of spin splittings observed for atomic submonolayer films of oxygen on Co(100) (200 meV) [93], iodine (150 to 350 meV) [92] and xenon (180 to 240 meV)<sup>8</sup> [92] on iron films on W(110) are comparable to the finding presented here ( $210 \pm 20$  meV). Spin contrast on the atomic scale has been achieved on molecules before, but without resolving molecular orbitals resembling pristine molecular orbitals of free molecules. Iacovita *et al.* [14] observed spin polarisation on the central cobalt atom of CoPc adsorbed on ferromagnetic Co/Cu(111), but no spin splitting, and no spin polarisation on the Pc ligand. Brede *et al.* [15] investigated CoPc molecules adsorbed on ferromagnetic iron double layers on W(110) and found them strongly interacting with the substrate. While the latter findings offer new prospects to design newly engineered spin-polarised interface states, the observation of spin polarisation of rather pristine molecular orbitals as presented here provides detailed insight into the combination of molecular systems and their interaction with a ferromagnetic support.

---

<sup>8</sup>Interestingly, a final state effect, remotely related to the situation of tunnelling into empty states

### Terbium centre

The central terbium atom deserves special attention as its spin system makes this molecule an SMM. Direct observation of 4f states is therefore highly desirable.

Vitali *et al.* assigned a cross-like structure, observed in a spin-averaging  $dI/dU$  map at a bias voltage of +0.4 V, “to the spin-polarized Tb states” [11]. Indeed, we do observe a cross-like spin-polarised structure at this bias voltage. However, it is rotated by 45°, following the lower Pc ring, not the upper, and is visible over the entire HOMO–LUMO gap (cf. 4.13). This observation clearly contradicts their result. The structure they observe by spin-averaging STM, following the geometry of the upper Pc, might simply reflect the molecular backbone within the HOMO–LUMO gap. Their DFT calculations give the same structure in charge density maps. These calculation were however performed for the free molecule; adsorption on cobalt might give a different result. Also, they do not comment on the vacuum decay length of these states; a short decay length might make them hardly visible to STM. Moreover, it remains unclear why and how the localised 4f orbitals (cf. Figure 2.2) spread over parts of the molecule; the authors explicitly exclude a hybridisation with the molecular ligand state.

Furthermore, neither point spectroscopy nor  $dI/dU$  maps reveal a state unique to the molecular centre, hence no signature that can be uniquely assigned to the Tb centre here.

The spin splitting of the LUMO is observed on the Pc ligand. The high interaction of the Pc ligands with the substrate, even resulting in spin-polarised hybrid states, and the high interaction of both Pc ligands strongly hint towards a direct coupling with the substrate. The Tb centre is not required for this effect. The effect should therefore be observable on YPc<sub>2</sub>, lacking 4f electrons, as well. A direct comparison to TbPc<sub>2</sub> would be interesting, but YPc<sub>2</sub> was not available during the experiments. Tb probably couples to the Pc rings via exchange interaction, or to the substrate via superexchange mediated by the four inner nitrogen atoms of the lower Pc ring. The high anisotropy, responsible for the classification as SMM, is not caused by exchange coupling but by a high-spin ground state in combination with a ligand field provided by the Pc ligands. Therefore, geometric modification of the nitrogen antiprism, modification of the charge state of the Pc ligands and thereby the nitrogen atom charge density, and exchange coupling by a ferromagnetic support offer different kind of access to this SMM.

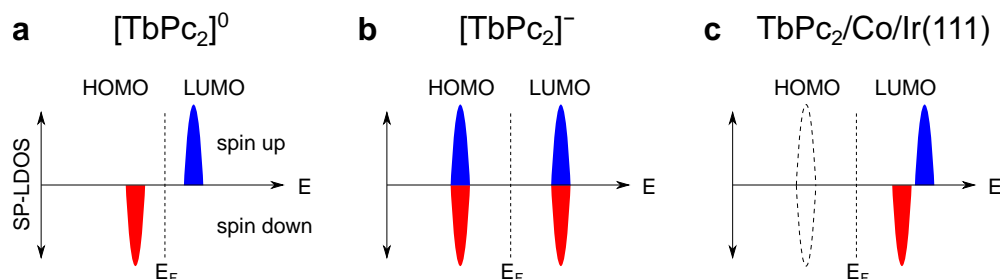


Figure 4.16: **Schematic spin-resolved states of  $\text{TbPc}_2$ .** (a) Neutral  $[\text{TbPc}_2]^0$  carries the  $\pi$ -radical ligand spin; its orbital is spin-split across the Fermi level into a singly occupied HOMO below, and an unoccupied state above the Fermi level. (b) In free negatively charged  $[\text{TbPc}_2]^-$  the HOMO is filled with the additional electron. Both spin states of the LUMO reside above the Fermi level. (c) Surface-adsorbed  $\text{TbPc}_2/\text{Co}/\text{Ir}(111)$  shows both spin channels of the HOMO below, and both spin states of the LUMO above the Fermi level, as in (b). Additionally, the LUMO is spin-split.

### Charge state of $\text{TbPc}_2$ on Co on Ir(111)

There is an interesting consequence of the fact that the LUMO is spin-split: The observation of a spin-split LUMO reveals the charge state of the molecule;  $\text{TbPc}_2/\text{Co}/\text{Ir}(111)$  is negatively charged.

For neutral  $[\text{TbPc}_2]^0$ , the frontier orbital is only singly occupied. By the Pauli exclusion principle, the present and the missing electron have opposite spin character. Here, occupied states are accessible by negative bias voltage and unoccupied states by positive bias voltage. Figure 4.16a depicts a schematic of the corresponding SP-LDOS of  $[\text{TbPc}_2]^0$ . In contrast, the experimental observation is schematically depicted in Figure 4.16c. Both spin channels of the LUMO of the investigated molecule are above the Fermi level, at positive bias voltage. This observation is incompatible with the assumption of an orbital spin-split around the Fermi level, and thus incompatible with the assumption of a neutral charge state. In a positively charged  $[\text{TbPc}_2]^+$  or negatively charged  $[\text{TbPc}_2]^-$  molecule, both up and down spins of the (respective) LUMO are above the Fermi level. An additional electron saturates the Pc rings (cf. chapter 2.2.3), and the electronegativity of all Pc atoms is higher than the one of cobalt surface atoms. Therefore, the molecule is negatively rather than positively charged. The charge transferred to the Pc ligand originates from the substrate and not from the Tb ion, as the  $\text{Tb}^{\text{III}}$  oxidation state is very stable. Similarly, Mugarza *et al.* [94] find mostly electron transfer towards single-decker transition metal Pcs on  $\text{Ag}(100)$ , even into saturated Pc ligands. It is crucial to clearly identify the observed STS

peaks with the frontier orbitals, as established here through their spatial distribution. Otherwise,  $\sigma$ -type frontier orbitals hardly visible to STM due to their more localised nature might be yet closer to (and potentially spin-split across) the Fermi level, giving a different result.

Most importantly, this finding implies that the ligand spin of  $[TbPc_2]^0$  is not present here, and thus the Pc ligand does not possess a magnetic moment. Nevertheless, a spin polarisation on the ligand is observed, so the advertised features of the ligand spin, namely a (magnetic) access to the Tb magnetic moment or read-out of Tb spin information through the ligand might be feasible even in the absence of a ligand spin.

### Upper and lower Pc ligand

The lower Pc ring is not directly visible to STM, as the signal from the upper ring dominates the tunnelling current. High similarity to free-molecule electronic structure, high Pc–Pc interaction as deduced from intact deposition (section 4.3) and difficult decomplexation (section 4.3.1), and large energy width (meaning strong coupling to the substrate) all together hint towards a joint  $Pc_2$  LUMO. On the contrary, the eight-lobe appearance is very similar to a pristine molecular orbital in contrast to a strong lower-Pc–substrate coupling, as manifested in the observation of spin-polarised hybrid states of surface and lower Pc ring only; this hints towards distinct lower and upper Pc rings with different electronic structure, while they still hybridise as manifested in the spin splitting of the upper Pc. The impact of differing Pc rings on the discussion given above is briefly discussed here. Spin-averaged spectroscopy, using a technique not as surface-sensitive as STM, could settle this question, as joint  $Pc_2$  gives different spectral lines than two distinct Pcs.

Assuming differing Pc rings rather than Pc rings with identical molecular orbital gives a similar picture concerning the spin splitting. The observed spin-split LUMO means that the frontier orbitals are filled with paired electrons. The upper Pc ligand can therefore be for example neutral, doubly negatively charged, or four times negatively charged. A double negative charge is most likely because it is the most stable oxidation state of a phthalocyanine ligand. Most importantly, a ligand spin is not present in this scenario either. Since the upper ring is too far away from the substrate for a strong direct coupling or dipolar coupling with the ferromagnetic substrate, the coupling is necessarily mediated via the Tb ion or the lower Pc ligand. Given the magnetic interaction of substrate and lower Pc (proven in the formation of spin-polarised hybrid states) and the large overlap between the Pc planes, a coupling mediated by the lower Pc is reasonable. As before, an influence of the Tb ion cannot be ruled out, but is not necessary to explain the observa-

tion. In summary, the key conclusions, namely the absence of a ligand spin and the lack of influence by the Tb centre, are the same whether or not the two Pc rings form a joint orbital. The alternative assumption of electronically different Pc rings might even open more prospects for modification of just one Pc ligand by the substrate. Heteroleptic double-deckers (i.e. chemically different upper and lower ligand) are interesting here, as different ligands for surface and vacuum side might prove useful.

### Sign of magnetic coupling

In principle, SP-STM can provide information about the sign of the magnetic coupling, i.e. ferro- or antiferromagnetic coupling for parallel or antiparallel alignment of the magnetisations. An observation of spin polarisation on the frontier orbitals of neutral  $[\text{TbPc}_2]^0$ , spin-split across the Fermi level, would give an immediate result: the dominating HOMO spin channel represents the majority spin carrier of the molecule, comparison with the substrate yields the sign of the magnetic coupling.

The sign of coupling is of additional interest as the internal coupling in  $\text{TbPc}_2$  is not clarified: Vincent *et al.* [45] find the coupling between Tb and  $\text{Pc}_2$  to be ferromagnetic and dominated by exchange interaction of about 0.35 Tesla for  $\text{TbPc}_2$  between gold electrodes. In contrast, Trojan *et al.* [95, 96] report a strong antiferromagnetic coupling between Tb and  $\text{Pc}_2$  ligand from low-temperature magnetic susceptibility data of powdered samples.

Antiferromagnetic or ferromagnetic coupling is not well defined for objects carrying no magnetic moment (such as the ligands of  $[\text{TbPc}_2]^-$ ), as an antiparallel or parallel alignment of magnetic moments is not given. Still a spin splitting into two spin components marks one spin channel to have higher binding energy, defining directionality. Nevertheless, Getzlaff *et al.* [92] denote the spin splitting of occupied states in iodine adsorbed on Fe/W(110) films a “ferromagnetic coupling” and an “induced magnetic moment”, even though these states do not cross the Fermi level.

In the present experiment, the LUMO is split into a lower-energy contribution in the spin channel antiparallel to the magnetic field and a higher-energy contribution parallel. This directly means that it takes less energy to put an electron with spin magnetic moment aligned antiparallel to the field into the  $[\text{TbPc}_2]^-$  molecule. Thus, the ligand orbital magnetisation of a hypothetical  $[\text{TbPc}_2]^{2-}$  (assumed to be unchanged and unperturbed by the additional charge) aligns antiparallel to the cobalt islands. Lacking reliable information about the HOMO spin polarisation, a similar conclusion for  $[\text{TbPc}_2]^0$  is not possible.

### Coupling of the spin systems

This work and Rizzini *et al.* [71] investigate double-decker Pcs on (different) ferromagnetic surfaces. Combining these experiments might give deeper understanding of the coupling of the spin systems (ligand spin, Tb centre, and ferromagnetic substrate). However, different substrate systems were used, so conclusions remain speculative. In the present experiment, SP-STM finds the LUMO to have a large spin splitting, spin-polarised molecule–substrate hybrid states, but no signature of the Tb centre. Rizzini *et al.* employ XMCD to study TbPc<sub>2</sub> on ferromagnetic nickel films. They observe an antiferromagnetic alignment of Tb and Ni magnetic moments, which is overcome by an external magnetic field of a few Tesla. They do not investigate the ligand spin system, so it remains unclear whether TbPc<sub>2</sub> or only the Tb centre aligns with the field. The application of SP-STM on their TbPc<sub>2</sub>/Ni/Cu(100) system might clarify the role of the Pc ligand. A combination of the existing results, tentatively assuming the Ni and Co interaction with TbPc<sub>2</sub> to be comparable, gives the following picture: The lower Pc ring strongly hybridises with the ferromagnetic support (section 4.3). The upper Pc strongly binds with the lower Pc. The upper Pc or the whole TbPc<sub>2</sub> is strongly exchange coupled or hybridised with the substrate (section 4.4.4). The terbium centre is coupled via direct exchange to the Pc, or via superexchange mediated by the inner nitrogen atoms to Ni. This coupling can be overcome by high magnetic fields in Rizzini’s experiment. As the 4f states interact only weakly with Pc, this is most likely the coupling overcome by high magnetic fields. This would imply that in Rizzini’s experiment only the Tb centre aligns with the field, not the full TbPc<sub>2</sub> molecule including its ligand spin; the Pc<sub>2</sub> ligand spin, if present, does not alter its alignment with the ferromagnetic substrate. A combination of SP-STM and XMCD experiments on the same substrate system might reveal the ligand spin polarisation, provide a comparison of the different coupling strengths involved, and clarify the direction (AFM vs. FM) of the alignment within the TbPc<sub>2</sub> molecule.

Interesting future experiments on this topic are XMCD investigations of the magnetisation of cobalt atoms below a full layer (or very high coverage) of TbPc<sub>2</sub> molecules in comparison with blank Co to directly investigate molecule–substrate hybrid states. SP-STM requires more direct access to the lower Pc ring to investigate these states. Experiments on TbPc<sub>1</sub> would be helpful, still the absence of the upper Pc gives a different system hampering comparison.

Having Rizzini’s experiment in mind, it is interesting to increase the magnetic field in the experiment presented here. Most likely the magnetic field of 6 Tesla provided by the STM setup is insufficient to break the large spin

splitting we observed. If the Pc–substrate coupling is strong (as evidenced here), ramping the field to align terbium as in Rizzini’s publication, SP-STM might or might not be able to detect a gentle effect of the changing Tb magnetisation on the LUMO spin splitting. While a few Tesla cannot overcome the large spin splitting observed in this work, lower splittings might be found on other substrates. Ramping the magnetic field in both directions and successfully altering spin polarisation in one direction would reveal the sign of the coupling of the Pc to the substrate.

Other magnetic substrates might maintain the neutral charge state of  $\text{TbPc}_2$ , show a spin-split orbital around Fermi and potentially provide information about the sign of the magnetic coupling.

An interesting follow-up experiment would be a simple repetition with  $\text{YPc}_2$  (which does not contain 4f electrons) replacing  $\text{TbPc}_2$ , to determine to what degree the 4f states influence the spin polarisation on the Pc ligand and the spin splitting.

### **SP-STM on $\text{TbPc}_2$ on Ir(111)**

Another interesting and possibly feasible follow-up experiment is to simply investigate the  $\text{TbPc}_2$  molecules adsorbed directly on the non-magnetic surface with a magnetic tip and in a small external magnetic field. The magnetic field shall align the magnetic moment of the molecule. The SP-STM tip needs to be antiferromagnetic to keep the tip’s spin direction fixed and thus the spin sensitivity stable independent of the applied external magnetic field.

The ferromagnetic cobalt islands serve as a magnetic reference to characterise the spin sensitivity of the antiferromagnetic chromium coated tip. This scheme is reminiscent to Miyamachi *et al.* [9], who claimed (cf. Steinbrecher *et al.* [10] for clarification) to observe the magnetisation of single magnetic holmium atoms adsorbed on Pt(111). Such an experiment is very tedious. In our case, either a ligand spin or direct access to Tb 4f states is required. Here, magnetic contrast on the cobalt islands has indeed been achieved, but measurements of low quality did not reveal a magnetic contrast on neither Pc ligand nor Tb centre.



# Chapter 5

## TbPc<sub>2</sub> on Ir(111)

This chapter is focussed on TbPc<sub>2</sub> molecules adsorbed on bare Ir(111). They show two distinct conformations, which can be switched into each other by the STM tip. One of them is achiral while the other is chiral. Moreover, the handedness of the chiral conformation can be changed, albeit not controlled. The combination of chirality and controlled switching on surfaces is new and of fundamental relevance for biology and chemistry. This chapter first describes the chiral conformation in section 5.1, then the achiral conformation in section 5.2, and finally the switching processes in section 5.3.

Molecular switches, i.e. molecules that can be reversibly switched between two or multiple states, are of high interest for several fields [97]. Information technology seeks for new bistable systems to store data or more complex devices to process data. Bottom-up fabrication demands nanoscale molecular machines for controlled assembly. Light and chemical sensitivity of molecules is interesting for optoelectronic devices and sensors. Switches can be driven locally (STM, AFM, break junctions) or macroscopically for example by electric field, tunnelling electrons, light, or temperature. These switch various properties of molecules, including charge or spin state and conformation.

A chiral molecule is a molecule not superposable to its mirror image. A standard example for chiral objects are the left and right hand. Similarly, chiral conformers are called right-handed and left-handed enantiomers. Chirality is of fundamental interest. In earth's lifeforms, some chiral molecules are found in only one handedness, a familiar example is lactic acid in yoghurt. The human body treats enantiomers differently, some medicine therefore requires enantioselective synthesis.

A large number of molecular switches has been found. Weigelt *et al.* [98] find molecules to randomly switch between chiral and achiral conformations driven by temperature. Qiu *et al.* [99] find porphyrin molecules in two different chiral conformations and switch between these conformations via the

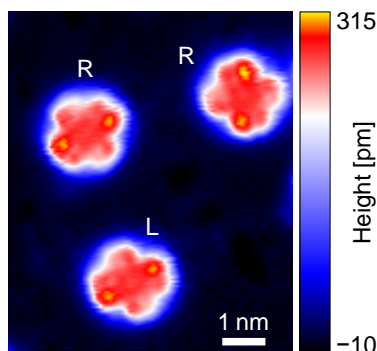


Figure 5.1: **Enantiomers of  $TbPc_2$  on  $Ir(111)$ .** The upper two molecules in this topograph appear identical but rotated by  $60^\circ$  with respect to each other. The bottom molecule appears very similar, but cannot be superimposed on the upper molecules. An object which cannot be superimposed on its mirror image is defined to be chiral. The molecules therefore are enantiomers, denoted here right-handed (R) and left-handed (L).  $U = +1.5$  V,  $I = 84$  pA, W tip. Data recorded by Yingshuang Fu.

STM tip. The switching processes are found to be driven by inelastic tunnelling and the electric field, respectively. They however cannot change the handedness of the chiral conformations. Komeda *et al.* [47] investigate the molecule studied here as well,  $TbPc_2$ . Adsorbed in monolayers on  $Au(111)$ , the azimuthal angle between the Pc planes is switched between two stable positions by voltage pulses of the STM tip. This changes the charge state and thereby the spin state of the molecule. They however do not observe a chiral motif.

## 5.1 Chiral conformation

When depositing  $TbPc_2$  molecules on a  $Co/Ir(111)$  substrate, alongside with those on Co islands, molecules also adsorb on the bare  $Ir(111)$  surface. In contrast,  $CoPc$  molecules on a substrate with Co islands on  $Cu(111)$  accumulate on Co islands [14]. Deposited on an  $Ir(111)$  sample kept at room temperature,  $TbPc_2$  molecules are isolated on the surface. They neither form self-assemblies nor assemble at island or step edges. All these observations indicate that the molecule–substrate interaction is high, similar to  $TbPc_2$  molecules on Co islands (cf. chapter 4).

Figure 5.2 provides insight into the electronic structure of the molecules. As topography-corrected maps of differential conductance give the best defined approximation of maps of molecular orbitals (cf. chapter 1.5),

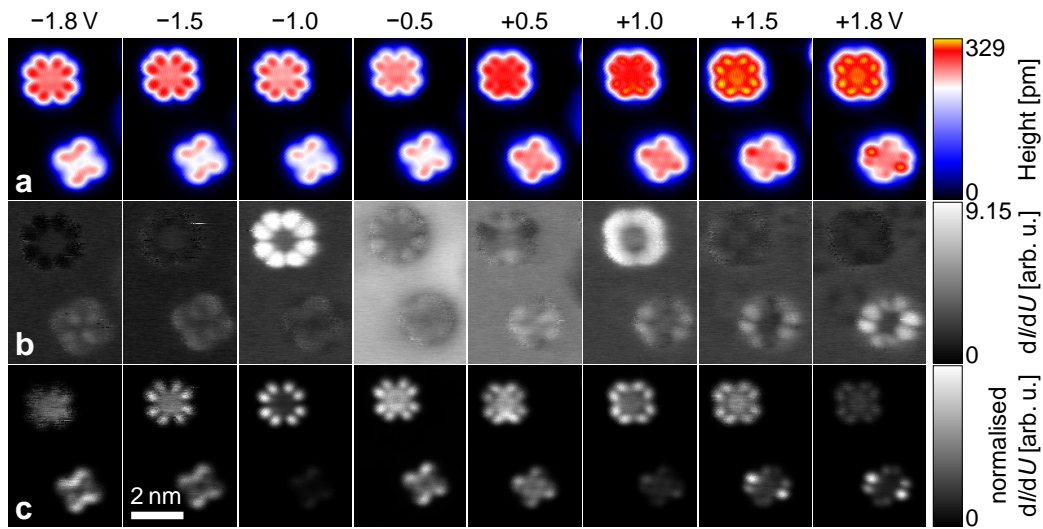


Figure 5.2: **Energy-dependent appearance of TbPc<sub>2</sub> on Ir(111).** Topographs, maps of differential tunnelling conductance, and topography corrected maps of differential conductance at different bias voltages. (a) Topograph of TbPc<sub>2</sub> molecules adsorbed on Ir(111), achiral (top) and chiral (bottom). Bias voltages are specified above the images. The same colour scale applies to all images.  $I = 100$  pA,  $U_{\text{mod}} = 50$  mV,  $f_{\text{mod}} = 1111$  Hz (b) Simultaneously recorded maps of differential tunnelling conductance. (c) Topography-corrected maps of differential conductance. Individual colour scales to improve contrast.

they are discussed in the following. The topography corrected maps of differential conductance taken at  $U = +1.5$  V and  $+1.8$  V give the highest intensity. They both show eight lobes over the pyrrole rings, indicating  $\pi$ -type molecular orbitals. They are assigned to the LUMO. The maps show eight lobes with different intensities in a  $C_2$  geometry, i.e. lobes opposing each other appear equally strong. Also, pairs of lobes belonging to the same pyrrole group appear equally strong for pyrrole groups opposing each other, but different for neighbouring ones, resembling a saddle shape geometry. The two lobes of each pyrrole group aren't equally strong either and match the saddle-like appearance. While eight lobes are typical for  $\pi$  orbitals as observed for  $TbPc_2$  on Co as well, the difference in intensities might (at this point) stem from a geometrical distortion of the molecule, or from its arrangement on the substrate [94]. With the given set of observations this distortion might be a saddle-shaped deformation of the upper Pc ring simply matching the intensity of the molecular orbitals, or a deformation involving both Pc rings, which changes the tunnelling paths.

At low negative bias voltage ( $U = -0.5$  V and  $-1.0$  V) only four lobes are resolved, which merge into two larger banana-shaped regions at  $U = -1.5$  V and  $-1.8$  V. The ends of the banana-shaped regions are at the same positions as the highest appearing lobes of the LUMO. Having the similarity of HOMO and LUMO of Pc molecules in mind (they stem from  $a_{1u}$  and  $e_g$  orbitals, both with predominant  $\pi$  character), these maps likely show a combination of a  $\pi$ -type HOMO and a contribution similar to the four bright spots in the uncorrected  $dI/dU$ -map at  $U = -1.8$  V. These spots follow the lobes of the lower Pc ring and thus probably originate from it. Maps taken at low positive bias voltage ( $U = +0.5$  V and  $U = +1.0$  V) show two neighbouring crosses, with an addition of the brightest lobes of the map taken at the next higher bias voltage, at  $U = +1.5$  V. The low intensities indicate that these maps show the molecular backbone together with the tail of the LUMO.

In all maps of differential tunnelling conductance presented in Figure 5.2, the centre of the molecule shows lower intensity than the lobes. Chiral  $TbPc_2$  on Ir(111) therefore does not show a state directly stemming from the terbium centre.

The  $dI/dU$  spectrum presented in Figure 5.6 is featureless apart from steep increases at  $-1.9$  V and  $+1.8$  V. These likely represent flanks of HOMO and LUMO peaks; the molecular orbitals imaged at  $U = \pm 1.5$  V and  $\pm 1.8$  V, thus the tail of these frontier orbitals, represent HOMO and LUMO of the chiral conformation. This gives a HOMO–LUMO gap of more than 3.5 eV, which is very high for both double-decker [47, 11] and single-decker [85, 100] Pc molecules.

### 5.1.1 Orientation

As described above, the molecules show four lobes at low bias voltage (Fig. 5.2a). In contrast to the  $D_{4h}$  symmetry of free  $TbPc_2$  and the  $C_2$  symmetry observed at higher bias voltage, the low bias voltage maps show a mirror symmetry with symmetry axes between the lobes, giving a  $C_{2v}$  symmetry. Several single-decker Pc molecules adsorbed on metal fcc(111) surfaces [81] are two-fold symmetric as well, but with symmetry axes following the cross of the lobes. Assuming that the lower and upper Pc rings are rotated by  $45^\circ$  with respect to each other, the symmetry axes observed here follow the cross of the lower Pc ring. Thus, this  $C_{2v}$  symmetry observed here might be induced by a similar adsorption of the lower Pc adsorbed on an fcc(111) surface.

The axes of mirror symmetry are slightly misaligned with respect to the Ir(111) close-packed rows by  $(4 \pm 1)^\circ$ . As shown in Figure 5.3, both molecules rotated to the left as well as molecules rotated to the right exist. While these conformations appear very similar at low bias voltage, they clearly show a sense of rotation at higher bias voltage corresponding to molecular orbitals (Fig. 5.2b). A molecule as presented above cannot be superimposed on its mirror image. It is by definition chiral, with the two conformations shown in Figure 5.1 denoted here the left-handed and right-handed enantiomer.

The investigation only covers a bias voltage range within  $\pm 2$  V, as a higher voltage makes the molecule switch into a different conformation. The following section describes this conformation, before going into details of the switching process in section 5.3.

## 5.2 Achiral conformation

Depositing  $TbPc_2$  onto a room-temperature sample yields the chiral conformation described above. Deposited onto a sample held at low temperature ( $\approx 100$  K),<sup>1</sup>  $TbPc_2$  molecules adsorbed on Ir(111) look clearly different (see the upper molecule in Figure 5.2). This second conformation of  $TbPc_2$  on Ir(111) can easily be distinguished from the first at all bias voltages, as it always shows eight nearly equally high lobes and is not chiral. These eight lobes are most pronounced in maps of differential tunnelling conductance taken at  $U \leq -1.0$  V and  $U \geq +1.0$  V (Fig. 5.2b). A  $dI/dU$  point spectrum

---

<sup>1</sup>This temperature is only an estimate. It is described best by the deposition procedure: The pre-cooled sample is taken out of the STM ( $T \sim 40$  K) with the room-temperature wobble stick, held in front of the molecule evaporator for  $\sim 30$  seconds of deposition and immediately put back into the STM.

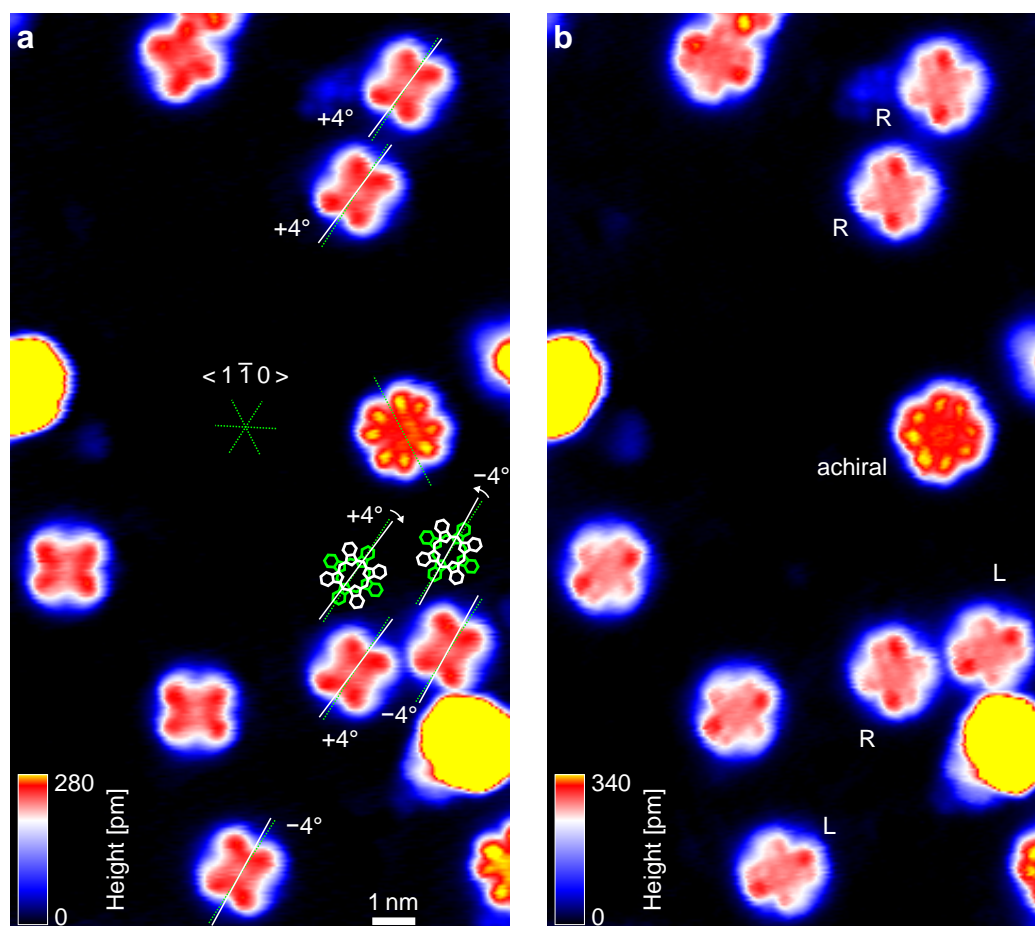


Figure 5.3: **Orientation of the chiral conformation.** (a) Topograph taken at  $U = -1.0$  V to reveal the  $C_{2v}$  symmetric appearance of the chiral conformation. The 8-lobed achiral molecule serves as reference for the surface close-packed rows. The apparent symmetry axes of the chiral molecules deviate from these axes by  $(4 \pm 1)^\circ$  to the right or left. (b) Topograph of the same area, taken with  $U = +1.5$  V to reveal the handedness of the molecules. Those molecules rotated to the right (left) are identified with the enantiomers denoted right(left)-handed.  $I = 84$  pA. Data recorded by Yingshuang Fu.

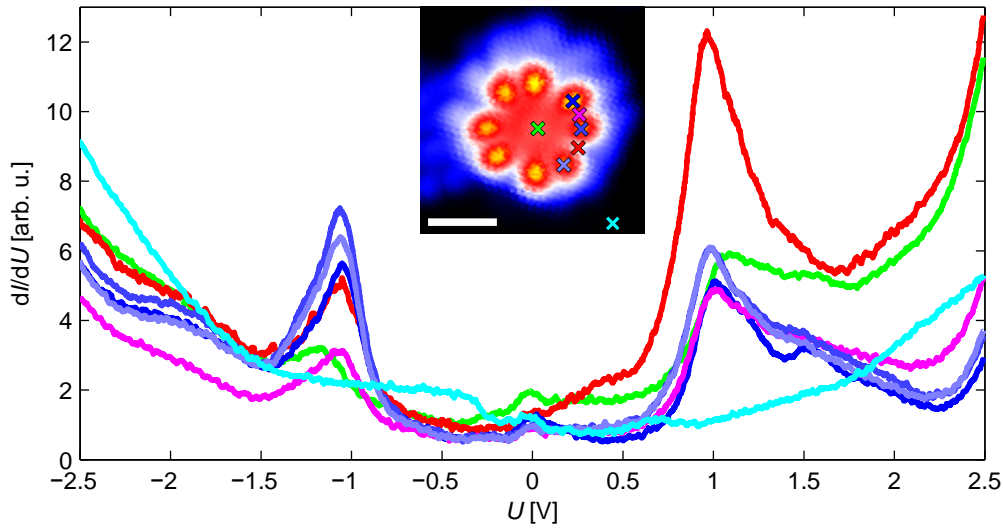


Figure 5.4: **Point spectroscopy of achiral TbPc<sub>2</sub> on Ir(111).** All spectra taken over lobes (blues, red, magenta) exhibit pronounced peaks for the HOMO at  $U = -1.1$  V and the LUMO at  $+1.0$  V. For both spectra taken between lobes (red, magenta) the LUMO appears twice as intense as the HOMO, in agreement with the larger lateral dimension of LUMO lobes in topography. The peaks of the spectrum taken over the centre (green) shift away from the Fermi level by  $\sim 100$  mV. The zero-bias peak is present on all spectra including the substrate, and therefore reflects the LDOS of the tip, not the sample.  $U_{\text{stab}} = -3.0$  V,  $I_{\text{stab}} = 1$  nA,  $U_{\text{mod}} = 50$  mV,  $f_{\text{mod}} = 6777$  Hz. Topograph:  $U = -1.5$  V,  $I = 1$  nA, white scale bar 1 nm, colour scale spans 280 pm.

(Fig. 5.4) reveals peaks residing at these energies, so they can be identified as HOMO ( $U = -1.1$  V) and LUMO ( $U = +1.0$  V) of this conformation. Both clearly show eight-lobed  $\pi$  orbitals. At energies between HOMO and LUMO, 8 lobes are still clearly visible but do not appear higher than the centre, as the molecular backbone is imaged, rather than a frontier orbital. The 4-fold  $D_{4h}$  symmetry of free  $TbPc_2$  is reduced to a two-fold  $C_{2v}$  symmetry. The symmetry axis again is perpendicular to a close-packed row of the Ir(111) surface. As this conformation is mirror symmetric, it is achiral, in contrast to the chiral conformation described above.

## 5.3 Switching

This section first describes the switching from a chiral to an achiral conformation in section 5.3.1, then the reverse switching in section 5.3.2, and finally switching to achieve a change of handedness in section 5.3.3.

### 5.3.1 Switching the chiral conformation into the achiral conformation

The chiral conformation is switched into the achiral conformation by an elevated bias voltage. Both STM imaging and point spectroscopy visualise this. Figure 5.5 shows molecules in the chiral conformation imaged at  $U = +1.8$  V, which are scanned with a higher bias voltage of  $+2.0$  V in panel (b) and suddenly transform into the achiral conformation while the tip is scanning. Similarly, the switching occurs when reaching a sufficiently high bias voltage in a point spectroscopy voltage ramp. When recording a point spectrum (Fig. 5.6) with a bias voltage exceeding a threshold, a sudden jump or drop in both current and  $dI/dU$  signal occurs. When ramping back, the  $dI/dU$  spectrum follows a different trajectory, as it now monitors the LDOS of the achiral conformation. The STM tip remains unaffected by the switching process.

To get deeper insight into the switching mechanism, the current dependence of the switching rate is investigated. The tip is stabilised over the centre of the molecule with a bias voltage below the switching threshold ( $U = +1.5$  V) and with different currents of a large range of 25 pA to 5000 pA. The bias voltage is then quickly (0.2 seconds) ramped to  $U = -2$  V, which is sufficient to switch the molecule. The current is recorded; a jump denotes the switching event. This procedure is repeated for about 50 molecules. The resulting switching times vary from below one second to minutes. Especially, they vary for a given current, indicating that the process is of statistical

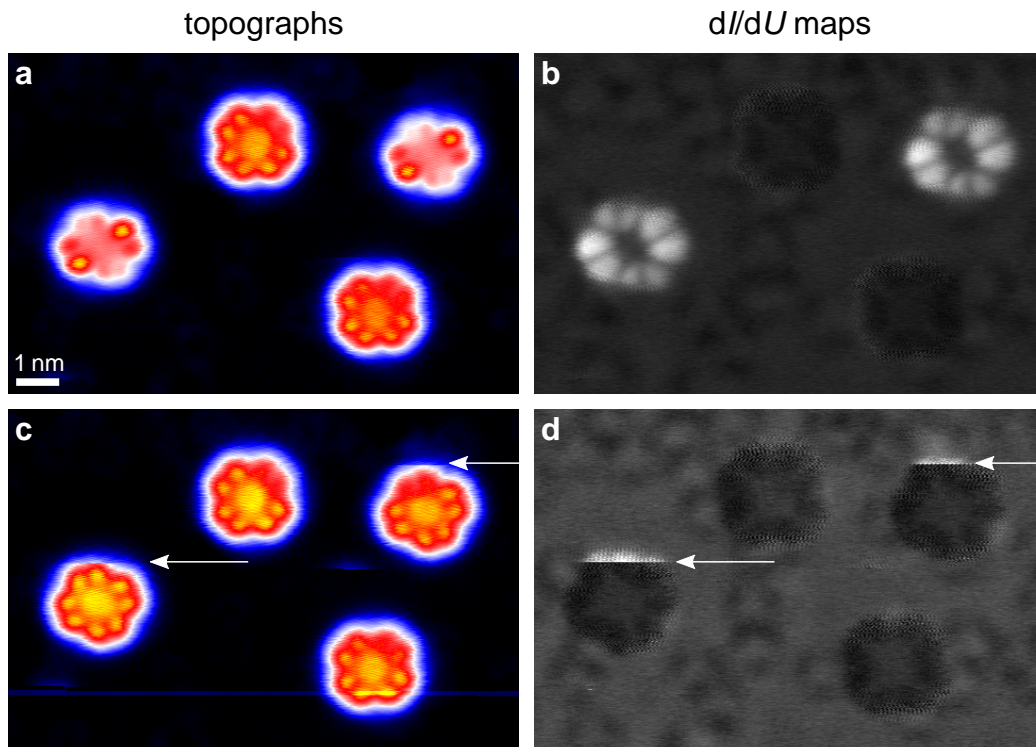


Figure 5.5: **Switching of chiral  $\text{TbPc}_2$  during STM imaging.** (a) Topograph with two chiral and two achiral  $\text{TbPc}_2$  on Ir(111).  $U = +1.8 \text{ V}$ ,  $I = 1 \text{ nA}$ . (b) Simultaneously recorded map of differential tunnelling conductance. The chiral conformers appear much brighter.  $U_{\text{mod}} = 20 \text{ mV}$ ,  $f_{\text{mod}} = 6777 \text{ Hz}$ . (c) Topograph of the same area, with a higher bias voltage of  $U = +2.0 \text{ V}$  to switch the molecule. Arrows indicate where the chiral conformation switches into the achiral conformation, which is subsequently imaged. (d) Simultaneously recorded map of differential tunnelling conductance. The large drop in differential tunnelling conductance from chiral to achiral marks the switching event. Data recorded by Yingshuang Fu.

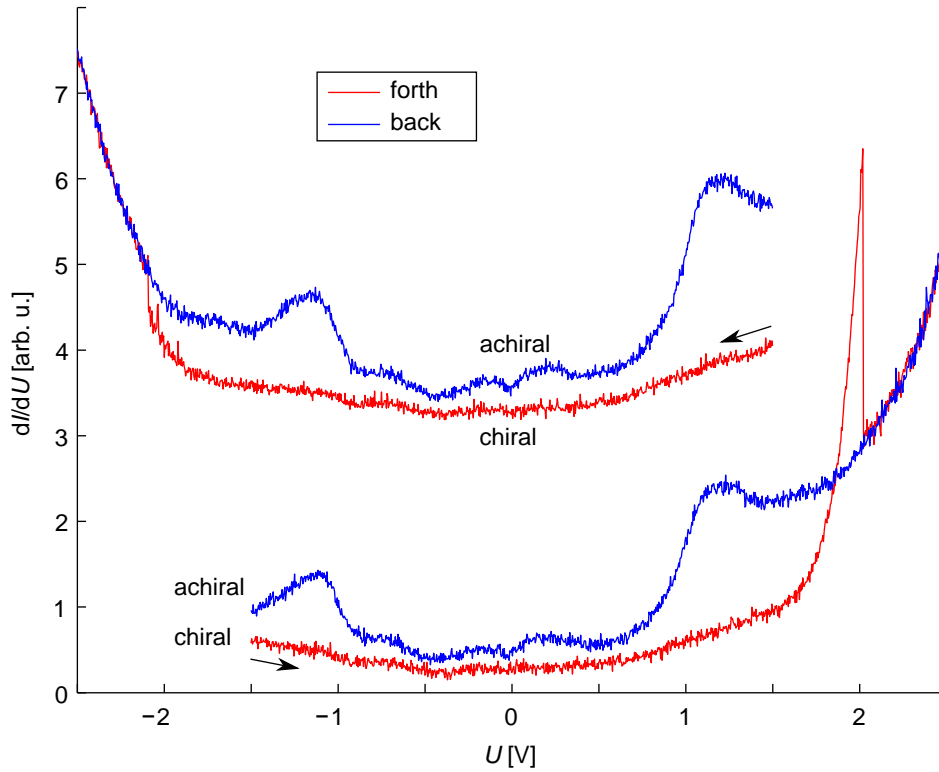


Figure 5.6: **Switching of chiral  $TbPc_2$  during tunnelling spectroscopy.** Two events (a,b). The tip is stabilised over the centre of a chiral molecule with  $U = \pm 1.5$  V, then the bias voltage is ramped and the  $dI/dU$  signal recorded (red curve). At  $U \sim \pm 2.0$  V the molecule switches as can be seen from the jump or drop in the  $dI/dU$  signal. The  $dI/dU$  curve then follows a different trajectory now representing the  $dI/dU$  curve of the achiral conformation. The upper set of curves is set higher by 0.3 arb. u. for better visibility.  $U_{\text{stab}} = -1.0$  V,  $I_{\text{stab}} = 50$  pA. Data recorded by Yingshuang Fu.

nature. The inverse of the average time gives a switching rate. This is plotted against the current in Figure 5.7a. The proportional dependence indicates a one-electron process. Multi-electron processes are clearly excluded, as they result in higher orders ( $f \propto I^n$ ). The quantum yield, i.e. the switching probability per electron, is given by the quotient of rate and current. At  $U = -2\text{ V}$  it is about  $5 \cdot 10^{-10}$ .

Another experiment is performed to quickly elucidate the dependence on the electric field. Again, the tip is stabilised at  $U = +(-)1.5\text{ V}$  and different currents. The bias voltage is then slowly ramped towards  $-(+ )2.5\text{ V}$ , and the current is recorded. Again the switching event is observed as a jump in current. The ramping speed is  $2\text{ V/s}$  for all tunnelling currents. To properly determine a threshold bias voltage, the ramping speed must be slow regarding the switching time at a given current. As the average switching time has already been determined to be on the order of several seconds for the lowest currents, the ramp speed used here is much too fast to allow for a correct determination of a threshold bias voltage. Still some results can be retrieved from this experiment. First of all, the absolute values of negative and positive switching bias voltages are identical within the error bars. This eliminates the possibility of a particular molecular orbital playing a crucial role in the switching process. Furthermore, the effect of the excessively high ramping speed can be discussed qualitatively: Low currents give a lower switching yield, therefore the switching occurs later, i.e. when the bias voltage has been ramped further. Thus, the observed switching bias voltage shifts to higher absolute values for small currents, giving more similar switching voltages depending less strongly on the tunnelling current than apparent from the graphs. A linear fit to the data in Figure 5.7b gives a finite y-intercept at about  $\pm 1.4\text{ V}$  for a reasonable tip-sample separation of  $\sim 500\text{ pm}$  for the highest currents. As discussed above, corrected data would give an even larger y-intercept. If a threshold electric field was needed, tip-sample distance and switching voltage would be proportional ( $|\vec{E}| = U/z$ ). This is not the case here, ruling out an electric field driven switching process.

As an electric field driven process is ruled out and no particular molecular orbital drives the process, the switching process is attributed to inelastic tunnelling (IET). The tunnelling electrons excite inelastic excitations in the molecule when probing HOMO or LUMO. The bias sign insensitivity indicates that a certain energy, rather than access to a specific orbital, is needed to switch the molecule.

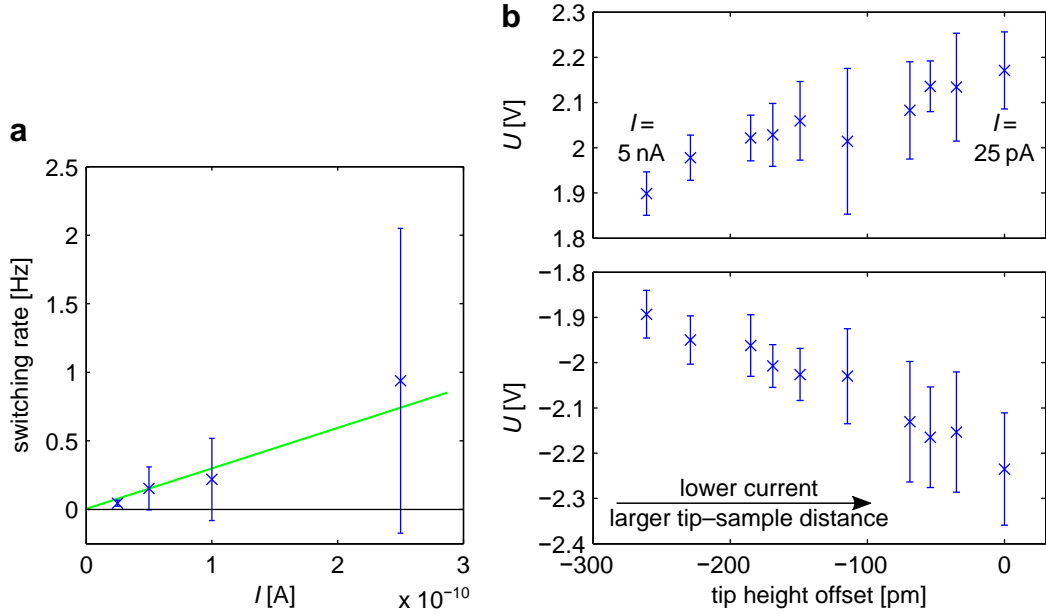


Figure 5.7: **Statistics of switching from chiral to achiral conformation.** (a) Linear dependence of current and switching rate, indicating a one-electron process. Procedure: The tip is stabilised at  $U_{\text{stab}} = -1.5$  V and  $I_{\text{stab}}$  indicated on the horizontal axis, the bias voltage ramped quickly ( $t = 0 \dots 0.2$  s) to and held at  $U = -2.0$  V, and the time until the switching event (indicated by a jump in current) recorded. (b) Switching bias voltage as a function of tip-sample separation, to investigate a possible electric field dependence. Procedure: The tip is stabilised at  $U_{\text{stab}} = -(+)1.5$  V and  $I_{\text{stab}}$  indicated on the horizontal axis, the bias voltage ramped slowly ( $\pm 2$  V/s) towards the opposite bias polarity until  $U = +(-)2.5$  V, and the bias voltage at the switching event (indicated by a jump in current) recorded. Zero tip height offset is arbitrarily referenced to  $I = 25$  pA. Data recorded by Jens Brede.

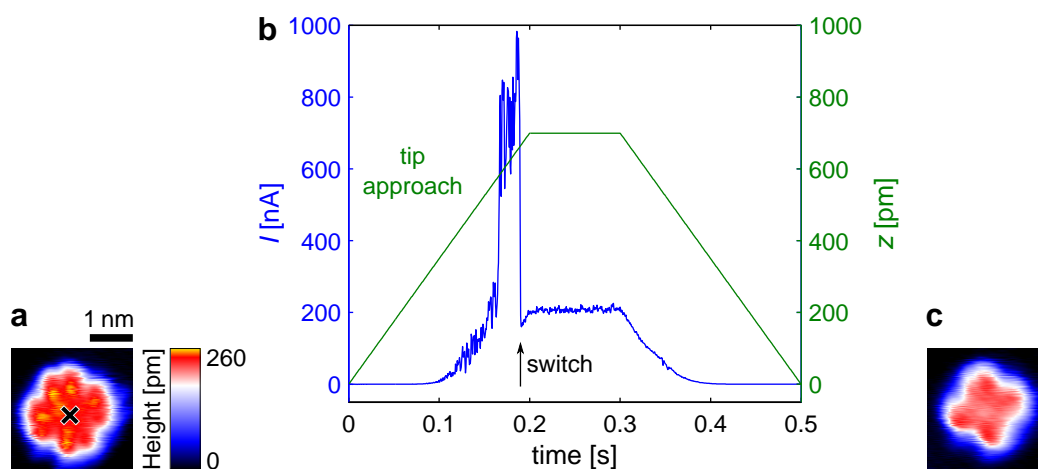


Figure 5.8: **Switching from achiral to chiral.** (a) Topograph of TbPc<sub>2</sub> in its achiral conformation. (b) To switch into the chiral conformation, the STM tip (stabilised at  $U_{\text{stab}} = +1.5$  V and  $I_{\text{stab}} = 110$  pA) approaches by 700 pm over the centre of the molecule (green curve). The tunnelling current (blue curve) increases exponentially as the tip approaches ( $U = 50$  mV). At 0.19 seconds the molecule switches, making the current drop sharply. Then the current again increases to  $\sim 200$  nA until the tip stops approaching. With a constant tip height, the current then remains constant ( $t = 0.2 \dots 0.3$  s), and decreases when the tip retracts. (c) The subsequent topograph proves that the molecule has switched into the chiral conformation.  $U = -1.0$  V,  $I = 110$  pA. Data recorded by Yingshuang Fu.

### 5.3.2 Switching the achiral conformation into the chiral conformation

Switching the achiral conformation into the chiral one is also feasible, although with a low success rate. The tip is stabilised above the centre of the molecule and approached close to contact with a low bias voltage of  $\pm 50$  mV. Figure 5.8b shows a sudden drop in current at  $\sim 900$  nA. The subsequent topograph (Fig. 5.8c) confirms that the molecule has switched. This method has proven successful with both bias polarities. The success rate is low ( $< 5\%$ ), as the molecule often decomposes in the process, typically leaving an ill-shaped molecular rest rather than the lower Pc ring as observed in the decomplexation experiment. The tip apex often changes as it adsorbs molecular left-overs. While the first switching attempt is rarely successful, several successful switching events often follow the first success. This hints towards a dependence on the tip stability. The tunnelling current needed to switch the molecule is on the order of 1  $\mu$ A, whereas already 5 nA are suffi-

cient to decompose the molecule by scanning or lateral tip manipulation. To find a more efficient method, both pulses with higher (+1.0 V) and yet lower bias voltage ( $\pm 5$  mV) are tested, approaching the tip step by step closer to the molecule. Bias voltages well below  $\pm 2$  V are chosen to prevent the molecule from switching back. None of these attempts proves to be successful. As the success rate is low, and failure usually results in tip changes requiring time-consuming tip treatment, a precise experimental investigation of this switching process is not feasible. Still some conclusions can be drawn from the kind of pulse applied. Two parameters are unusual during this switching process: the very high tunnelling current and the close vicinity of tip and molecule. The vicinity of tip and molecule might induce deformations due to the locally high electric field, or make the molecule jump to contact and randomly relax into the achiral or chiral conformation or decompose. The high current points towards a very appealing and plausible scenario: the high current heats the molecule<sup>2</sup> by Joule heating [102] and makes it switch or relax into its lowest energy conformation, the chiral one. This agrees well with the observation of chiral molecules after room temperature deposition and achiral molecules after low temperature deposition. Here, room temperature provides the thermal energy to relax into the lowest energy conformation, whereas molecules deposited onto a cold sample cool down quickly and maintain a structure more similar to a free *TbPc<sub>2</sub>* molecule. To substantiate the hypothesis, a sample prepared at low temperature is warmed up to room temperature, and subsequently cooled down for measurement. Nearly all achiral molecules are found to have relaxed into the chiral conformation. These molecules clearly switched due to heat input as well, substantiating the hypothesis.

The low success rate of this switching process also prevents deeper investigation of the reverse switching process, as statistics requires a large number ( $\gtrsim 1000$ ) of switching events, which is only feasible with reliable back-and-forth switching.

### 5.3.3 Chirality change

As the molecule can be switched from the chiral conformation to the achiral one and back, a chirality change, i.e. switching between enantiomers and thereby changing handedness, should be feasible. Figure 5.9 shows a sequence of images presenting an initially right-handed chiral molecule, which

---

<sup>2</sup>A quantitative comparison with literature is difficult as the molecular temperature is hard to determine, and cooling by the substrate varies a lot depending on molecule-substrate coupling. Here,  $\sim 50$  mV $\cdot$ 1000 nA  $\approx 50$  nW heat the molecule (to  $T \gtrsim 100$  K), whereas Schulze *et al.* [101] crack *C<sub>60</sub>* molecules ( $T \sim 1000$  K) by a few  $\mu$ W.

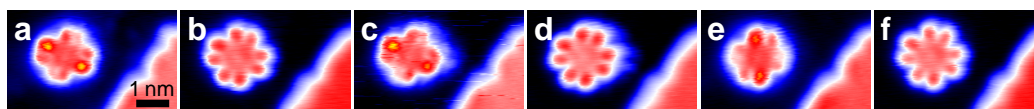


Figure 5.9: **Chirality change.** Series of topographs of  $\text{TbPc}_2$  on  $\text{Ir}(111)$ , switched between chiral and achiral conformation in each step. The switching process does not control handedness. The molecule first switches back to its initial handedness (a,b,c), and then successfully changes handedness (c,d,e) in the second attempt.  $I = 84 \text{ pA}$ ,  $U = +1.5 \text{ V}$  (a,c,e),  $-1.0 \text{ V}$  (b,d,f), colour scale 0 to 320 pm. Data recorded by Yingshuang Fu.

is switched forth and back to the achiral and chiral conformation by scans at elevated bias voltage of  $U = \pm 2.5 \text{ V}$  and by the tip-approach scheme, respectively. The first attempt yields a right-handed enantiomer again, the second attempt successfully changes handedness to the left-handed enantiomer. Note that the switching process from achiral to chiral conformation does not control the handedness, so the outcome of the switching is assumed to be random. The scheme applied for this switching process is inherently insensitive to the handedness of the resulting conformation as the tip is stabilised over the centre of the molecule. An off-centre stabilisation position could potentially allow for controlling the handedness, or at least shift the probability of the outcome. This could be addressed in future experiments, but in case of a thermally driven switching mechanism, a directionality is unlikely; still the tip position might introduce directionality by modifying the final state energy landscape.

### 5.3.4 Geometrical structure of the conformations

To elucidate the difference of the conformations, molecular symmetry and orientation are discussed in this section.

Two high symmetry adsorption sites reduce the  $D_{4h}$  symmetry of free  $\text{TbPc}_2$  to the  $C_{2v}$  symmetry of the achiral conformation: top and bridge site. No adsorption site induces the  $C_2$  symmetry of the chiral conformation, as long as the  $D_{4h}$   $\text{TbPc}_2$  aligns with crystal symmetry axes. A rotation of  $\text{TbPc}_2$  away from the substrate axes, or a rotation of only one of the Pc rings, breaks the mirror symmetry of the joint system and reduces it to  $C_2$  on top and bridge sites (the same as for the achiral conformation! Conformation changes therefore do not require lateral motion). All other adsorption sites give an asymmetric joint system. Furthermore, a rotation induces chirality, as rotation to left or right gives two different enantiomers. Other deformations also reduce the  $D_{4h}$  symmetry of free  $\text{TbPc}_2$  to  $C_2$ : a propeller-like tilt

of all Pc lobes, or a saddle-shaped deformation not following a substrate axis. However, a propeller-shaped deformation does not agree with the saddle-like appearance of the LUMO, and a saddle-shaped deformation does not explain the  $C_{2v}$  symmetry observed at low bias for the chiral conformation. Thus, a rotation is the most likely scenario. Indeed, at low bias voltage the chiral conformation shows a  $C_{2v}$  symmetry, with the mirror axis rotated by  $4^\circ$  with respect to the symmetry axis of the achiral conformation. The rotation could be a rotation of the entire molecule with respect to the substrate, or an azimuthal rotation of the upper Pc ring with respect to the lower ring which remains aligned with the substrate. These two proposed scenarios only differ in the orientation of the lower Pc ring, while the upper ring in both cases is rotated by  $4^\circ$  with respect to a substrate close-packed row, as deduced from the apparent rotation of the low-bias appearance of the chiral conformation. By STM, it is hard to distinguish these scenarios as the lower Pc is farther away from the tip than the upper one, and therefore gives a much lower contribution to the tunnelling current by about a factor of 100 (cf. chapter 1.1). An obvious idea to gain direct access to the lower Pc ring is a removal of the upper one by manipulation with the tip. However, such a decomplexation is not a convincing strategy as the harsh tunnelling conditions during manipulation and, more importantly, the process of decomplexation itself easily provide sufficient energy for the leftover lower Pc ring to relax into a new lowest energy position. The high molecule–substrate interaction means that a rotation of the entire molecule is less likely; previous studies indicate that an azimuthal rotation [47, 103] is feasible, Komeda *et al.* [47] use 2 Volt pulses by the STM tip to rotate the Pc ligand, very similar to the process found here. An azimuthal rotation is therefore the more likely scenario.

Mugarza *et al.* [94] observe similar chiral orbitals for single-decker Pcs on Ag(100). There, the  $D_{4h}$  molecules are rotated with respect to a  $C_{4v}$  surface symmetry. While the nuclear positions of the molecules remain in the molecular plane and do not exhibit chirality (as found by DFT), the electronic molecular orbitals do. Here, the saddle-shape appearance of the LUMO of the chiral conformation might be similarly caused by a simple rotation, without a saddle (or other) deformation of the nuclear positions. This also explains the absence of saddle-type appearance in the HOMO–LUMO gap.

## 5.4 Summary

$TbPc_2$  on Ir(111) shows a chiral and an achiral conformation, which can be switched into each other by the STM tip. Chirality can therefore be switched

on and off by switching between the chiral and the achiral conformation, and the handedness can be changed (though not controlled) by switching from a chiral to the achiral and back to a random chiral conformation. The chiral conformation is switched easily (with 100% success rate and non-destructive) into the achiral one by tunnelling at elevated bias voltages. The process is determined to be a one-electron process involving inelastic tunnelling electrons. The reverse process is more tedious and brutal: approaching the tip close to the molecule sometimes switches it back by local current heating of the tunnelling electrons, and often makes it decompose. The process is not enantioselective. Room-temperature and low-temperature preparation yield the chiral and achiral conformation, respectively. This allows for macroscopic control of chirality. Warming up a low-temperature preparation to room-temperature makes the achiral molecules switch to chiral ones. The switching is probably accompanied by an azimuthal rotation of the upper Pc ring by  $4^\circ$ . The HOMO–LUMO gap of the chiral conformation is larger by more than 1 eV, larger than observed on single-decker or double-decker Pc molecules so far. According to calculations of the electronic structure of  $\text{TbPc}_2$  [86, 47], an azimuthal rotation by  $4^\circ$  changes the HOMO–LUMO gap by less than 0.1 V. It remains unclear whether the switching alters the charge state of  $\text{TbPc}_2$  similar to the observation by Komeda *et al.* [47] for  $\text{TbPc}_2$  in molecular layers. Unfortunately, they do not comment on the Kondo effect, charge or spin state of individual molecules on Au(111). Comparing to the negatively charged isolated  $\text{TbPc}_2$  molecule on cobalt nanoislands on Ir(111), the higher work function for Ir(111) (5.7 eV [104, 105]) in comparison to cobalt (Co(0001): 5.3 eV [106]) means that it costs more energy to transfer an electron from the surface to the molecule on Ir(111), and it therefore remains unclear whether the molecule is charged.

### Comparison to $\text{TbPc}_2$ on cobalt nanoislands

In comparison with  $\text{TbPc}_2$  adsorbed on Co nanoislands on Ir(111), the achiral conformation of  $\text{TbPc}_2$  on Ir(111) is most similar both in geometric and electronic structure. A chiral conformation is not found on Co/Ir(111); neither room-temperature preparation nor the local current heating scheme yield chiral molecules. A spin-resolved investigation of chiral and similar achiral molecules would be of fundamental interest.



# Summary

In this work, the single-molecule magnet  $\text{TbPc}_2$  was investigated by spin-averaging and spin-polarised scanning tunnelling microscopy and -spectroscopy. The adsorption of  $\text{TbPc}_2$  on ferromagnetic cobalt nanoislands on Ir(111) was investigated.  $\text{TbPc}_2$  was found to adsorb intact on the substrate, and to chemisorb on the substrate, as deduced from its strong bonding with the substrate manifested in manipulation experiments, from the rarely observed influence of the second below-surface substrate layer on the number of adsorption orientations, and from its hybridisation with substrate states manifested in the spin polarisation of the lower Pc ring. The adsorption position was determined and found to be incompatible with the results of external DFT calculations, which might give more accurate results in the future when additionally taking into account the Hubbard  $U$  term.

Spin-polarised scanning tunnelling microscopy and -spectroscopy revealed the energy-dependent spin structure of the molecule. Within the HOMO–LUMO gap, spin polarisation of opposite sign relative to the substrate, following the geometry of the lower Pc ring was found, stemming from hybridisation with spin-polarised substrate states.

The LUMO of  $\text{TbPc}_2$  on cobalt on Ir(111) was found to be spin-split. The magnitude of the splitting was determined to be  $(210 \pm 20)$  eV by spin-resolved point spectroscopy, and the lower-energy spin channel is the one with opposite polarisation with respect to the substrate. Constant-height  $dI/dU$  maps of both spin channels clearly resolved the spatial distribution of the LUMO, highly resembling a pristine  $\pi$  orbital. The different meanings of the experimentally deduced quantities spin difference and spin asymmetry are discussed: while the spin difference maps the spatial distribution of spin-polarised orbitals, the spin asymmetry provides a measure of the spin polarisation.

From the observation of a spin-split LUMO, the charge state of the molecule could be determined:  $\text{TbPc}_2$  adsorbed on cobalt on Ir(111) is negatively charged due to a charge transfer from the surface. No signature uniquely assignable to the Tb centre, i.e. no direct access to the 4f electrons, was ob-

served. In particular, a distribution of 4f electrons over the upper Pc ring as suggested by Vitali *et al.* [11] was not observed.

Adsorbed on bare Ir(111),  $TbPc_2$  was observed in a chiral and an achiral conformation. The chiral conformation was found to switch into the achiral one when applying an elevated bias voltage. The switching process was determined to be a one-electron process based on inelastic tunnelling. With the reverse process feasible (although with low success rate) as well, the chirality of the molecule can be switched on and off, and the handedness can be controlled by repeated random switching.

A new STM setup for operation at  $T = 380$  mK and in high magnetic fields of  $B = 17$  T was built and tested. It is equipped with facilities for molecular evaporation, especially deposition at very low temperature. The design principles and the challenges for a successful operation have been described in detail.

# Bibliography

- [1] L. Bogani and W. Wernsdorfer, *Nat. Mater.* **7**, 179 (2008).
- [2] M. Urdampilleta, S. Klyatskaya, J.-P. Cleuziou, M. Ruben, and W. Wernsdorfer, *Nat Mater* **10**, 502 (2011).
- [3] A. Candini, S. Klyatskaya, M. Ruben, W. Wernsdorfer, and M. Affronte, *Nano Letters* **11**, 2634 (2011).
- [4] M. N. Leuenberger and D. Loss, *Nature* **410**, 789 (2001).
- [5] A. Dei and D. Gatteschi, *Angew. Chem. Int. Ed.* **50**, 11852 (2011).
- [6] R. Sessoli, D. Gatteschi, A. Caneschi, and M. A. Novak, *Nature* **365**, 141 (1993).
- [7] N. Ishikawa, M. Sugita, T. Ishikawa, S.-y. Koshihara, and Y. Kaizu, *Journal of the American Chemical Society* **125**, 8694 (2003).
- [8] J. D. Rinehart and J. R. Long, *Chem. Sci.* **2**, 2078 (2011).
- [9] T. Miyamachi, T. Schuh, T. Markl, C. Bresch, T. Balashov, A. Stohr, C. Karlewski, S. Andre, M. Marthaler, M. Hoffmann, M. Geilhufe, S. Ostanin, W. Hergert, I. Mertig, G. Schon, A. Ernst, and W. Wulfhekel, *Nature* **503**, 242 (2013).
- [10] M. Steinbrecher, A. Sonntag, M. d. S. Dias, M. Bouhassoune, S. Lounis, J. Wiebe, R. Wiesendanger, and A. A. Khajetoorians, *Nature Communications* **7**, 10454 (2016).
- [11] L. Vitali, S. Fabris, A. M. Conte, S. Brink, M. Ruben, S. Baroni, and K. Kern, *Nano Letters* **8**, 3364 (2008).
- [12] S. Stepanow, J. Honolka, P. Gambardella, L. Vitali, N. Abdurakhmanova, T.-C. Tseng, S. Rauschenbach, S. L. Tait, V. Sessi, S. Klyatskaya, M. Ruben, and K. Kern, *Journal of the American Chemical Society* **132**, 11900 (2010).

- [13] R. Wiesendanger, Rev. Mod. Phys. **81**, 1495 (2009).
- [14] C. Iacovita, M. V. Rastei, B. W. Heinrich, T. Brumme, J. Kortus, L. Limot, and J. P. Bucher, Phys. Rev. Lett. **101**, 116602 (2008).
- [15] J. Brede, N. Atodiresei, S. Kuck, P. Lazić, V. Caciuc, Y. Morikawa, G. Hoffmann, S. Blügel, and R. Wiesendanger, Phys. Rev. Lett. **105**, 047204 (2010).
- [16] N. Atodiresei, J. Brede, P. Lazić, V. Caciuc, G. Hoffmann, R. Wiesendanger, and S. Blügel, Phys. Rev. Lett. **105**, 066601 (2010).
- [17] G. Binnig, H. Rohrer, C. Gerber, and E. Weibel, Phys. Rev. Lett. **49**, 57 (1982).
- [18] J. Wiebe, Ph.D. thesis, University of Hamburg, 2003.
- [19] J. Bardeen, Phys. Rev. Lett. **6**, 57 (1961).
- [20] J. Tersoff and D. R. Hamann, Phys. Rev. Lett. **50**, 1998 (1983).
- [21] J. Tersoff and D. R. Hamann, Phys. Rev. B **31**, 805 (1985).
- [22] V. A. Ukraintsev, Phys. Rev. B **53**, 11176 (1996).
- [23] R. Feenstra, J. A. Stroscio, and A. Fein, Surface Science **181**, 295 (1987).
- [24] C. J. Chen, *Introduction to Scanning Tunneling Microscopy: Second Edition* (Oxford University Press, Great Clarendon Street, Oxford OX2 6DP, 2007).
- [25] L. Gross, N. Moll, F. Mohn, A. Curioni, G. Meyer, F. Hanke, and M. Persson, Phys. Rev. Lett. **107**, 086101 (2011).
- [26] J. C. Slonczewski, Phys. Rev. B **39**, 6995 (1989).
- [27] S. Heinze, Ph.D. thesis, Universität Hamburg, 2000.
- [28] R. Wiesendanger, M. Bode, and M. Getzlaff, Appl. Phys. Lett. **75**, 124 (1999).
- [29] R. Wiesendanger and M. Bode, Solid State Commun. **119**, 341 (2001).
- [30] F. Meier, L. Zhou, J. Wiebe, and R. Wiesendanger, Science **320**, 82 (2008).

- [31] A. Kubetzka, Ph.D. thesis, University of Hamburg, 2002.
- [32] A. Li Bassi, C. S. Casari, D. Cattaneo, F. Donati, S. Foglio, M. Passoni, C. E. Bottani, P. Biagioni, A. Brambilla, M. Finazzi, F. Ciccacci, and L. Duo, *Applied Physics Letters* **91**, 173120 (2007).
- [33] A. Schlenhoff, S. Krause, G. Herzog, and R. Wiesendanger, *Applied Physics Letters* **97**, 083104 (2010).
- [34] R. Wiesendanger, H.-J. Güntherodt, G. Güntherodt, R. J. Gambino, and R. Ruf, *Phys. Rev. Lett.* **65**, 247 (1990).
- [35] X.-Y. Wang, C. Avendano, and K. R. Dunbar, *Chem. Soc. Rev.* **40**, 3213 (2011).
- [36] Y.-Y. Zhu, C. Cui, K. Qian, J. Yin, B.-W. Wang, Z.-M. Wang, and S. Gao, *Dalton Trans.* **43**, 11897 (2014).
- [37] J. D. Rinehart, M. Fang, W. J. Evans, and J. R. Long, *J. Am. Chem. Soc.* **133**, 14236 (2011).
- [38] F. Branzoli, P. Carretta, M. Filibian, G. Zoppellaro, M. J. Graf, J. R. Galan-Mascaros, O. Fuhr, S. Brink, and M. Ruben, *Journal of the American Chemical Society* **131**, 4387 (2009).
- [39] C. R. Ganivet, B. Ballesteros, G. de la Torre, J. M. Clemente-Juan, E. Coronado, and T. Torres, *Chem. Eur. J.* **19**, 1457 (2013).
- [40] H. H. Wickham, A. M. Trozzolo, H. J. Williams, G. W. Hull, and F. R. Merritt, *Phys. Rev.* **163**, 526 (1967).
- [41] H. H. Wickman, A. M. Trozzolo, H. J. Williams, G. W. Hull, and F. R. Merritt, *Phys. Rev.* **155**, 563 (1967).
- [42] J. R. Friedman, M. P. Sarachik, J. Tejada, J. Maciejewski, and R. Ziolo, *Journal of Applied Physics* **79**, 6031 (1996).
- [43] J. R. Friedman, M. P. Sarachik, J. Tejada, and R. Ziolo, *Phys. Rev. Lett.* **76**, 3830 (1996).
- [44] R. Sessoli, H. L. Tsai, A. R. Schake, S. Wang, J. B. Vincent, K. Foltling, D. Gatteschi, G. Christou, and D. N. Hendrickson, *Journal of the American Chemical Society* **115**, 1804 (1993).
- [45] R. Vincent, S. Klyatskaya, M. Ruben, W. Wernsdorfer, and F. Balestro, *Nature* **488**, 357 (2012).

- [46] N. Ishikawa, Y. Mizuno, S. Takamatsu, T. Ishikawa, and S.-y. Koshihara, *Inorganic Chemistry* **47**, 10217 (2008).
- [47] T. Komeda, H. Isshiki, J. Liu, Y.-F. Zhang, N. Lorente, K. Katoh, B. K. Breedlove, and M. Yamashita, *Nat. Commun.* **2**, 217 (2011).
- [48] F. Neese and D. A. Pantazis, *Faraday Discuss.* **148**, 229 (2011).
- [49] L. Margheriti, M. Mannini, L. Sorace, L. Gorini, D. Gatteschi, A. Caneschi, D. Chiappe, R. Moroni, F. B. de Mongeot, A. Cornia, F. M. Piras, A. Magnani, and R. Sessoli, *Small* **5**, 1460 (2009).
- [50] M. Mannini, F. Pineider, C. Danieli, F. Totti, L. Sorace, P. Sainctavit, M.-A. Arrio, E. Otero, L. Joly, J. C. Cezar, A. Cornia, and R. Sessoli, *Nature* **468**, 417 (2010).
- [51] N. Ishikawa, M. Sugita, T. Ishikawa, S.-y. Koshihara, and Y. Kaizu, *The Journal of Physical Chemistry B* **108**, 11265 (2004).
- [52] N. Ishikawa, M. Sugita, N. Tanaka, T. Ishikawa, S.-y. Koshihara, and Y. Kaizu, *Inorganic Chemistry* **43**, 5498 (2004).
- [53] N. Ishikawa, O. Ohno, and Y. Kaizu, *Chemical Physics Letters* **180**, 51 (1991).
- [54] A. A. Khajetoorians, J. Wiebe, B. Chilian, S. Lounis, S. Blügel, and R. Wiesendanger, *Nature Physics* **8**, 497 (2012).
- [55] A. A. Khajetoorians, B. Baxevanis, C. Hübner, T. Schlenk, S. Krause, T. O. Wehling, S. Lounis, A. Lichtenstein, D. Pfannkuche, J. Wiebe, and R. Wiesendanger, *Science* **339**, 55 (2013).
- [56] P. K. Hansma and H. P. Broida, *Appl. Phys. Lett.* **32**, 545 (1978).
- [57] B. C. Stipe, M. A. Rezaei, and W. Ho, *Science* **280**, 1732 (1998).
- [58] Y. J. Song, A. F. Otte, V. Shvarts, Z. Zhao, Y. Kuk, S. R. Blankenship, A. Band, F. M. Hess, and J. A. Stroscio, *Review of Scientific Instruments* **81**, 121101 (2010).
- [59] L. Zhang, T. Miyamachi, T. Tomanić, R. Dehm, and W. Wulfhekel, *Review of Scientific Instruments* **82**, 103702 (2011).
- [60] J. Wiebe, A. Wachowiak, F. Meier, D. Haude, T. Foster, M. Morgenstern, and R. Wiesendanger, *Rev. Sci. Instrum.* **75**, 4871 (2004).

- [61] S. Meckler, M. Gyamfi, O. Pietzsch, and R. Wiesendanger, *Rev. Sci. Instrum.* **80**, (2009).
- [62] S. Loth, M. Etzkorn, C. P. Lutz, D. M. Eigler, and A. J. Heinrich, *Science* **329**, 1628 (2010).
- [63] M. F. Crommie, C. P. Lutz, and D. M. Eigler, *Science* **262**, 218 (1993).
- [64] A. A. Khajetoorians, S. Lounis, B. Chilian, A. T. Costa, L. Zhou, D. L. Mills, J. Wiebe, and R. Wiesendanger, *Phys. Rev. Lett.* **106**, 037205 (2011).
- [65] S. Kuck, J. Wienhausen, G. Hoffmann, and R. Wiesendanger, *Rev. Sci. Instrum.* **79**, 083903 (2008).
- [66] K. Lämmle, *Review of Scientific Instruments* **81**, 053902 (2010).
- [67] S. K. Hämäläinen, M. Stepanova, R. Drost, P. Liljeroth, J. Lahtinen, and J. Sainio, *The Journal of Physical Chemistry C* **116**, 20433 (2012).
- [68] M. Nohme, Master's thesis, University of Hamburg, 2008.
- [69] J. Ekin, *Experimental Techniques for Low Temperature Measurements: Cryostat Design, Materials, and Critical-Current Testing* (Oxford University Press, Great Clarendon Street, Oxford OX2 6DP, 2006).
- [70] O. Pietzsch, A. Kubetzka, D. Haude, M. Bode, and R. Wiesendanger, *Rev. Sci. Instrum.* **71**, 424 (2000), 8th International Conference on Ion Sources (ICIS 99), Kyoto, Japan, Sep 06-10, 1999.
- [71] A. Lodi Rizzini, C. Krull, T. Balashov, J. J. Kavich, A. Mugarza, P. S. Miedema, P. K. Thakur, V. Sessi, S. Klyatskaya, M. Ruben, S. Stepanow, and P. Gambardella, *Phys. Rev. Lett.* **107**, 177205 (2011).
- [72] A. Lodi Rizzini, C. Krull, T. Balashov, A. Mugarza, C. Nistor, F. Yakhov, V. Sessi, S. Klyatskaya, M. Ruben, S. Stepanow, and P. Gambardella, *Nano Letters* **12**, 5703 (2012).
- [73] O. Pietzsch, A. Kubetzka, M. Bode, and R. Wiesendanger, *Phys. Rev. Lett.* **92**, 057202 (2004).
- [74] O. Pietzsch, S. Okatov, A. Kubetzka, M. Bode, S. Heinze, A. Lichtenstein, and R. Wiesendanger, *Phys. Rev. Lett.* **96**, 237203 (2006).
- [75] S. Ouazi, S. Wedekind, G. Rodary, H. Oka, D. Sander, and J. Kirschner, *Phys. Rev. Lett.* **108**, 107206 (2012).

- [76] J. E. Bickel, F. Meier, J. Brede, A. Kubetzka, K. von Bergmann, and R. Wiesendanger, *Phys. Rev. B* **84**, 054454 (2011).
- [77] Y. Zhang, P. Guan, H. Isshiki, M. Chen, M. Yamashita, and T. Komeda, *Nano Research* **3**, 604 (2010).
- [78] S. Fahrenndorf, N. Atodiresei, C. Besson, V. Caciuc, F. Matthes, S. Blügel, P. Kögerler, D. E. Bürgler, and C. M. Schneider, *Nat. Commun.* **4**, 2425 (2013).
- [79] G. Nazin, S. Wu, and W. Ho, *Proc. Natl. Acad. Sci. U. S. A.* **102**, 8832 (2005).
- [80] C. Uhlmann, I. Swart, and J. Repp, *Nano Lett.* **13**, 777 (2013).
- [81] S.-H. Chang, S. Kuck, J. Brede, L. Lichtenstein, G. Hoffmann, and R. Wiesendanger, *Phys. Rev. B* **78**, 233409 (2008).
- [82] Y.-F. Zhang, H. Isshiki, K. Katoh, Y. Yoshida, M. Yamashita, H. Miyasaka, B. K. Breedlove, T. Kajiwara, S. Takaishi, and T. Komeda, *The J. Phys. Chem. C* **113**, 14407 (2009).
- [83] Y. He, Y. Zhang, I.-P. Hong, F. Cheng, X. Zhou, Q. Shen, J. Li, Y. Wang, J. Jiang, and K. Wu, *Nanoscale* **6**, 10779 (2014).
- [84] Y. Zhang, P. Liao, J. Kan, C. Yin, N. Li, J. Liu, Q. Chen, Y. Wang, W. Chen, G. Q. Xu, J. Jiang, R. Berndt, and K. Wu, *Phys. Chem. Chem. Phys.* **17**, 27019 (2015).
- [85] K. Katoh, Y. Yoshida, M. Yamashita, H. Miyasaka, B. K. Breedlove, T. Kajiwara, S. Takaishi, N. Ishikawa, H. Isshiki, Y. F. Zhang, T. Komeda, M. Yamagishi, and J. Takeya, *J. Am. Chem. Soc.* **131**, 9967 (2009).
- [86] D. Qi, L. Zhang, L. Wan, Y. Zhang, Y. Bian, and J. Jiang, *Phys. Chem. Chem. Phys.* **13**, 13277 (2011).
- [87] X. Lu, K. W. Hipps, X. D. Wang, and U. Mazur, *J. Am. Chem. Soc.* **118**, 7197 (1996).
- [88] J. Brede and R. Wiesendanger, *Phys. Rev. B* **86**, 184423 (2012).
- [89] Y.-H. Chu, C.-H. Hsu, C.-I. Lu, H.-H. Yang, T.-H. Yang, C.-H. Luo, K.-J. Yang, S.-H. Hsu, G. Hoffmann, C.-C. Kaun, and M.-T. Lin, *ACS Nano* **9**, 7027 (2015).

- [90] J. A. Stroscio and W. J. Kaiser, *Scanning Tunneling Microscopy* (Academic Press, New York, 1993), Vol. 27.
- [91] S. L. Kawahara, J. Lagoute, V. Repain, C. Chacon, Y. Girard, S. Rousset, A. Smogunov, and C. Barreteau, *Nano Letters* **12**, 4558 (2012).
- [92] M. Getzlaff and G. Schönhense, *Surface Science* **331–333, Part A**, 213 (1995).
- [93] W. Clemens, E. Vescovo, T. Kachel, C. Carbone, and W. Eberhardt, *Phys. Rev. B* **46**, 4198 (1992).
- [94] A. Mugarza, R. Robles, C. Krull, R. Korytár, N. Lorente, and P. Gambardella, *Phys. Rev. B* **85**, 155437 (2012).
- [95] K. L. Trojan, W. E. Hatfield, K. D. Kepler, and M. L. Kirk, *J. Appl. Phys.* **69**, 6007 (1991).
- [96] K. L. Trojan, J. L. Kendall, K. D. Kepler, and W. E. Hatfield, *Inorganica Chimica Acta* **198-200**, 795 (1992).
- [97] J. L. Zhang, J. Q. Zhong, J. D. Lin, W. P. Hu, K. Wu, G. Q. Xu, A. T. S. Wee, and W. Chen, *Chem. Soc. Rev.* **44**, 2998 (2015).
- [98] S. Weigelt, C. Busse, L. Petersen, E. Rauls, B. Hammer, K. Gothelf, F. Besenbacher, and T. Linderoth, *Nat. Mater.* **5**, 112 (2006).
- [99] X. H. Qiu, G. V. Nazin, and W. Ho, *Phys. Rev. Lett.* **93**, 196806 (2004).
- [100] T. G. Gopakumar, J. Meiss, D. Pouladsaz, and M. Hietschold, *The J. Phys. Chem. C* **112**, 2529 (2008).
- [101] G. Schulze, K. J. Franke, and J. I. Pascual, *New Journal of Physics* **10**, 065005 (2008).
- [102] G. Schulze, K. J. Franke, A. Gagliardi, G. Romano, C. S. Lin, A. L. Rosa, T. A. Niehaus, T. Frauenheim, A. Di Carlo, A. Pecchia, and J. I. Pascual, *Phys. Rev. Lett.* **100**, 136801 (2008).
- [103] D. Écija, W. Auwärter, S. Vijayaraghavan, K. Seufert, F. Bischoff, K. Tashiro, and J. V. Barth, *Angew. Chem. Int. Ed.* **50**, 3872 (2011).
- [104] F. Schulz, R. Drost, S. K. Hämäläinen, T. Demonchaux, A. P. Seitsonen, and P. Liljeroth, *Phys. Rev. B* **89**, 235429 (2014).

- [105] M. Kaack and D. Fick, *Surface Science* **342**, 111 (1995).
- [106] S. Saito, K. Takeda, T. Soumura, M. Ohki, T. Tani, and T. Maeda, *Journal of Applied Physics* **71**, 5500 (1992).

# Publications

J. Schwöbel, Y.-S. Fu, J. Brede, A. Dilullo, G. Hoffmann, S. Klyatskaya, M. Ruben, and R. Wiesendanger,  
*Real-space observation of spin-split molecular orbitals of adsorbed single-molecule magnets,*  
Nat. Commun. **3**, 953 (2012).

Y.-S. Fu, J. Schwöbel, S.-W. Hla, A. Dilullo, G. Hoffmann, S. Klyatskaya, M. Ruben, and R. Wiesendanger,  
*Reversible Chiral Switching of Bis(phthalocyaninato) Terbium(III) on a Metal Surface,*  
Nano Lett. **12**, 3931 (2012).

J. Brede, M. Linares, S. Kuck, J. Schwöbel, A. Scarfato, S.-H. Chang, G. Hoffmann, R. Wiesendanger, R. Lensen, P. H. J. Kouwer, J. Hoogboom, A. E. Rowan, M. Bröring, M. Funk, S. Stafström, F. Zerbetto, and R. Lazzaroni,  
*Dynamics of molecular self-ordering in tetraphenyl porphyrin monolayers on metallic substrates,*  
Nanotechnology **20**, 275602 (2009).

C. Bartels, C. Hock, J. Huwer, R. Kuhnen, J. Schwöbel, and B. von Issendorff,  
*Probing the Angular Momentum Character of the Valence Orbitals of Free Sodium Nanoclusters,*  
Science **323**, 1323 (2009).



# Talks and poster presentations

## Contributed talks

J. Schwöbel, Y.-S. Fu, A. Dilullo, J. Brede, S. Klyatskaya, M. Ruben, G. Hoffmann, and R. Wiesendanger,  
*Spin-sensitive tunneling through individual Terbium-Phthalocyanine Molecules by Spin-polarized Scanning Tunneling Microscopy*,  
75th Spring Conference, Deutsche Physikalische Gesellschaft, Dresden (Germany), 2011-03-14.

*Spin-sensitive Tunneling through individual Terbium- $Pc_2$  Molecules by Spin-polarized STM*,  
PGI-1 Seminar, Peter Grünberg Institute, Forschungszentrum Jülich, Jülich (Germany), 2010-10-13.

## Poster presentations

J. Schwöbel, M. Nohme, R. Ravlić, J. Wienhausen, G. Hoffmann, and R. Wiesendanger,  
*Design and construction of a 300 mKelvin / 17 Tesla ultra-high vacuum scanning tunneling microscope for molecular studies*,  
72nd Spring Conference, Deutsche Physikalische Gesellschaft, Berlin (Germany), 2008-02-27.

J. Brede, J. Schwöbel, S. Kuck, G. Hoffmann, and R. Wiesendanger,  
*A Scanning tunneling microscope study of single Phthalocyanine molecules on ultra thin insulating layers on different metal substrates*,  
74th Spring Conference, Deutsche Physikalische Gesellschaft, Regensburg (Germany), 2010-03-25.



# Acknowledgement

Zunächst möchte ich meinem Betreuer, Prof. Wiesendanger, für die vielfältige und andauernde Unterstützung danken. Meinem Untergruppenleiter Germar Hoffmann sowie meinen engen Kollegen Jens Brede und Stefan Kuck danke ich für großartigen Input, Hilfe und Diskussionen. Der Molekül-Untergruppe sowie der gesamten Gruppe R danke ich für erfolgreiche Zusammenarbeit, die tolle Atmosphäre, den Austausch und all die sich hier selbstverständlich anfühlenden gegenseitigen Kleinigkeiten.

Lars Krieger, Jens Brede und Maciej Bazarnik danke ich für das Korrekturlesen.

Der mechanischen Werkstatt und dem Heliumteam danke ich für tollen Einsatz, der weit jenseits einer Angestelltenmentalität liegt.

Meiner Familie, Freunden und Mitbewohnern danke ich für den großen Rückhalt.

Außerdem danke ich den Geldgebern, insbesondere dem GrK 611 und dem SFB 668, dafür, unsere Forschung überhaupt möglich zu machen.